Foreground Cleaning for Cosmic Microwave Background Polarimeters in the Presence of Instrumental Effects

A THESIS
SUBMITTED TO THE FACULTY OF THE GRADUATE SCHOOL
OF THE UNIVERSITY OF MINNESOTA
BY

Chaoyun Bao

IN PARTIAL FULFILLMENT OF THE REQUIREMENTS
FOR THE DEGREE OF
Doctor of Philosophy

Professor Shaul Hanany

June, 2015

Acknowledgements

There are numerous people who have supported me through all the ups and downs in my graduate student life. First of all, I would like to express special gratitude to my advisor, Professor Shaul Hanany, who has been a tremendous mentor and role model for me in the past years. His guidance helped me to become a better researcher, communicator and person in general. I would not be who I am today without his influence.

I want to thank the entire EBEX collaboration and the observational cosmology lab at the University of Minnesota. It has been a wonderful experience to work in a collaborative, productive and welcoming environment. I want to specially thank Samuel Leach and Ben Gold, my two direct mentors on software development and data analysis of CMB. I also want to thank Carlo Baccigalupi, Andrew Jaffe, Jeff Klein, Giorgio Savini, Greg Tucker and Kyle Zilic for all the discussion and data products which lead to this thesis.

On a personal level, I would like to thank my family for their support, patience and understanding throughout the years. Particularly to my father Kangjian Bao, my late mother Xiaomin Wang and my boyfriend François Aubin, I can not mention enough how much their support meant to me. I also want to thank all my friends who supported me through my graduate school life, one way or the other: Kate Raach, Yuanjing Jin, Marilyn Bennett, Yuanyuan Zhang, Hao Dou, Bert Pablo, Asad & Liz Aboobaker, Tianran Chen, Shelley Frankel, Xiaohui Li, all my friends from the Minnesota Chinese Dance Theater, Al-Bahira Middle Eastern Dance Theater and Women in Physics and Astronomy student group and many many other people.

Last but not least, I would like to thank NASA, NSF, SISSA, MSI and Doctoral Dissertation Fellowship for all the financial and computing support for my work.

Dedication

谨以此文献给我的父亲鲍康健和远在天国的母亲汪晓敏。

Abstract

The Cosmic Microwave Background (CMB) B-mode polarization signal offers a direct probe of inflation, a period of exponential expansion in the extreme early universe. The inflationary CMB B-mode polarization signal, however, is subject to the contamination of polarized galactic thermal dust foreground emission. A robust foreground cleaning method is essential for CMB polarimeters targeting the inflationary B-mode signal. In this thesis I present my work on developing foreground cleaning algorithms particularly in the presence of instrumental effects.

One of the instrumental effects I focus on in this work is the frequency dependent polarization rotation effect such as the one caused by an achromatic half-wave plate (AHWP). As an example, I use the AHWP of the E and B Experiment (EBEX) in this work and study the relation between the frequency dependent rotation effect and the characteristic parameters of the AHWP. To address the effect of an AHWP while removing galactic dust foreground contamination, I developed two foreground cleaning algorithms: a simple method that assumes perfect knowledge of the AHWP and a few simplifying assumptions, and a more sophisticated algorithm based on maximum likelihood method. Based on simulation results, the maximum likelihood foreground cleaning algorithm can recover CMB B-mode signal without any bias in the presence of band shape uncertainty, frequency dependent rotation effect and instrumental noise with realistic measurement accuracy of instrumental parameters.

In this thesis I also present my work on calculating the atmospheric loading in the millimeter wave regime for sub-orbital CMB experiments such as EBEX. Having a proper prediction of the atmospheric loading is an important input to detector designs for CMB experiments.

Contents

Acknowledgements **i**

Dedication **ii**

Abstract **iii**

List of Tables **vii**

List of Figures **viii**

1 Introduction **1**

2 Scientific Background **3**

2.1 Cosmic Microwave Background and the Big Bang 3

2.2 Inflation 7

2.3 Foreground Contamination 8

3 The E and B Experiment **10**

3.1 EBEX Science 10

3.2 EBEX Instrument 11

4 Performance Simulation of an Achromatic Half-Wave Plate **17**

4.1 Half-wave plate polarimetry model 18

4.1.1 Stokes vector and Mueller matrices 18

4.1.2 Single HWP polarimetry model 19

4.1.3 Achromatic half-wave plate polarimetry . . . 23
4.2 Modeling the AHWP frequency dependent rotation . . . 27
4.2.1 Indices of refraction . . . 27
4.2.2 Relative orientation of the plates . . . 32
4.2.3 Thickness of the plates . . . 33
4.2.4 Observation frequency band . . . 34
4.2.5 Incoming signal spectrum . . . 42
4.2.6 Combined effect from bands and incident spectra . . . 45
4.2.7 Comparison with other predictive model . . . 46
4.2.8 Comparison with experimental data . . . 47
4.2.9 Discussion . . . 49

5 Simple Foreground Cleaning Method in the Presence of an AHWP 51
5.1 Description of the Simulation . . . 52
5.2 The Effect of Galactic Dust . . . 54
5.3 Removing AHWP Induced Rotation in Dust Subtraction . . . 56
5.4 Uncertainty in Detection Band and High Frequency Spectral Response . . . 59
5.4.1 Shift of Band-Center . . . 59
5.4.2 Misestimate of Band-Width . . . 61
5.4.3 Effects of High Frequency Spectral Leak . . . 63
5.5 Discussion and Summary . . . 63

6 Maximum Likelihood Foreground Cleaning with Instrumental Effects 66
6.1 Theoretical Framework . . . 67
6.1.1 Basic Formalism . . . 67
6.1.2 Extension of the Basic Formalism . . . 68
6.1.3 Error Propagation . . . 76
6.2 Simulations . . . 77
6.3 Results . . . 82
6.3.1 Band Shape Uncertainty . . . 83
6.3.2 Frequency Dependent Rotation Effect . . . 89
6.3.3 Combining the Band Shape and Rotation effect . . . 94

6.4 Discussion 98

7 Atmospheric Loading **100**

7.1 Software packages to model the atmosphere 100

7.1.1 ATM package for ALMA 101

7.1.2 *am* 102

7.1.3 AT – Atmospheric Transmission Software 103

7.1.4 Comparison between different models 103

7.2 Atmospheric loading calculation 104

7.2.1 From transmission curve to atmospheric loading power 106

7.2.2 Atmospheric loading for EBEX north America flight 107

7.2.3 Atmospheric loading for EBEX long duration balloon flight 111

7.2.4 Atmospheric loading at ground observation sites 114

8 Conclusion **118**

References **119**

Appendix A. AHWP Performance in EBEX Ground Bands **130**

List of Tables

4.1 Design parameters of EBEX five-stack sapphire AHWP. 27
4.2 Indices of refraction of sapphire at 300 K and 5.8 K 30
4.3 Thicknesses of the single HWPs in the EBEX AHWP 34
4.4 Best fit EBEX AHWP parameters at cryogenic temperature 36
4.5 $\langle\phi\rangle$ for various top-hat bands using EBEX AHWP 36
4.6 EBEX band characteristics in LDB flight configuration 40
4.7 Best fit EBEX AHWP parameters at room temperature 42
4.8 $\langle\phi\rangle$ for different incident spectra in various top-hat bands 45
4.9 $\langle\phi\rangle$ for different incident spectra in EBEX LDB flight bands 46
5.1 AHWP and band parameters used in the simulations. 54
6.1 EBEX bands and pixel noise in the Q and U maps used in the simulation . 79
6.2 EBEX band mismatch corresponding to scaling coefficient mismatch 89
6.3 Prior constraints of η and θ for EBEX LDB bands 96
7.1 Example parameters for comparing various atmosphere modeling software . 104
7.2 Comparison between atmospheric loading calculated by ATM, AT and *am* . 104
7.3 Atmospheric parameters for EBEX NA flight 107
7.4 Atmospheric parameters for EBEX LDB flight 111
7.5 Atmospheric parameters for ground observation sites 115
7.6 Atmospheric loading for Palestine, TX at various elevation 116
A.1 EBEX band characteristics in ground calibration configuration 132
A.2 $\langle\phi\rangle$ for different incident spectra in EBEX bands during ground calibration 132

List of Figures

2.1 CMB temperature anisotropy map 5
2.2 Power spectrum of the CMB temperature anisotropy 6
2.3 Production of polarization via Thomson scattering 7
3.1 Power spectra of the designed performance of EBEX 12
3.2 EBEX planned patch 14
3.3 EBEX outer frame 15
3.4 EBEX inner frame and cryogenic receiver 15
3.5 EBEX AHWP assembly 16
4.1 HWP polarimetry schematic plot 19
4.2 Modulation Efficiency vs ν at various α_{in} 23
4.3 AHWP polarimetry schematic plot 24
4.4 AHWP IVA curves at various frequencies 26
4.5 IVA phase offset ϕ vs ν 28
4.6 Measured indices of refraction of sapphire as a function of frequency 29
4.7 ϕ vs ν for EBEX AHWP at room temperature 30
4.8 Effect of frequency dependent n_o and n_e on Δn and ϕ vs ν 31
4.9 ϕ vs ν for EBEX AHWP using best fit $\vec{\theta}$ 32
4.10 ϕ vs ν for EBEX AHWP assuming $d = 1.69$ mm 33
4.11 ϕ vs ν for EBEX AHWP using best fit thicknesses of the plates 35
4.12 ϕ vs ν for best fit EBEX AHWP parameters at cryogenic temperature . . . 37
4.13 $\langle\phi\rangle$ vs band shift for EBEX 38
4.14 $\langle\phi\rangle$ vs change of band-width for EBEX 39
4.15 Measured EBEX bands in the LDB flight configuration 41

4.16 ϕ vs ν for EBEX best fit AHWP parameters at room temperature 43
4.17 Comparison of ϕ vs ν curve from different predictive models 47
4.18 Comparison between model and relative phase measurement at Cardiff . . . 48
4.19 Comparison between simulation and absolute polarization calibration 50
5.1 CMB and galactic dust B-mode power spectra at 150 GHz 53
5.2 Validation of signal and noise power spectrum estimation 55
5.3 Effect of AHWP rotation due to polarized dust 57
5.4 Effectiveness of the simple dust removal algorithm 60
5.5 Effect of band-center shift on B-mode power spectrum estimation 61
5.6 Effect of band-width change on B-mode power spetrum estimation 62
5.7 Effect of high frequency spectral leak on B-mode power spectrum estimation 64
6.1 Illustration of the definition of in-band scaling coefficient η 70
6.2 Illustration of degeneracy between η_d and β 73
6.3 Q and U maps of CMB and dust at 150 GHz band 78
6.4 Simulated input Q and U maps at 150 GHz band 80
6.5 Demonstration of validity of the extended algorithm 84
6.6 Power spectrum of noiseless simulation with 10 GHz shift of 150 GHz band 85
6.7 Degeneracy between spectral index and in-band dust scaling coefficient . . . 86
6.8 Setting prior constraints on in-band scaling coefficients 87
6.9 Fitting for all in-band scaling coefficients with prior constraints 88
6.10 LDB configuration prior constraints on in-band scaling coefficients 90
6.11 Fitting for rotation angles in 150 GHz band in the absence of noise 91
6.12 Fitting for 150 GHz band rotation angles with nominal EBEX noise 92
6.13 Fitting for all band averaged rotation angles with prior constraints 93
6.14 Fitting for both effects at 150 GHz band in the absence of noise 95
6.15 Fitting for both instrumental effects at 150 GHz band with nominal noise . 96
6.16 Fitting for both instrumental effects in EBEX LDB configuration 97
7.1 Comparison of atmospheric transmission spectra from ATM, AT and *am* . . 105
7.2 Atmospheric transmission vs frequency for EBEX NA flight 108
7.3 Atmosphere antenna temperature vs frequency for EBEX NA flight 109
7.4 Atmospheric loading power for EBEX NA flight 110

7.5 Atmospheric transmission vs frequency for EBEX LDB flight 112
7.6 Atmosphere antenna temperature vs frequency for EBEX LDB flight 113
7.7 Atmospheric loading for EBEX LDB flight 114
7.8 Atmosphere transmission vs frequency for ground sites 115
7.9 Atmosphere antenna temperature vs frequency for ground sites 116
7.10 Atmosphere antenna temperature vs frequency for Palestine, TX 117
A.1 Measured EBEX bands in ground calibration configuration 131

Chapter 1

Introduction

The Cosmic Microwave Background (CMB) is one of the fundamental elements of the modern cosmology. As the oldest light in the universe, it offers precious information about the origin, structure and evolution of the universe. Precise measurements of the CMB have been for the past twenty years and are still an active research frontier in cosmology. Currently, many experimental efforts are focused on searching a possible faint signal called the 'inflationary B-mode signal' in the polarization of the CMB which originates from the inflation period at the very beginning of the universe. Detecting or setting an upper limit of the inflationary B-mode signal not only provides a glimpse to the origin of the universe, but also probes physics at ultra high energy scale that is currently beyond the reach of particle colliders.

One of the challenges for inflationary B-mode measurement is the contamination from the polarized galactic thermal dust foreground emission. To extract the inflationary B-mode signal accurately, the ability to remove galactic dust foreground contamination is essential. This work focuses on developing a robust foreground removal technique for CMB polarimeters in the presence of instrumental effects, particularly the uncertainty in the spectral response of the instrument and a frequency dependent polarization rotation effect. So far we have tested the techniques developed in this work on simulated data. As a concrete example we use the instrumental parameters of the E and B experiment (EBEX) in the simulation.

In Chapter 2 I will briefly overview the scientific background, including the CMB,

the inflation paradigm and the galactic foreground. Then I will give a short summary of EBEX in Chapter 3. In Chapter 4 I am going to discuss the study on the frequency dependent polarization rotation effect of an achromatic half-wave plate (AHWP) and its relation with various parameters of the AHWP, the telescope and the incoming signal. Next I will present a simple foreground removal technique in the presence of the frequency dependent polarization rotation effect and the uncertainty of the instrumental spectral response in Chapter 5. Then in Chapter 6 I will present a foreground removal technique based on maximum likelihood method which handles the instrumental effects better than the simple method. I will finally discuss my simulations about the atmospheric loading in the millimeter wave regime in Chapter 7, for predicting the detector load for sub-orbital CMB experiments such as EBEX.

Chapter 2

Scientific Background

The origin of the universe has always been a question humans trying to answer throughout the history. Today, the Big Bang cosmology is the commonly accepted scientific explanation of the origin of our universe. One of the landmark tests of the Big Bang cosmology is the existence of Cosmic Microwave Background (CMB). The precision measurements of the CMB has greatly shaped our understanding of the universe since the launch of Cosmic Background Explorer in 1989. Despite the huge success standard Big Bang cosmology attains in explaining various observation results, there still exists some puzzle about the early history of the universe. The CMB science remains to be an active research frontier in modern cosmology, trying to provide more evidence of the history in the extreme early universe. In this chapter I will briefly discuss the scientific background related to the Big Bang, the CMB, inflation paradigm and the galactic foreground.

2.1 Cosmic Microwave Background and the Big Bang

First discovered in 1964 by Penzias and Wilson [1], the Cosmic Microwave Background is the relic electromagnetic radiation of the Big Bang permeating the entire universe. Standard Big Bang cosmology states that the Universe began in an extreme hot and dense state 13.8 billion years ago and has been expanding and cooling ever since. After 10^{-6} seconds, the universe consisted of a hot plasma of photons, electrons and baryons held in thermal equilibrium by Thomson scattering and Coulomb interaction. The energy distribution of

the photons followed a black-body spectrum characterized by the Planck function with temperature T,

$$B(\nu, T) = \frac{2h\nu^3}{c^2} \frac{1}{e^{\frac{h\nu}{k_B T}} - 1}. \tag{2.1}$$

Here ν is the frequency of the light, h is the Planck constant, c is the speed of light and k_B is the Boltzmann constant.

About 380,000 years after the Big Bang the temperature of the photon-baryon plasma dropped to ∼3000 K. At this temperature, there were not enough high energy photons to ionize all the electrons from the protons. For the first time in the history of the universe the electrons and protons combined to form neutral hydrogen, making the universe transparent to the photons. This era is called the epoch of recombination (EoR). After the EoR the photons have been streaming through the universe without any obstruction. This radiation is the most ancient and most distant light in the universe we can observe. The temperature of the photons has been decreasing as they travel through the universe. Today the black-body radiation has a temperature of 2.725 K with its peak intensity in the microwave regime at ∼160 GHz. The CMB is a nearly perfect black-body. It is homogeneous across the entire sky to one part in 10^5. Fig. 2.1 shows the CMB temperature anisotropy map measured by the Planck satellite [2].

The statistical properties of the anisotropies of the CMB encodes abundant information about the early universe. To characterize the CMB anisotropies across the sky, the anisotropy map is expanded into spherical harmonics $Y_{\ell m}$ with coefficient $T_{\ell m}$

$$T_{\ell m} = \int d\hat{n} Y^{\star}_{\ell m}(\hat{n}) T(\hat{n}), \tag{2.2}$$

where $T(\hat{n})$ is the temperature anisotropy measured at a particular direction $\hat{n}$ on the sky. The variance C_ℓ of the $T_{\ell m}$ which is defined as

$$\langle T_{\ell m} T^{\star}_{\ell' m'} \rangle = \delta_{\ell \ell'} \delta_{m m'} C_\ell, \tag{2.3}$$

characterizes the angular power spectrum of the map. Typically we plot

$$\Delta T \equiv \sqrt{\frac{\ell(\ell+1)}{2\pi} C_\ell} \tag{2.4}$$

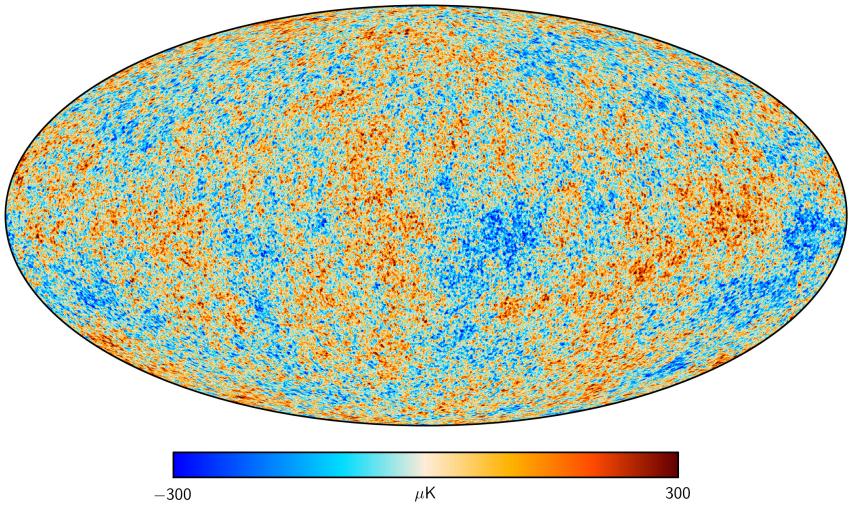

Figure 2.1: CMB temperature anisotropy map measured by the Planck satellite [2].

or ΔT^2 as a function of the multiple moment ℓ as the angular power spectrum. The multiple moment ℓ scales inversely with the angular scale θ on the sky $\ell = \frac{\pi}{\theta}$ so low ℓ means large angular scale and vice versa.

At the EoR, the coupled baryon-photon fluid oscillates in a non-uniform gravitational field at sub-horizon scales. This oscillation causes the CMB temperature power spectrum to have distinct peaks due to the phase difference between standing waves corresponds to different k-modes. As seen in Fig. 2.2, the first acoustic peak in the CMB temperature power spectrum is at $\ell \sim 200$, which corresponds to angular size of about 1° on the sky. The angular size of the first acoustic peak is related to the size of the sound crossing horizon at the epoch of recombination, which marks the size of the region that could be causally connected.

At the epoch of recombination, photons are scattered by electrons via Thompson scattering process. During the Thompson scattering process, any quadrupole moment in the radiation field results in polarization of the scattered light [4], as shown in Fig. 2.3. At the last scattering surface during EoR, the motion of baryon-photon fluid caused by fluctuation in the gravitational field results in a radiation quadrupole seen by individual electron. The

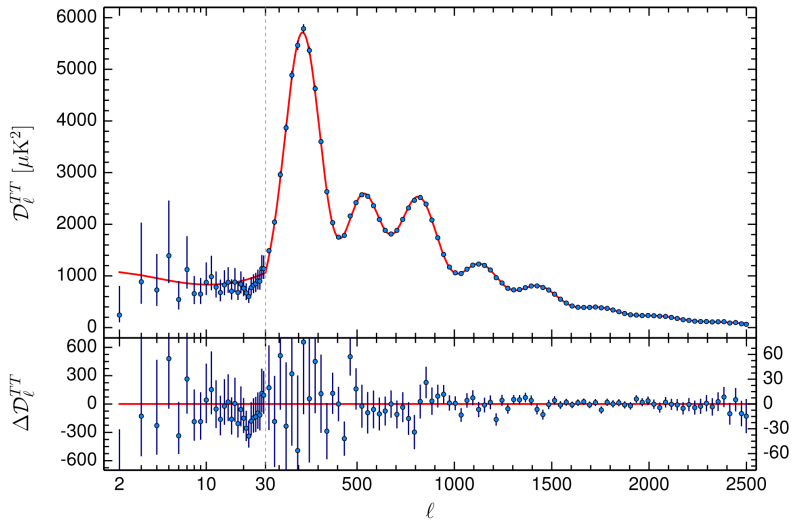

Figure 2.2: Power spectrum of the CMB temperature anisotropy (upper panel)[3]. The error bars show the 1-σ uncertainty. The red line is the best fit ΛCDM model and the bottom panel shows the residuals with respect to the model.

scattered CMB is polarized along the direction of the cold radiation. Globally the CMB polarization map can be decomposed into two orthogonal modes: a curl-free E-mode polarization pattern and a divergence-free B-mode polarization pattern. The density perturbation, which is a scalar perturbation, generates E-mode polarization signal. The temperature anisotropy and E-mode polarization both originates from the same density perturbation. The CMB E-mode polarization signal is at the level of 1 μK and has been measured by various ground based, sub-orbital and satellite CMB experiments [5, 6, 7, 8, 9, 10, 11, 12]. On the other hand, the gravitational wave, which is a tensor perturbation, generates both E-mode and B-mode polarization signal. The gravitational lensing caused by structures formed in the universe randomly deflects the CMB photon and mixes E and B-mode signals. The lensing B-mode signal from the E-mode signal peaks at $\ell \sim 1000$ and is in the order of 0.1 μK. The lensing B-mode signal has been recently measured by POLARBEAR, Atacama Cosmology Telescope (ACT) and South Pole Telescope (SPT) [13, 14, 15].

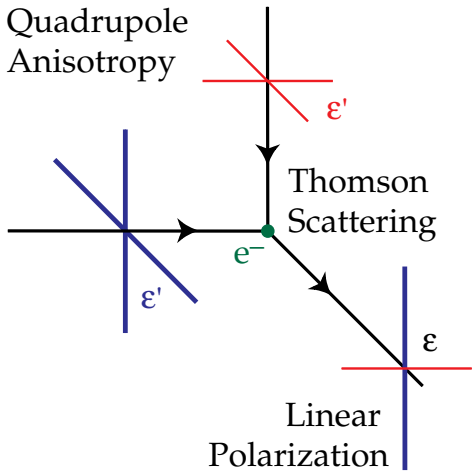

Figure 2.3: Quadruple anisotropy during Thomson scattering produces linear polarization [4].

2.2 Inflation

Although the standard Big Bang cosmology successfully explains many observations, there are a few outstanding puzzles which can not be explained. For example, given the small angular size of the sound crossing horizon at the epoch of recombination it is puzzling that the different regions on the sky which are more than couple degrees apart not only share the same temperature, but also share the temperature fluctuation in a statistical way. This problem, together with the flatness problem, the missing magnetic monopole problem and structure in the Universe are the main issues that could not be resolved by the standard Big Bang model [16].

In the 1980's the inflation paradigm was proposed [17, 18] as a solution to these cosmological problems. The inflation paradigm posits that the universe underwent a superluminal and exponential expansion period within its first 10^{-35} sec, which blew up a causally connected region to a size that is much larger than the Hubble length at that time. The universe expanded at least 60 e-folds during inflation. Although the exact underlying physics of inflation remains unknown, inflation paradigm makes predictions about observable signatures. One of the predictions is that a stochastic inflationary gravity wave background (IGB) was produced during inflation [19, 20, 21, 22, 23]. These gravitational

waves, which are tensor perturbations, produce a unique B-mode polarization signal in the CMB which peaks at $\ell \sim 90$ [24, 25]. The ratio between amplitudes of fluctuation caused by IGB (tensor mode) and by density perturbation generate during inflation (scalar mode) is defined as the 'tensor-to-scalar ratio', denoted as r. The energy scale of the inflation V is predicted to be directly related to r

$$V^{1/4}/m_{pl} = 3.0 \times 10^{-3} r^{1/4}, \tag{2.5}$$

where m_{pl} is the Planck mass. Detecting or setting an upper limit on r will probe underlying mechanism of inflation and physics at ultra high energy scale. The inflationary B-mode signal is predicted to be at most at the level of 0.1 μK and currently the 95% upper limit of r is $r < 0.09$ [3].

2.3 Foreground Contamination

The inflationary B-mode signal is susceptible to foreground contamination from the Milky Way galaxy. The Galaxy has an interstellar magnetic field in the order of 10^{-6}G. The Galactic magnetic field causes synchrotron emission from relativistic electrons and polarization of thermal dust emission. The linear polarization of the thermal dust emission is caused by the alignment of non-spherical dust grains although the exact mechanism of alignment remains unknown. Below 70GHz the synchrotron emission is the dominant foreground source[26]. Recent observation results reveal that the polarized thermal dust signal is much higher than we previously estimated. Above 70GHz the polarized emission from thermal dust in the Galaxy dominates over the inflationary B-mode signal over the entire sky [27, 28, 29, 30]. Even for the cleanest patch of the sky, the galactic dust foreground must be removed correctly to be able to measure the B-mode signal accurately.

Currently no observation data of polarized galactic dust in the mm-wave regime is accurate enough for inflationary B-mode measurements. To monitor and subtract dust contamination, many CMB experiments targeting the inflationary B-mode signal observe in multiple frequency channels. The electromagnetic spectra of dust and CMB are different: the CMB is a 2.725 K black-body and the polarized dust spectrum is typically modeled as a black-body with a power-law emissivity [31, 32]. When observing at multiple frequency

bands, the observations outside the CMB channel are used to extract the dust signal in the CMB channel. Since the spectral shape and amplitude of the polarized galactic dust signal are not known exactly, a robust foreground subtraction technique is essential for CMB polarimeters targeting the inflationary B-mode signal.

Chapter 3

The E and B Experiment

Searching the inflationary CMB B-mode signal has been an active research frontier in cosmology. Experimental efforts targeting the inflationary B-mode signal include ground based (BICEP/Keck, SPTpol, ACTpol), sub-orbital (EBEX, SPIDER, PIPER) and satellite (WMAP, Planck) CMB polarimeters. In this chapter I will briefly review the E and B Experiment (EBEX), a long-duration balloon-borne CMB polarimeter which had its long-duration science flight in December 2012. In Sec. 3.1, I will describe the science goals of EBEX. In Sec. 3.2, I will give an introductory description of the EBEX instrument and its current status.

3.1 EBEX Science

The EBEX was designed with following science goals:

1. To detect or set an upper limit of the inflationary CMB B-mode signal at low ℓ which probes the underlying physics of inflation;

2. To characterize the polarized galactic dust foreground and to determine its EE and BB power spectra in microwave regime;

3. To measure the CMB lensing B-mode signal and the power spectrum of lensing deflection angle with high signal to noise ratio;

4. To make a cosmic variance limited measurement of CMB E-mode signal for $20 < \ell < 1500$.

Fig. 3.1 shows the designed performance of EBEX after a 14-day long-duration balloon flight observing the planned EBEX patch which is a low-dust region in the southern hemisphere. The plot also includes the theoretical EE and BB power spectra in a standard cosmological model with tensor-to-scalar ratio of $r = 0.05$. The expected dust B-mode power spectrum in the planned EBEX sky patch at 150 GHz is also plotted. Even for a clean patch of the sky like the planned EBEX patch, the dust signal dominates the CMB inflationary B-mode signal and needs to be subtracted to get a correct estimate of the inflationary B-mode signal. To remove the dust foreground contamination in the CMB map, observation at higher frequency channel where the signal mainly comes from galactic dust is extrapolated down to the CMB channel and used as a template.

3.2 EBEX Instrument

EBEX is a long-duration balloon-borne microwave telescope. Being on a balloon platform allows EBEX to observe above 99% of the atmosphere, which eliminates atmospheric effects and gives EBEX access to frequency channels above 300 GHz that are not available to ground telescopes. I will discuss my simulations on atmospheric loading power for EBEX at balloon flight altitude in more detail in Chapter 7.

The EBEX telescope consists of a Gregorian Dragone-type telescope with a 1.5 m parabolic primary mirror and a 1 m ellipsoidal secondary mirror. EBEX observes at three frequency channels centered at 150, 250 and 410 GHz with bolometric transition edge sensor (TES) detectors. EBEX planned to observe a $\sim$400 deg^2 patch centered at RA = 55° and DEC = -45.5° in the southern sky with $8'$ resolution at all frequency channels. The patch size and resolution enable EBEX to cover the angular power spectrum between $20 < \ell < 1500$. Fig. 3.2 shows the planned EBEX patch over-plotted on the intensity map of the galactic thermal dust emission. This patch was selected because it is a low dust region that satisfies the anti-sun and elevation scanning constraint of EBEX. Many other ground-based and sub-orbital experiments (QUaD, QUIET, BOOMERANG, POLARBEAR2/Simons Array, SPIDER, SPTpol) including EBEX10k, the successor of EBEX, plans to observe or

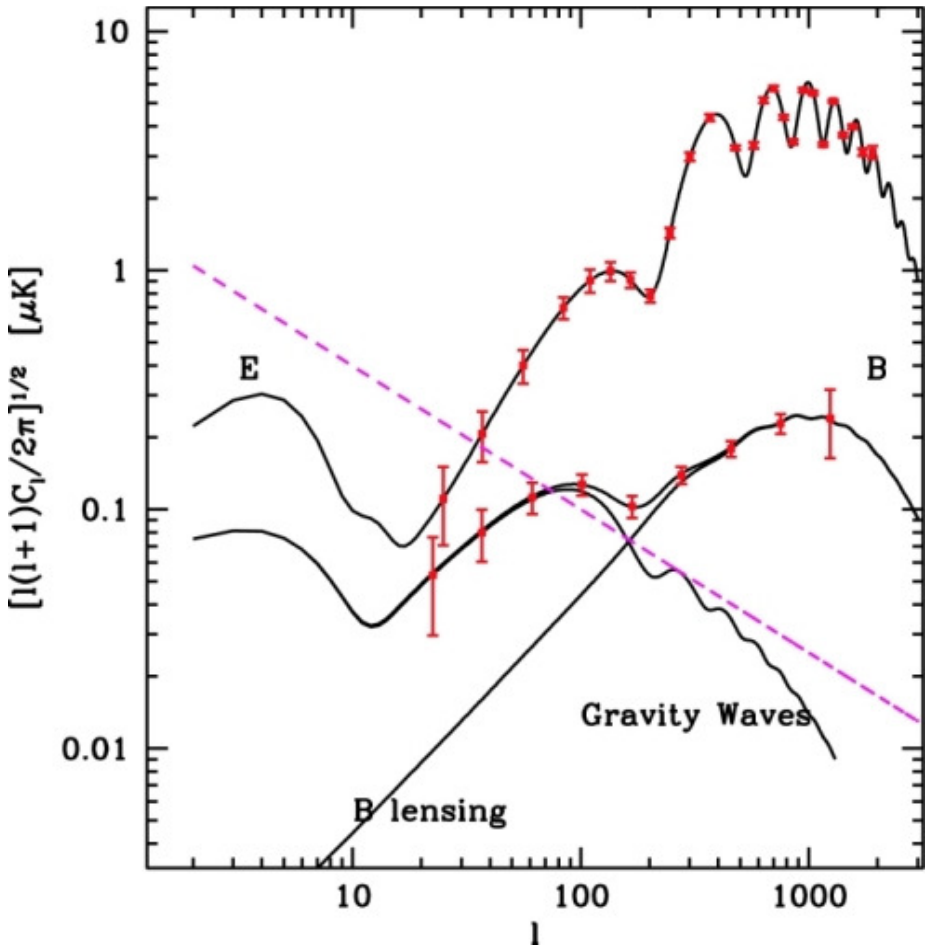

Figure 3.1: The predicted 1σ measurement of the E and B modes polarization power spectra with EBEX (red points and error bars). The solid lines are the theoretical predictions for EE and BB power spectra assuming a tensor-to-scalar ratio $r = 0.05$. The dashed magenta line is the predicted dust B-mode power spectrum at 150 GHz in the planned EBEX sky patch from WMAP data [28].

observed the same region of the sky.

The EBEX instrument can be divided into outer frame and inner frame. The outer frame is the support structure of the EBEX telescope [33]. The outer frame hosts the flight computers, data storage, power and pointing systems of the experiment. Fig. 3.3 shows the model of the EBEX outer frame and a photo of the integrated instrument. The inner frame of the EBEX contains the mirrors, the cryogenic receiver and the detector readout electronics [34]. The incoming light reflects off the primary and secondary mirror and then enters the cryogenic receiver. The cryogenic receivers hosts cold optics and the two focal planes. Fig. 3.4 shows a cut-away model of the cryogenic receiver and a photo of the cold optics. The cold optics consists the field lens and the AHWP which are kept at 4 K and the pupil lenses, polarizing grid and the camera lenses which are at 1 K. Keeping the optics at low temperature reduces the radiation emission power from the system which affects the sensitivity of the instrument.

Each EBEX focal plane consists of 7 wafers: one 410 GHz wafer in the center, two 250 GHz wafers and four 150 GHz wafers around the central wafer. Each wafer has 140 micro-fabricated transition edge sensor (TES) bolometers. TES bolometers used in EBEX are superconductors with critical temperature T_c at $\sim$500 mK. In operation the focal planes are cooled down to $\sim$250 mK [36]. The TES detectors are read out using a Superconducting QUantum Interference Devices (SQUIDs) based digital frequency domain multiplexing system (DfMUX) with a multiplexing factor of 16 [37].

The EBEX polarimeter consists of a continuously rotating AHWP, fixed wire-grid polarizer and the TES detectors. Fig. 3.5 shows the schematic model and a photo of the AHWP assembly [35]. When the AHWP is rotating at frequency f, a linearly polarized incident light is modulated at 4 f by the polarimeter. Any instrumental polarization downstream of the AHWP is not modulated and thus can be easily removed. When scanning, the sky signal resides in the side-bands of 4 f. Compared to polarimeters using pairs of polarization sensitive bolometers (PSB), the AHWP polarimeters turns every EBEX bolometer into an independent polarimeter, mitigating systematic effects such as gain difference, beam shape mismatch and scan pattern. Although AHWP polarimetry has great advantages, its behavior as a moving optical element is complicated. The characteristics of the AHWP needs to be understood for data analysis. My simulation on the AHWP frequency dependent

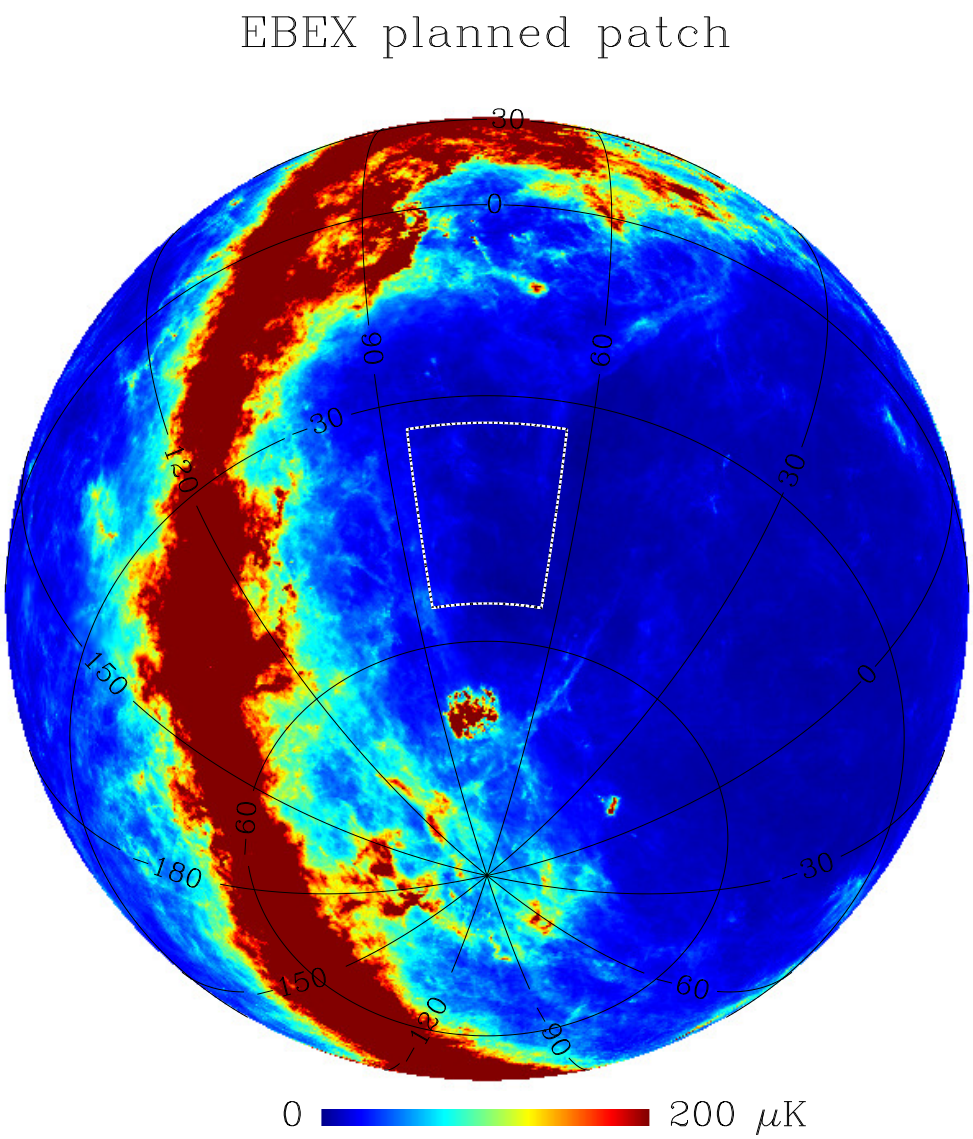

Figure 3.2: The planned EBEX patch in the southern hemisphere over-plotted on the intensity map of the polarized thermal dust emission in unit of thermodynamic temperature.

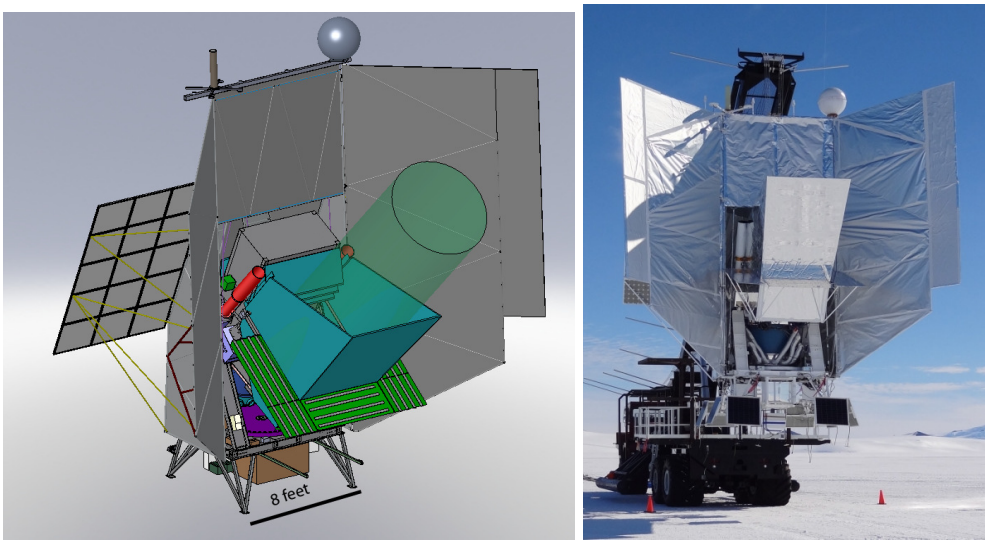

Figure 3.3: Model (left) and photo (right) of the EBEX outer frame. [34, 35].

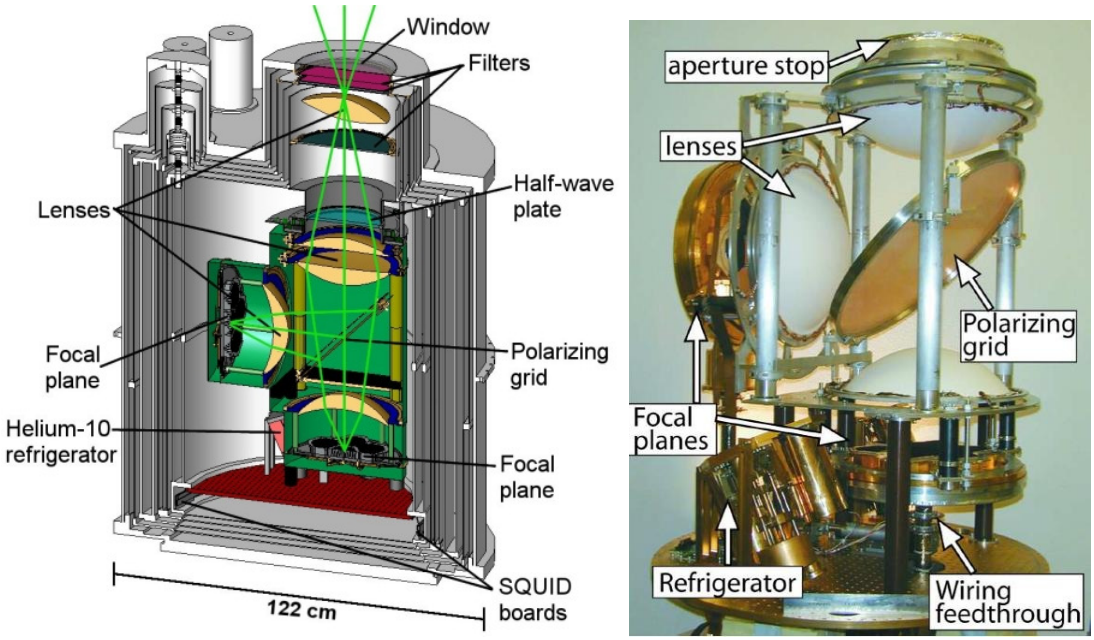

Figure 3.4: Model of the EBEX cryogenic receiver (left) and photo of the cold optics (right) of the EBEX [34, 35]. In the cold optics the polarizing grid split the incoming beam to two focal planes. The AHWP assembly is not included in the photo. [34, 35].

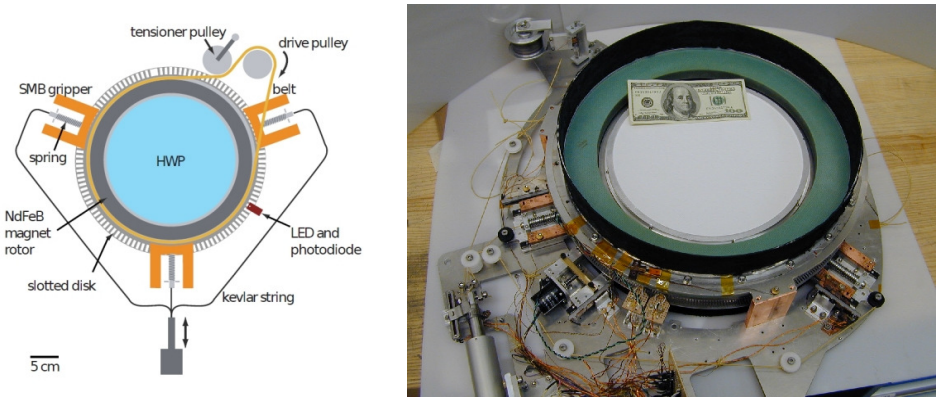

Figure 3.5: Model (left) and photo (right) of the EBEX AHWP [35].

response is discussed in Chapter 4.

EBEX had an engineering test flight in New Mexico in 2009 and a long duration science flight from Antarctica in December 2012. During the science flight EBEX was at float for 28 days and collected data for 12 days before the cryogens ran out as expected. EBEX had a total of 955 operating detectors during the science flight. The pivot motor controller overheated during the EBEX science flight, resulting in EBEX not being able to control azimuth pointing. The EBEX scan pattern had to be re-strategized and the final scan area is a 6000 deg^2 constant DEC strip between $-66° < \mathrm{DEC} < -40°$. The data collected during science flight is being analyzed right now.

Chapter 4

Performance Simulation of an Achromatic Half-Wave Plate

The CMB B-mode signal has a polarization fraction P of less than 10^{-8} at low ℓ and 10^{-7} at high ℓ. At low ℓ the B-mode signal is dominated by the inflationary B-mode signal and at high ℓ it is dominated by the lensing B-mode signal. To ensure the spurious B-mode signal generated from the instrumental leakage of E to B is less than 10% of the lensing B-mode signal, the polarization angle α of the CMB needs to be measured with $< 0.3^{\circ}$ accuracy [38]. To mitigate systematic effects and measure polarization accurately, some CMB experiments [39, 30, 40] use half-wave plate (HWP) polarimetry. Various previous studies have been conducted to assess the performance of HWP polarimetry used in CMB experiments [41, 42, 43, 44]. In this chapter, I will discuss my work on simulations of the spectral response of an achromatic half-wave plate (AHWP) and its dependence on various characteristics of the AHWP, the input polarization and the observation band. In Sec. 4.1 I will briefly overview the mathematical model of HWP polarimetry. In Sec. 4.2 I will show the simulation results of the spectral response of an AHWP with various sets of parameters and their comparison with other predictive models and measured data.

4.1 Half-wave plate polarimetry model

For EBEX, whose detectors are bolometric power detectors, polarimetry consists of a continuously rotating AHWP and a wire grid polarizer. Throughout this chapter, we use Stokes vectors and Mueller Matrices to describe polarization in the simulation. In this section I will layout the formalism of the model and introduce terminologies used in the chapter. First I will introduce the formalism of Stokes vector and Mueller matrix in Sec. 4.1.1. In Sec. 4.1.2 I will describe the model for single HWP polarimetry. I will then expand the model to broadband AHWP polarimetry in 4.1.3. The flow of this section largely follows Chapter 3 in the thesis of T. Matsumura, a former Cosmolab member [45]. There are a few discrepancies in some definitions to ensure the math is consistent and I will highlight these discrepancies in the text.

4.1.1 Stokes vector and Mueller matrices

Stokes vector and Mueller matrices are commonly used mathematical tools to describe polarization. The Stokes vector is defined as

$$\vec{s} = \begin{pmatrix} I \\ Q \\ U \\ V \end{pmatrix} = \begin{pmatrix} I \\ Ip\ cos2\alpha\ cos2\beta \\ Ip\ sin2\alpha\ cos2\beta \\ Ip\ sin2\beta \end{pmatrix}. \tag{4.1}$$

Here I is the total intensity of the light, p is the polarization fraction, α is the polarization angle with respect to a reference coordinate system and β is the ellipticity. Q and U parameters describe the linear polarization of the light and V describes the circular polarization. When $\beta = 0$ then $V = 0$ and the light is linearly polarized. Since CMB is expected to be linearly polarized, V **is assumed to be 0 throughout this chapter**. For linearly polarized light, the polarization fraction is

$$p = \frac{\sqrt{Q^2 + U^2}}{I}. \tag{4.2}$$

When $p = 1$ the light is fully polarized and when $p = 0$ the light is unpolarized.

A Mueller matrix is a 4×4 matrix which is used to manipulate the Stokes vector. For

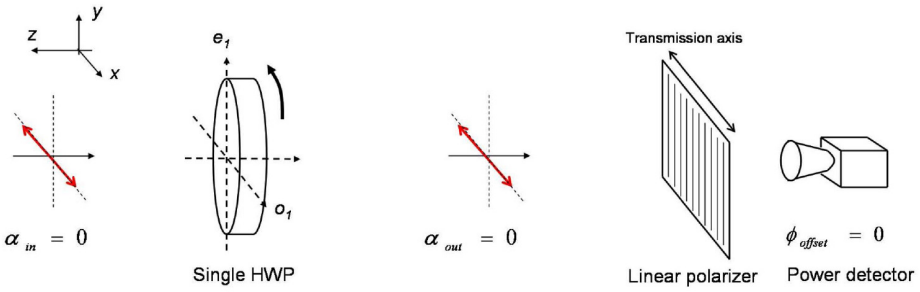

Figure 4.1: Schematic plot of a HWP polarimetry including a linear polarizer and power detector [41]. Here we define the transmission axis of the linear polarizer as the x-axis of the system.

partially polarized incoherent light, Mueller matrix is used to describe the polarization. For all the calculations in this chapter, we use Mueller matrices to describe optical elements and operations to polarized light.

4.1.2 Single HWP polarimetry model

A half-wave plate (HWP) is a type of retarder. It is an optical element that changes the polarization angle of linearly polarized light. A HWP is made of birefringent material, whose index of refraction is different along different directions. We consider a polarimetry which consists of a continuously rotating HWP at frequency f_0, a fixed linear polarizer and a power detector such as a bolometer, which is used in EBEX. A schematic drawing of the system is shown in Fig. 4.1. Here we define the direction of the transmission axis of the linear polarizer as the 0° direction and x-axis. The rotation angle ρ of the HWP is 0° when its optical axis is aligned with the x-axis.

Given the system described, the HWP polarimetry of a single frequency light can be modeled in Mueller matrix formalism as follows:

$$\vec{S}_{out} = GR(\rho)\Gamma R(-\rho)\vec{S}_{in}(\alpha_{in}, p_{in}, \nu). \tag{4.3}$$

Compared to Eq. 3.7 in Matsumura's thesis [45], the positions of the $R(\rho)$ and $R(-\rho)$ terms are switched in Eq. 4.3. Here $\vec{S}_{out}$ is the output Stokes vector; the input Stokes vector $\vec{S}_{in}$ is partially linearly polarized and characterized by polarization angle α_{in} and polarization

fraction p_{in}, specifically

$$\vec{S}_{in} = (I_{in}, Q_{in}, U_{in}, 0) \tag{4.4}$$
$$= (I_{in}, p\ I_{in}\ cos2\alpha_{in}, p\ I_{in}\ sin2\alpha_{in}, 0) \tag{4.5}$$
$$= I_{in}(1, p\ cos2\alpha_{in}, p\ sin2\alpha_{in}, 0). \tag{4.6}$$

G is the Mueller matrix of the linear polarizer. In the coordinate system defined above the transmission axis of the polarizer is aligned with the x-axis and thus

$$G = \frac{1}{2}\begin{pmatrix} 1 & 1 & 0 & 0 \\ 1 & 1 & 0 & 0 \\ 0 & 0 & 0 & 0 \\ 0 & 0 & 0 & 0 \end{pmatrix}. \tag{4.7}$$

Γ is the Mueller matrix of a retarder. For a retarder whose fast axis is aligned with the 0° direction, it is defined as

$$\Gamma(\delta) = \begin{pmatrix} 1 & 0 & 0 & 0 \\ 0 & 1 & 0 & 0 \\ 0 & 0 & cos\ \delta & sin\ \delta \\ 0 & 0 & -sin\ \delta & cos\ \delta \end{pmatrix}, \tag{4.8}$$

where δ is the retardance of the HWP. The Sin terms in the definition of Γ have opposite signs as the definition in Sec. 3.3.1 of Matsumura's thesis [45]. The retardance δ is a function of the thickness of the HWP d, the ordinary and extraordinary indices of refraction n_o and n_e and the frequency of the incident light ν. Specifically,the retardance is expressed as

$$\delta = 2\pi\frac{\nu}{c}|n_e - n_o|d. \tag{4.9}$$

Compared to the equation in Matsumura's thesis [45], the retardance here is proportional to the absolute value of $n_e - n_o$ which accounts for the situation where $n_e < n_o$. For a given HWP the retardance δ varies linearly with ν. Typically a HWP is optimized at a particular frequency such that $\delta(\nu_{opt}) = \pi$. When the HWP is rotated by angle ρ, its

Mueller matrix becomes $R(\rho)\Gamma R(-\rho)$ where R is a rotation matrix

$$R(\rho) = \begin{pmatrix} 1 & 0 & 0 & 0 \\ 0 & cos2\rho & -sin2\rho & 0 \\ 0 & sin2\rho & cos2\rho & 0 \\ 0 & 0 & 0 & 1 \end{pmatrix}. \tag{4.10}$$

The definition of the rotation matrix R here has an extra factor of 2 in front of the angle in the Cos and Sin terms compared to the definition (Eq. 3.10) in Matsumura's thesis [45]. Given Eq. 4.8 and Eq. 4.10, we have

$$R(\rho)\Gamma R(-\rho) = \begin{pmatrix} 1 & 0 & 0 & 0 \\ 0 & cos^2\frac{\delta}{2} + cos4\rho\ sin^2\frac{\delta}{2} & sin4\rho\ sin^2\frac{\delta}{2} & -sin2\rho\ sin\delta \\ 0 & sin4\rho\ sin^2\frac{\delta}{2} & cos^2\frac{\delta}{2} - cos4\rho\ sin^2\frac{\delta}{2} & cos2\rho\ sin\delta \\ 0 & sin2\rho\ sin\delta & -cos2\rho\ sin\delta & cos\delta \end{pmatrix} \tag{4.11}$$

From Eq. 4.3, Eq. 4.6 and Eq. 4.11 we can derive that the detected intensity I_{out}

$$I_{out} = \frac{1}{2}I_{in}(1 + p\ cos2\alpha_{in}\ cos^2\frac{\delta}{2}) + \frac{1}{2}I_{in}p\ sin^2\frac{\delta}{2}\ cos[4(\rho - \frac{\alpha_{in}}{2})]. \tag{4.12}$$

As seen in Eq. 4.12, the detected intensity I_{out} is a function of ρ, which we call an intensity vs angle curve (IVA curve). The first term is a constant term and the second term varies with HWP angle ρ. When ρ changes with a frequency f_0, I_{out} is modulated at $4f_0$. We define the phase ϕ of the IVA curve as

$$(I_{out})_{varying\ term} \propto cos[4(\rho - \phi)]. \tag{4.13}$$

Given this definition, ϕ is the location of the first maximum of the IVA curve on the ρ axis. For a single HWP the phase of the IVA curve is related to the polarization angle of the incoming light α_{in}

$$\phi = \frac{\alpha_{in}}{2} \tag{4.14}$$

A useful metric for characterizing polarimeters is 'modulation efficiency', which is defined as

$$\epsilon = \frac{p_{out}}{p_{in}}. \tag{4.15}$$

Here p_{out} is the measured polarization fraction

$$p_{out} = \frac{I_{out\_max} - I_{out\_min}}{I_{out\_max} + I_{out\_min}}, \tag{4.16}$$

where I_{out_max} and I_{out_min} are the maximum and minimum of the IVA. The modulation efficiency ϵ characterizes the de-polarization caused by the polarimeter.

For the HWP polarimeter discussed above, the I_{out_max} and I_{out_min} occurs at $\rho = \frac{\alpha_{in}}{2}$ and $\rho = \frac{\alpha_{in}}{2} + \frac{\pi}{4}$ respectively. With linearly polarized incoming light, we have

$$I_{out\_max} = \frac{1}{2} I_{in}(1 + p_{in}\ cos2\alpha_{in}\ cos^2\frac{\delta}{2}) + \frac{1}{2} I_{in} p_{in}\ sin^2\frac{\delta}{2} \tag{4.17}$$

$$I_{out\_min} = \frac{1}{2} I_{in}(1 + p_{in}\ cos2\alpha_{in}\ cos^2\frac{\delta}{2}) - \frac{1}{2} I_{in} p_{in}\ sin^2\frac{\delta}{2}, \tag{4.18}$$

and

$$p_{out} = \frac{p_{in} sin^2\frac{\delta}{2}}{1 + p_{in} cos^2\frac{\delta}{2}\ cos2\alpha_{in}}. \tag{4.19}$$

Consequently the measured modulation efficiency is

$$\epsilon = \frac{sin^2\frac{\delta}{2}}{1 + p_{in} cos^2\frac{\delta}{2}\ cos2\alpha_{in}}. \tag{4.20}$$

We notice from Eq. 4.20 that the measured modulation efficiency is not constant. As seen in Eq. 4.9, the retardance δ depends linearly on ν for a given HWP. So the modulation efficiency is a function of frequency ν, incoming polarization fraction p_{in} and angle α_{in}. Fig. 4.2 shows how the modulation efficiency varies with α_{in} and ν when p_{in} is set to 1. In polarization calibration measurements the incoming polarization fraction is typically close to 1. As seen in Fig. 4.2, only at the optimized frequency ν_{opt} where $\delta = \pi$ we always have the modulation efficiency $\epsilon = 1$ regardless the values of p_{in} and α_{in}. At all other frequencies, ϵ is not constant with different p_{in} and α_{in}. In the limit of $p_{in} \ll 1$ or when

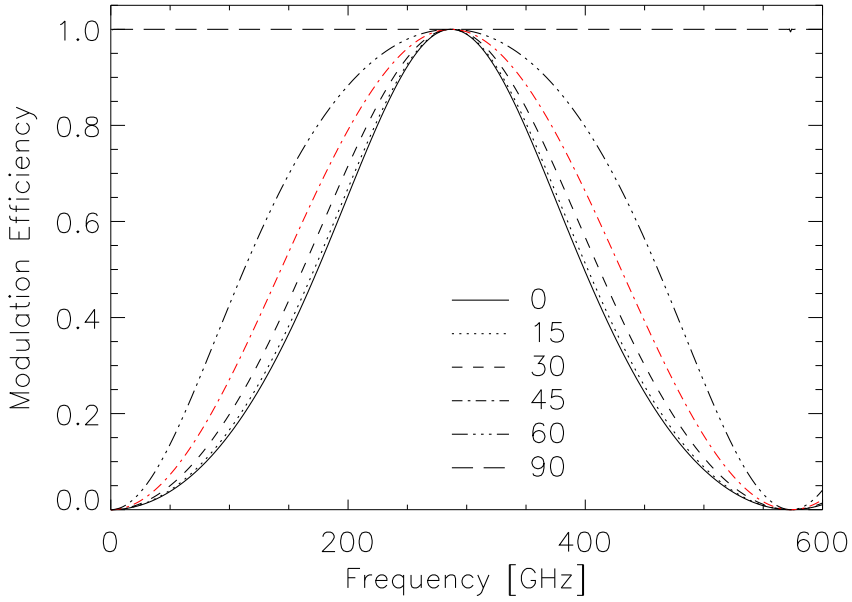

Figure 4.2: Modulation Efficiency as a function of frequency with incoming polarization angles of $0°, 15°, 30°, 45°, 60°$ and $90°$. Here we fix the incoming polarization fraction p_{in} at 100% which is close to the case in polarization calibration measurement. In this calculation we use an ideal sapphire HWP optimized at 290 GHz as an example. In the limit of $p_{in} \ll 1$ or when $\alpha_{in} = 45°$ the modulation efficiency vs frequency curve converges at the $\alpha_{in} = 45°$ line shown in red here.

$\alpha_{in} = 45°$, the modulation efficiency reduces to

$$\epsilon = sin^2 \frac{\delta}{2}, \tag{4.21}$$

which is the red curve in Fig. 4.2.

4.1.3 Achromatic half-wave plate polarimetry

When the measurement is over a range of frequencies, single HWP polarimetry is not suitable anymore. As shown in Sec. 4.1.2 a single HWP polarimeter can only achieve 90% modulation efficiency over ∼25% band around the optimal frequency. In the case of

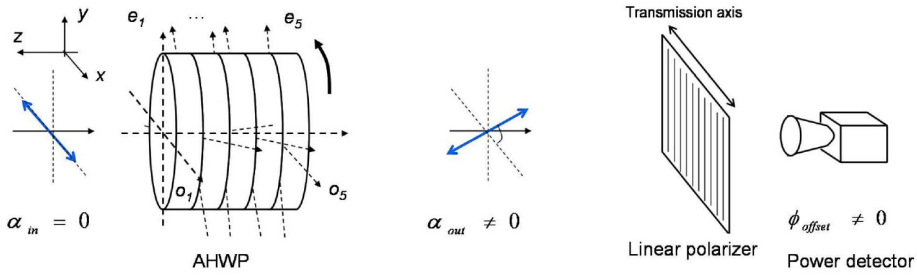

Figure 4.3: Schematic plot of a polarimetry with a five-stack AHWP, a linear polarizer and a power detector [41]. Here we define the transmission axis of the linear polarizer as the x-axis of the system.

broad band measurements, an achromatic half-wave plate (AHWP) is used to achieve high modulation efficiency. An AHWP consists of a stack of single HWPs with their optical axes rotated relative to each other. With specific choices of the number of HWPs and their relative orientation angles, an AHWP can achieve nearly 100% modulation efficiency over a broad range of frequencies [46].

A schematic drawing of a polarimeter with a five-stack AHWP is shown in Fig. 4.3. Similar to the single HWP polarimetry, the polarimeter consists of a continuously rotating AHWP at f_0, a fixed linear polarizer and a bolometer. The transmission axis of the linear polarizer is defined as the x-direction and 0° angle. The optical axes of the HWPs in the stack are offset with respect to each other. The array of relative orientation angles starting from the first plate is denoted as $\vec{\theta}$ and the orientation of the i^{th} plate is denoted as θ_i. The rotation angle of the AHWP is labeled as ρ. When $\rho = 0$ the fast axis of the first plate in the stack is aligned with x-axis.

An m-stack AHWP polarimeter can be modeled in Mueller matrix formalism as

$$\vec{S}_{out} = G \prod_{i=1}^{m} [R(\rho + \theta_i)\Gamma_i R(-\rho - \theta_i)] \vec{S}_{in}(\alpha_{in}, p_{in}, \nu), \tag{4.22}$$

where $\prod_{i=1}^{m} [R(\rho+\theta_i)\Gamma_i R(-\rho-\theta_i)]$ is the Mueller matrix of the m-stack AHWP. Eq. 4.22 represents the polarimetry model for light at a single frequency. For observation over a broad

band, we can write the total in-band Stokes vector $\langle \vec{S}_{out} \rangle$ as

$$\langle \vec{S}_{out} \rangle = \int_0^\infty G \prod_{i=1}^{m} [R(\rho + \theta_i)\Gamma_i R(-\rho - \theta_i)] \vec{S}_{in}(\alpha_{in}, p_{in}, \nu)\ T(\nu) d\nu. \tag{4.23}$$

Here $T(\nu)$ is the frequency band transmission function that describes the spectral response of the instrument. When computing the $\langle \vec{S}_{out} \rangle$ numerically, a discrete summation of Stokes vectors calculated over small intervals of frequency is performed instead of the analytical integral. Specifically, $\langle I_{out} \rangle$ is the summation of a group of sinusoidal curves with frequency $4f_0$, which also has frequency $4f_0$.

Fig. 4.4 shows the IVA curves for a 5-stack AHWP with incoming polarization angle $\alpha_{in} = 0$ at 150 GHz, 250 GHz and 410 GHz. In the case of a single HWP, the IVA phase $\phi = \frac{\alpha_{in}}{2}$ while for AHWP

$$\phi = \phi'(\nu, d, \vec{\theta}) + \frac{\alpha_{in}}{2}. \tag{4.24}$$

The AHWP IVA phase has a frequency dependence which means even for the same polarization angle α_{in} the IVAs at different frequencies are not in phase. The analysis in this chapter is focused on addressing the phase offset $\phi'(\nu, d, \vec{\theta})$. The polarization angle of the incoming signal α_{in} is set to 0 in the rest of this chapter.

For observations over a band, the shape of the band transmission function and the incoming polarization spectrum will affect the addition of all the IVAs and thus affect the total in-band IVA phase offset. These two effects are addressed individually in Sec. 4.2.4 and Sec. 4.2.5 and together in Sec. 4.2.6.

In the data analysis process, we need to know the frequency dependent AHWP IVA phase offset in order to be able to extract the CMB polarization angle. Given Eq. 4.24 if the IVA phase offset is not determined properly, it will induce an error in determining α_{in}. This is equivalent to a rotation of the polarization which causes E-B mixing and biases the final extraction of B-mode signal. So for CMB experiments targeting the B-mode, being able to calibrate the rotation effect of the AHWP is essential.

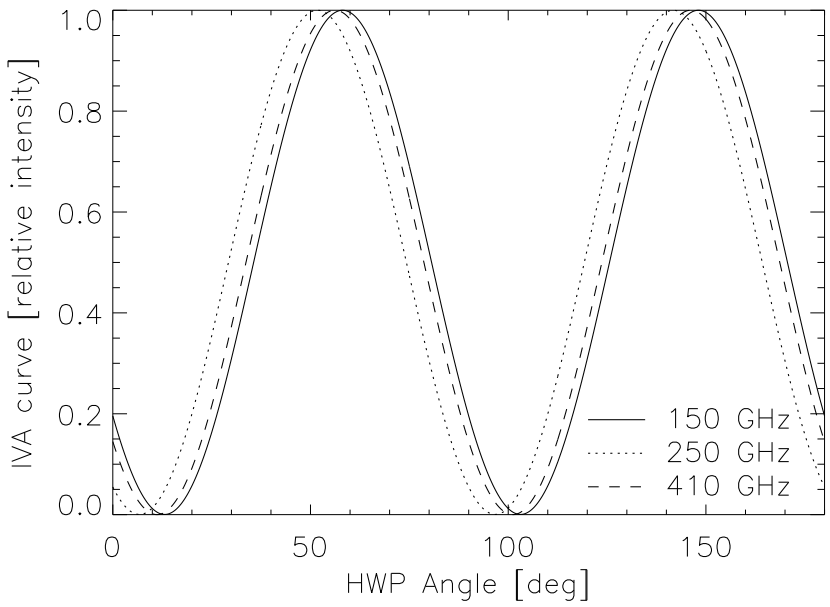

Figure 4.4: IVA curves for an example five-stack AHWP at 150 GHz, 250 GHz and 410 GHz. The input polarization angle α_{in} is set to 0° for all frequencies. The IVA curves of different frequencies are not in phase even with the same α_{in}.

Indices of refraction [47, 48, 49]	$n_o = 3.047, n_e = 3.361$
Thickness of single HWP	$d = 1.65$ mm
Relative orientation of the stack	$\vec{\theta} = (0°, 28°, 94°, 28°, 0°)$
Resolution of AHWP angle	$\Delta\rho = 0.1°$

Table 4.1: Design parameters of EBEX five-stack sapphire AHWP.

4.2 Modeling the AHWP frequency dependent rotation

In this section, we assess the relationship between the AHWP frequency dependent rotation effect and various parameters, including the indices of refraction of sapphire, the relative orientation angles between the HWPs in the stack, the thicknesses of the HWPs in the stack, the observation band shapes and the incoming signal spectra. The end goal of this analysis is to generate a realistic AHWP model that fits the polarization calibration data.

As a starting point, the designed EBEX five-stack AHWP is used as the baseline example in the simulation. The specific parameters of the AHWP are listed in Table 4.1. The AHWP is made of sapphire and each of HWPs in the stack is optimized for 290 GHz with a thickness of 1.65 mm. The nominal operation temperature of the AHWP is 4 K so the indices of refraction of sapphire at cryogenic temperature are used. The IVA phase offset as a function of frequency for the designed EBEX AHWP is shown in Fig. 4.5. The IVA phase offset curve is relatively flat near the optimal frequency, from ∼220 GHz to ∼360 GHz, and then increases further away from the optimal frequency. Across the $100 - 500$ GHz frequency range, the IVA phase shift varies by $\sim 16°$ and the curve is symmetric around the optimized frequency.

4.2.1 Indices of refraction

When installed inside the receiver, the EBEX AHWP was operated at cryogenic temperature. The indices of refraction of sapphire at cryogenic temperature are used in baseline parameters. Before the installation of the EBEX AHWP, EBEX collaborator W. Grainger at Cardiff University performed spectroscopic measurement of the AHWP at room temperature. The ordinary and extraordinary indices of refraction of sapphire have a temperature dependence. Here we first address the effect of the temperature dependence of indices of

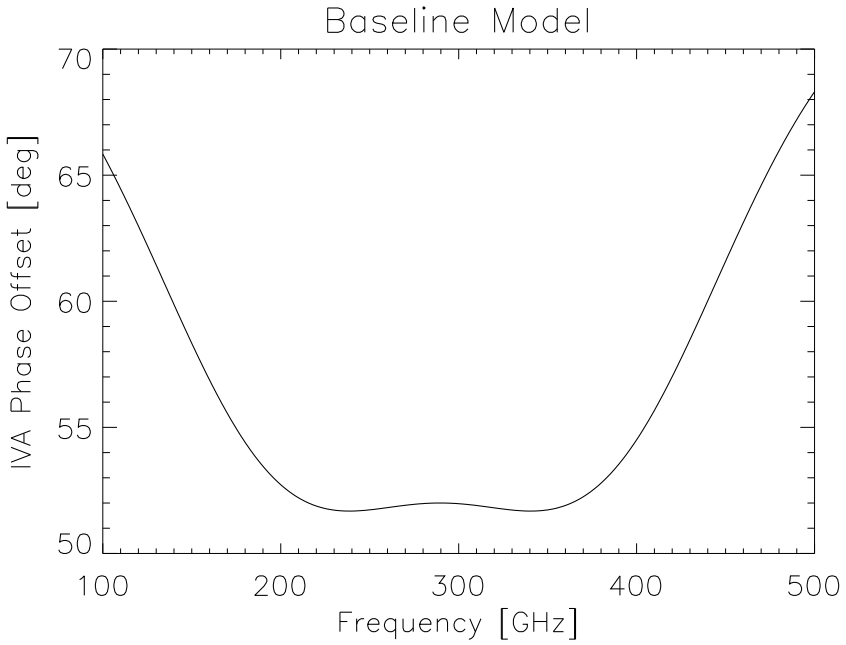

Figure 4.5: IVA phase offset as a function of frequency of incoming polarization for the baseline simulation. In the simulation we use the design parameters of the EBEX AHWP, which are listed in Table 4.1.

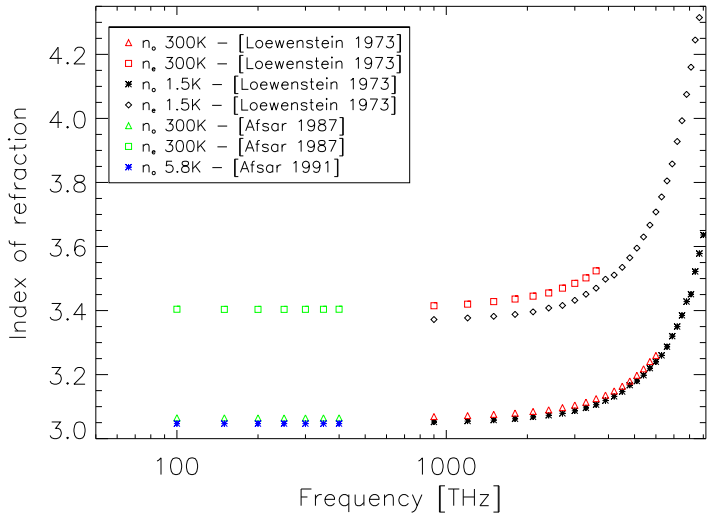

Figure 4.6: Measured indices of refraction of sapphire as a function of frequency at room temperature and cryogenic temperature [47, 50, 48, 49].

refraction on AHWP IVA phase offset.

Fig. 4.6 shows the measured indices of refraction of sapphire at both cryogenic and room temperature in millimeter wave and far infrared [47, 48, 50]. From measurements in millimeter wave regime [48, 50], the ordinary and extraordinary indices of refraction of sapphire are approximately constant in the EBEX frequency range. Due to the lack of experimental data of n_e of sapphire at cryogenic temperature, we extrapolate the measurements at higher frequencies [47, 49]. The values of n_o and n_e are listed in Table 4.2.

Fig. 4.7 shows the IVA phase offset as a function of frequency for a five-stack sapphire AHWP using constant indices of refraction at room temperature. For comparison we also show the curve from the baseline simulation in which the same AHWP at cryogenic temperature is used. Changing the indices, particularly the difference between n_o and n_e as shown in the definition of retardance Eq. 4.9, shifts and squeezes/stretches the IVA phase offset vs frequency curve.

Although it is a good approximation to assume that the indices of refraction of sapphire

Temperature (K)	n_o	n_e
300	3.065	3.404
5.8	3.047	3.361

Table 4.2: Indices of refraction of sapphire at 300 K [47, 48] and 5.8 K [47, 50]. The extraordinary index of refraction at cryogenic temperature is extrapolated from measurements at higher frequencies [49].

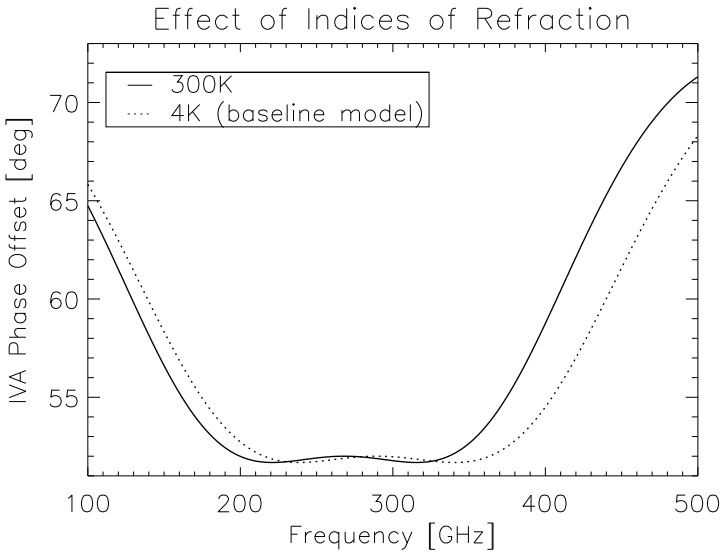

Figure 4.7: IVA phase offset as a function of frequency for the EBEX AHWP at 300 K(solid) and the baseline model at 4 K(dotted) as a comparison. The indices of refraction of sapphire at room temperature are used to generate the solid curve. Specifically, we have $n_o = 3.065$ and $n_e = 3.404$. All the rest of the parameters are the same as the ones listed in Table 4.1. The difference between the solid and the dotted curves is the due to the temperature dependence of n_e and n_o.

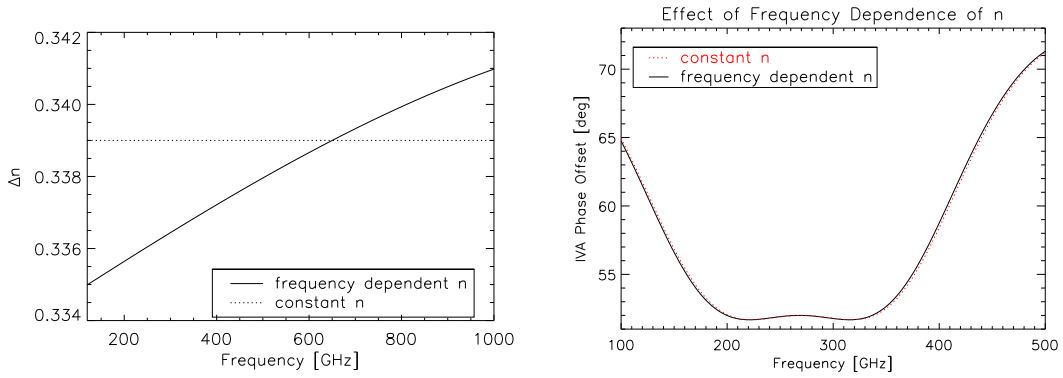

Figure 4.8: Comparison of $\Delta n = n_e - n_o$ (left) and ϕ (right) between cases where frequency dependent [42] (solid) or constant [47, 50, 48, 49] (dotted) indices of refraction of sapphire at room temperature are used. The difference of the AHWP IVA phase offset is small between the two cases.

are constant across the EBEX frequency range, n_o and n_e of sapphire have slight frequency dependence. Measurements of the refractive indices of sapphire at room temperature from 120 GHz to 1 THz are reported in Savini *et al.*, 2006 [42], where the authors express n_o and n_e as empirical polynomial functions of frequency in units of GHz:

$$n_o(\nu) = 3.053 + 4.7 \times 10^{-6}\nu + 2.2 \times 10^{-10}\nu^2 + 1.1 \times 10^{-12}\nu^3, \tag{4.25}$$

and

$$n_e(\nu) = 3.387 + 1.3 \times 10^{-5}\nu. \tag{4.26}$$

Fig. 4.8 shows the comparisons of $\Delta n = n_e - n_o$ and IVA phase offset vs frequency curves between the two cases where we use frequency dependent indices of refraction [42] or constant indices of refraction listed in Table 4.2. Here we compare Δn instead of n_o and n_e because Δn is the quantity that changes the retardance δ as seen in Eq. 4.9. Given the magnitude of difference in Δn between the two cases, the effect on the IVA phase offset angle vs frequency curve is small.

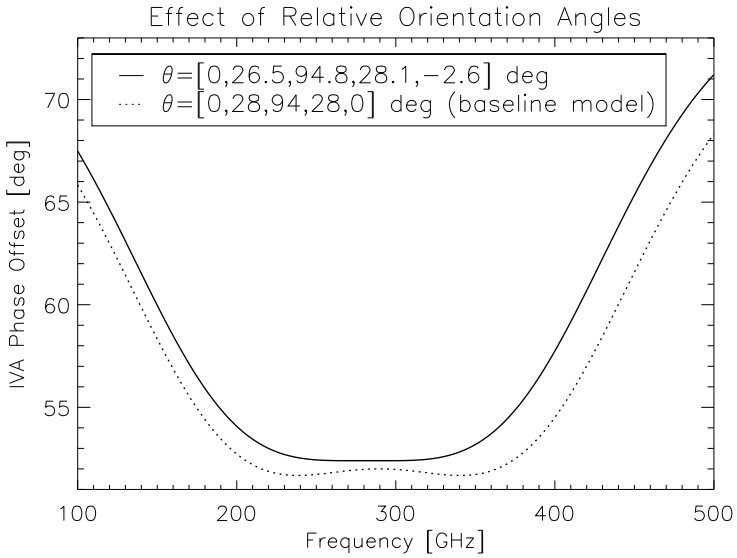

Figure 4.9: IVA phase offset as a function of frequency for the EBEX AHWP at cryogenic temperature using the best fit relative orientation angles between the plates (solid). The best fit relative orientation angles of the EBEX AHWP plate are $\vec{\theta}$=[0°, 26.5°, 94.8°, 28.1°, -2.6°]. The rest of the parameters are the same as the ones used in the baseline model, which are listed in Table 4.1. The baseline simulation (dotted line) is also plotted for comparison.

4.2.2 Relative orientation of the plates

When an AHWP is built, there is a difference between the designed and the actual relative orientations of the plates. From the spectroscopic data of the AHWP measured at Cardiff University [41], EBEX collaborator G. Savini found the best fit relative orientation angles of the plates are $\vec{\theta} = (0°, 26.5°, 94.8°, 28.1°, -2.6°)$ with respect to the optical axis of the first plate in the stack.

Fig. 4.9 shows the AHWP IVA phase offset vs frequency curve for the best fit orientation angles compared to the nominal case. With the best fit relative orientation angles, the IVA phase offset is increased by $[1.6°, 0.7°, 3.5°]$ at [150 GHz, 250 GHz, 410 GHz], respectively, compared to the baseline model. A more detailed study of the dependence of IVA phase offset on relative orientation of the stack can be found in Matsumura's thesis [41].

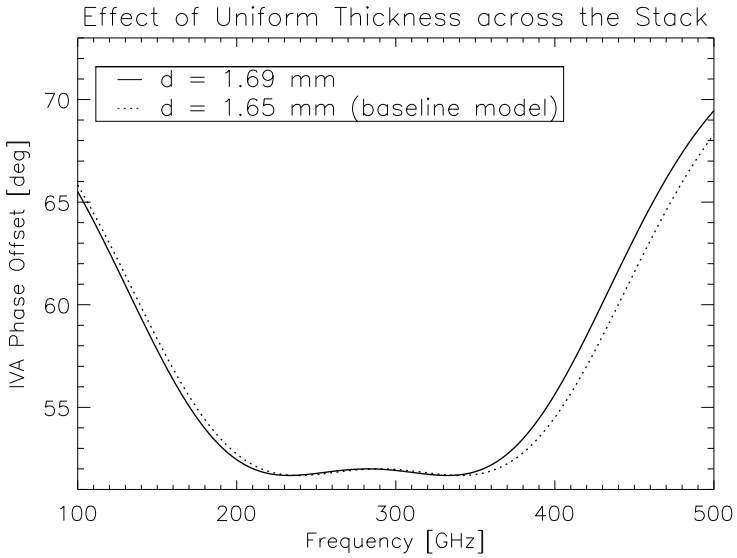

Figure 4.10: IVA phase offset as a function of frequency for a five-stack AHWP with the thickness of each individual plate set to $d = 1.69$ mm (solid). The rest of the AHWP parameters are the same as the ones used in the baseline simulation, which are listed in Table 4.1. Compared to the baseline model (dotted), the curve is shifted to the lower frequency side and flat part around the optimal frequency is narrower.

4.2.3 Thickness of the plates

In the baseline AHWP model, the thickness d of each of the single HWPs in the stack is assumed to be the same. Under this assumption, changing d has the same effect on the IVA phase offset vs frequency curve as changing Δn, which is shown in Eq. 4.9. Fig. 4.10 shows a simulation result for a five-stack AHWP with the thickness of each single HWP changed from 1.65 mm in the baseline model to 1.69 mm. We choose 1.69 mm as an example here because the uncertainty of the HWP thickness measurement is ~ 0.02 mm and 1.69 is 2-σ from the designed thickness. Compared to the baseline model, the simulated ϕ vs ν curve here is changed the same way as when Δn is increased, which is shown in Fig. 4.7.

In practice, the thicknesses of the single HWPs in the stack are slightly different from each other. EBEX collaborator G. Savini both fitted the thicknesses of the HWPs from spectroscopic data [41] and measured the thicknesses of each HWPs in the EBEX AHWP

HWP number	1	2	3	4	5
Best fit thickness [mm]	1.665	1.677	1.648	1.675	1.640
Average measured thickness [mm]	1.655	1.657	1.636	1.647	1.657
RMS of measured thickness [mm]	0.016	0.015	0.017	0.013	0.013
Weighed thickness from measurement [mm]	1.656	1.656	1.634	1.644	1.657

Table 4.3: Thicknesses of the single HWPs in the EBEX AHWP from best fit of the spectroscopic data and direct measurements. The average measured thicknesses are calculated from the measurements of 77 different locations across each plate. The best fit thicknesses are within 3-σ of the measurement.

across various locations on the plates. Table 4.3 lists the best fit and the measurement of the thicknesses of the single HWPs.

We use the best fit thicknesses of the HWPs in the simulation. Fig. 4.11 shows the simulated IVA phase offset as a function of frequency and its comparison with the baseline model. Varying the thicknesses of the plates makes the curve asymmetric around the optimal frequency. A more thorough exploration of the behavior of the IVA phase offset $\phi(\vec{d}, \nu)$ as a function of the thicknesses of each plate $\vec{d}$ and frequency can be a topic for future study.

4.2.4 Observation frequency band

In all the simulations above we assess the frequency dependent AHWP rotation effect at a single frequency. In practice the CMB observations are performed over a band that has a certain shape. For a **flat** incoming signal spectrum (the effect of incoming signal spectrum is addressed in Sec. 4.2.5), the band shape affects the relative amplitude between IVAs at various frequencies and thus modifies the band averaged IVA phase offset as seen in Eq. 4.23. In this section we use AHWP parameters at cryogenic temperature because the EBEX AHWP is nominally operated at cryogenic temperature. Due to the lack of data for n_e and n_o of sapphire as a function of ν at such temperature, we use constant indices of refraction in the simulation. For the thicknesses $\vec{d}$ and relative orientation angles $\vec{\theta}$, we use the best fit values from spectroscopic data taken by EBEX collaborator G. Savini [41]. The polarization angle α_{in} is set to 0° at all frequencies. The detailed simulation parameters are listed in Table 4.4. Fig. 4.12 shows the IVA phase offset as a function of

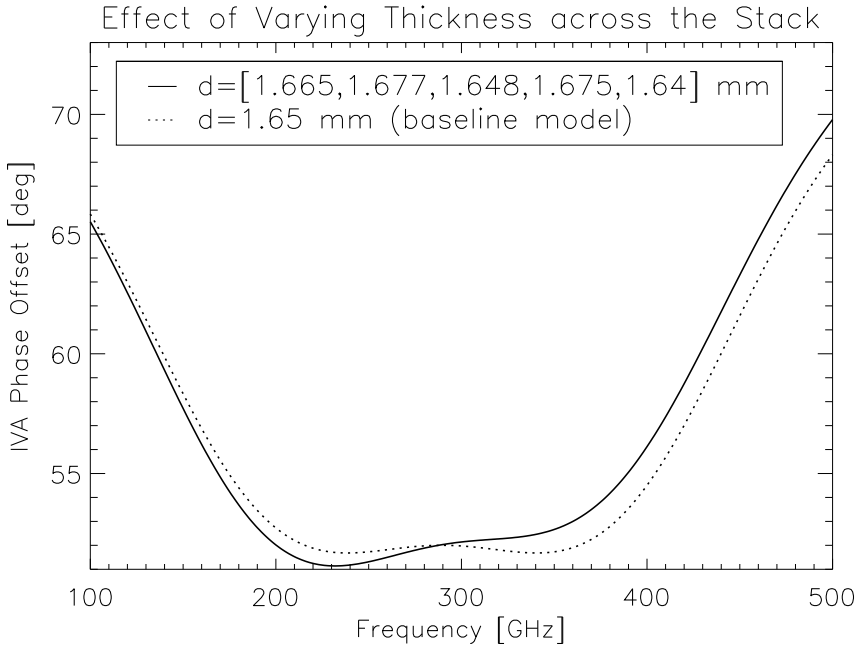

Figure 4.11: IVA phase offset vs frequency for the EBEX AHWP with varying thicknesses of the single HWPs across the stack (solid). The best fit thicknesses for each single HWP in the EBEX AHWP are [1.665, 1.677, 1.648, 1.675, 1.64] mm. The rest of the AHWP parameters used in the simulation are listed in Table 4.1. The baseline model (dotted) with 1.65 mm uniform thickness of the single HWPs in the stack is also shown for comparison. With varying thicknesses of the HWPs in the stack the ϕ vs ν curve is no longer symmetric around the optimal frequency.

Ordinary index of refraction [47, 48]	3.047
Extraordinary index of refraction [47, 49]	3.361
Thickness of HWPs in the stack	$\vec{d} = [1.665, 1.677, 1.648, 1.675, 1.64]$ mm
Relative orientation of the stack	$\vec{\theta} = (0°, 26.5°, 94.8°, 28.1°, -2.6°)$
Resolution of AHWP angle	$\Delta\rho = 0.1°$
Resolution of frequency	$\Delta f = 1.0\ GHz$

Table 4.4: Best fit parameters of EBEX five-stack sapphire AHWP at cryogenic temperature and other parameters used in the IVA phase offset simulations.

Top-hat band	Band averaged IVA phase offset
Broadband [0, 600] GHz	59.47°
EBEX 150 GHz band [133, 173] GHz	57.47°
EBEX 250 GHz band [217, 288] GHz	52.21°
EBEX 410 GHz band [366, 450] GHz	59.55°

Table 4.5: Band averaged IVA phase offset angles $\langle\phi\rangle$ for various top-hat bands, including a broad band from 0 to 600 GHz, the designed EBEX 150 GHz, 250 GHz and 410 GHz bands. We use the best fit AHWP parameters at cryogenic temperature to calculate the values listed here. The parameters are listed in Table 4.4.

incoming polarization frequency for this given set of parameters.

Specifically, the band is defined as transmission fraction as a function of frequency $T(\nu)$. When $T(\nu) = 1$ all light at frequency ν can pass through the instrument while $T(\nu) = 0$ means no light at frequency ν can pass through. A typical ideal band shape is the 'top-hat' band shape which means $T(\nu) = 1$ within the band frequency range and outside the frequency range $T(\nu) = 0$. Table 4.5 shows the band averaged IVA phase offset $\langle\phi\rangle$ for several different top-hat bands, including a broad band from 0 GHz to 600 GHz and the designed EBEX 150 GHz, 250 GHz and 410 GHz bands. The difference between the band averaged IVA phase offsets can be as large as 7.34° which translates to a 14.68° differential rotation of the incoming polarization.

For any band shape the band-center ν_c and band-width $\Delta\nu$ can be defined. For the

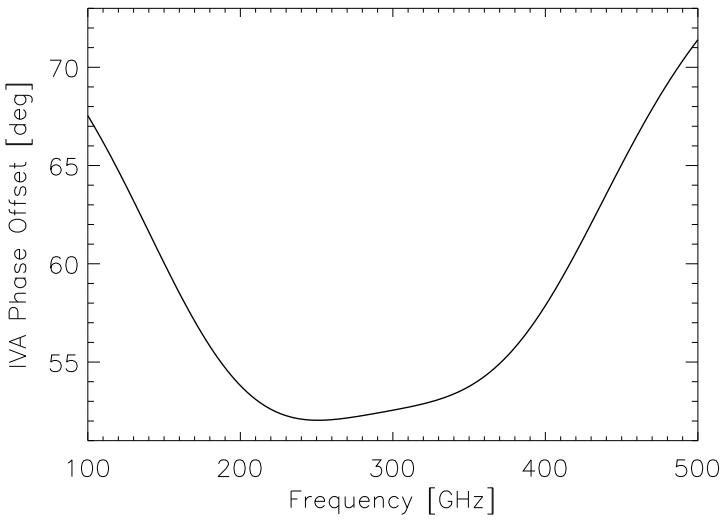

Figure 4.12: IVA phase offset vs frequency curve for the best fit EBEX AHWP parameters at cryogenic temperature and simulation parameters listed in Table 4.4.

band-center,

$$\nu_c \;=\; \frac{\int \nu\, T(\nu)\; d\nu}{\int T(\nu)\; d\nu}, \tag{4.27}$$

which is the mean frequency weighed by the transmission. For the band-width, we use the definition from Runyan *et al.*, 2002 [51]. First we define the lower and upper band edges as

$$\nu_U \;=\; \frac{\int_{\nu_c}^{\infty} \nu T'(\nu) d\nu}{\int_{\nu_c}^{\infty} T'(\nu) d\nu}\;,\; \nu_L \;=\; \frac{\int_{0}^{\nu_c} \nu T'(\nu) d\nu}{\int_{0}^{\nu_c} T'(\nu) d\nu}, \tag{4.28}$$

where $W'(\nu)$ is the derivative of the band transmission function $T(\nu)$. This definition favors frequencies where sharp transitions happen in the band curve. The band-width can then be calculated as the difference between the two

$$\Delta\nu \;=\; \nu_U - \nu_L. \tag{4.29}$$

For a top-hat band shape, the lower and upper edges are the frequencies where the transmission curve turned on and off and the band-center ν_c is $\frac{\nu_L+\nu_U}{2}$.

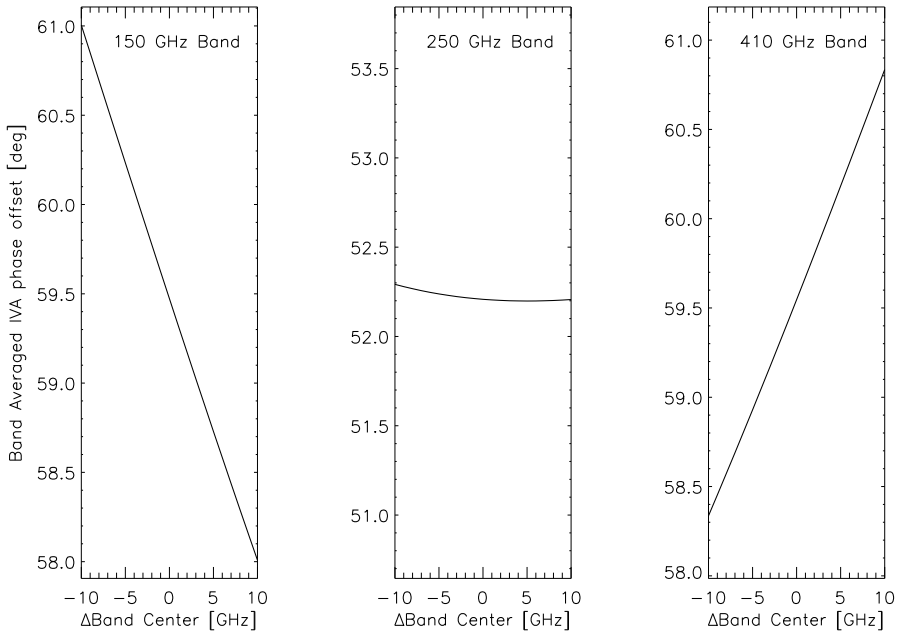

Figure 4.13: EBEX band averaged IVA phase offsets as a function of band shift while the corresponding band-widths are fixed at the designed values. From left to right: 150 GHz band, 250 GHz band and 410 GHz band. Here we use the best fit AHWP parameters at cryogenic temperature in the simulation. The parameters are listed in Table 4.4. The band averaged IVA phase offset is changed by 0.15°/GHz, 0.005°/GHz and 0.12°/GHz for a shift in 150 GHz, 250 GHz and 410 GHz band, respectively.

Shifting the band and changing the width of the band are two ways to change the shape of a top-hat band. Such changes affect the band averaged IVA phase offset. Fig. 4.13 and Fig. 4.14 show how $\langle\phi\rangle$ varies with a band shift or a change of band-width for the three designed EBEX frequency bands. A band shift changes the band averaged IVA phase offset by 0.15°/GHz for 150 GHz band and 0.12°/GHz for 410 GHz band. Since the 250 GHz band resides at the flat part of the IVA phase offset vs frequency curve, the effect of band shift on band averaged IVA phase shift is 0.005°/GHz, more than an order of magnitude smaller than that in the 150 GHz and 410 GHz bands. A change in band-width has less than 0.006°/GHz effect on the band averaged IVA phase shift in all three frequency bands.

In practice, the measured observation bands have more complicated structure than a

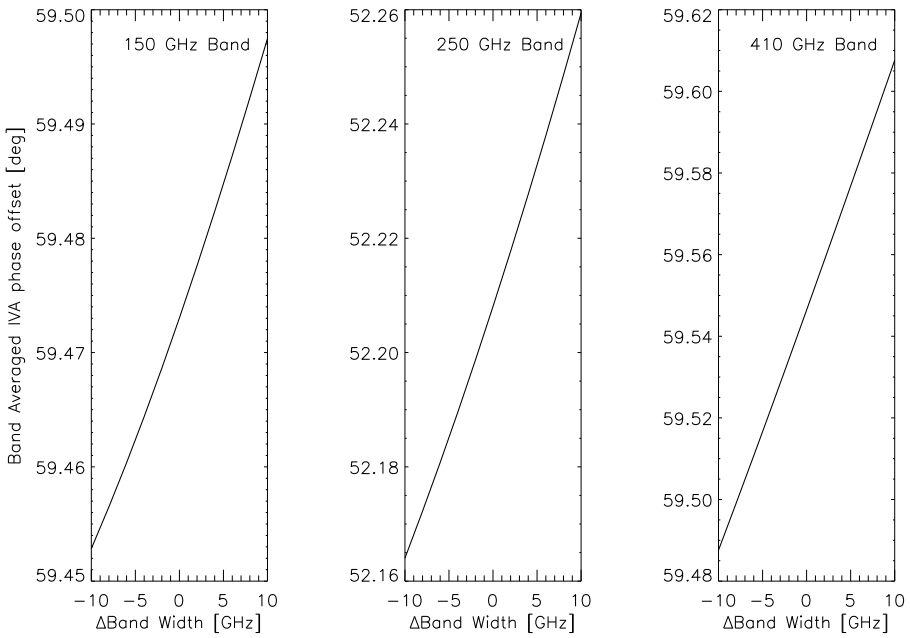

Figure 4.14: EBEX band averaged IVA phase offsets as a function of change in bandwidth while the corresponding band-centers are fixed at the designed values. From left to right: 150 GHz band, 250 GHz band and 410 GHz band. Here we use the best fit AHWP parameters at cryogenic temperature in the simulation. The parameters are listed in Table 4.4. The band averaged IVA phase offset is changed by 0.006°/GHz for a change of band-width in all three frequency bands.

Band (GHz)	ν_c (GHz)	$\Delta\nu$ (GHz)	$\langle\phi\rangle$
150	151.6 ± 1.1	25.1 ± 1.4	$59.50^\circ \pm 0.11^\circ$
250	244.0 ± 0.9	27.5 ± 1.1	$52.21^\circ \pm 0.01^\circ$
410	393.9 ± 1.7	45.4 ± 2.1	$58.21^\circ \pm 0.12^\circ$

Table 4.6: Band parameters for the measured EBEX bands in LDB flight configuration. The calculations of the top-hat equivalent band-centers, band-widths and their uncertainties are presented in K. Zilic's thesis [34]. Band averaged IVA phase offsets $\langle\phi\rangle$ and their uncertainties are calculated using Monte-Carlo simulation given the uncertainties of the band data points.

top-hat shape. In Fig. 4.15 we show the measured EBEX 150 GHz, 250 GHz and 410 GHz bands in the EBEX long-duration balloon flight configuration. The detailed analysis to derive these bands from the measurements is presented in the thesis of former Cosmolab member K. Zilic [34]. Table 4.6 lists the equivalent top-hat band-centers and band-widths derived from the measurements for all three EBEX bands. Given the error bars of the data points, Zilic used Monte-Carlo simulation to calculate the uncertainties of the band parameters, which are also listed in Table 4.6.

Given the measured EBEX bands, we calculate the band averaged IVA phase offsets using the mean values. To assess the uncertainties of $\langle\phi\rangle$, we run 500 Monte-Carlo simulations for each of the three frequency channels. In each simulation, we generate a random realization of the transmission at each frequency given the corresponding error bar. The band averaged IVA phase offset is then calculated for each simulation. We use the standard deviation from the 500 simulations as the uncertainty of $\langle\phi\rangle$ for each band. The mean and uncertainty of the band averaged IVA phase offset angles for the EBEX bands are listed in Table 4.6. The uncertainties on the band averaged IVA phase offset $\langle\phi\rangle$ are 0.11°, 0.01° and 0.12° for the 150 GHz, 250 GHz and 410 GHz bands, respectively. The uncertainty for the 250 GHz band is an order of magnitude smaller because the IVA phase offset vs frequency curve is flat within the frequency range of the band.

During the EBEX 2012 Palestine integration campaign, the instrument had a different filter in the system compared to the flight configuration which resulted in slightly different band shapes. We include the analysis of the the band averaged AHWP phase offset of these bands in Appendix A in case the result is needed for some of the ground calibration

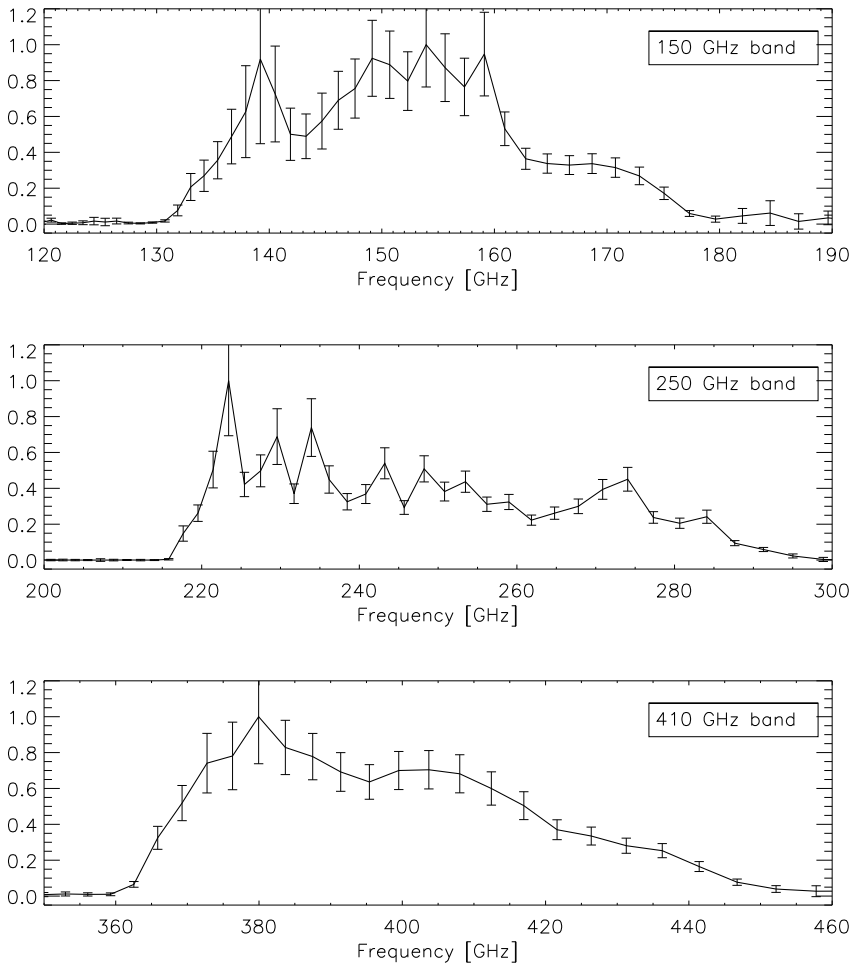

Figure 4.15: Measured EBEX 150 GHz, 250 GHz and 410 GHz bands in the LDB flight configuration. The measurements and data analysis to derive these bands are presented in K. Zilic's thesis [34].

Ordinary index of refraction [42]	$n_o(\nu) = 3.053 + 4.7 \times 10^{-6}\nu$ $+2.2 \times 10^{-10}\nu^2 + 1.1 \times 10^{-12}\nu^3$
Extraordinary index of refraction [42]	$n_e = 3.387 + 1.3 \times 10^{-5}\nu$
Thickness of HWPs in the stack	$\vec{d} = [1.665, 1.677, 1.648, 1.675, 1.64]mm$
Relative orientation of the stack	$\vec{\theta} = (0°, 26.5°, 94.8°, 28.1°, -2.6°)$
Resolution of AHWP angle	$\Delta\rho = 0.1°$
Resolution of frequency	$\Delta f = 1.0\ GHz$

Table 4.7: Best fit parameters of EBEX five-stack sapphire AHWP at room temperature and other parameters used in the IVA phase offset simulations in Sec. 4.2.5.

tests.

4.2.5 Incoming signal spectrum

In this section, we assess the effect of the incoming signal spectrum when it is not flat across the frequencies. Here we use the best fit EBEX AHWP parameters and the frequency dependent indices of refraction of sapphire at room temperature in the simulation as an example, because the results are used in EBEX ground polarization calibration data analysis [35]. The AHWP parameters are listed in Table 4.7. Fig. 4.16 shows the IVA phase offset angle as a function of frequency for this set of parameters. The polarization angle α_{in} is set to 0° at all frequencies in the simulations here.

When the spectrum of incident signal is considered, the incoming Stokes vector $\vec{S}_{in}$ for linearly polarized light at any frequency ν can be written as

$$\vec{S}_{in}(\nu) = I_{in}(\nu)(1, p\ cos2\alpha_{in}, p\ sin2\alpha_{in}, 0), \tag{4.30}$$

where $I_{in}(\nu)$ is the incoming signal spectrum. In the analysis and simulation performed here, we assume that the polarization fraction p and the incoming polarization angle α_{in} are independent of frequency.

In this section, we use the following spectra in the simulation: CMB anisotropy spectrum, galactic polarized thermal dust spectrum, black body source spectra at 77 K (liquid

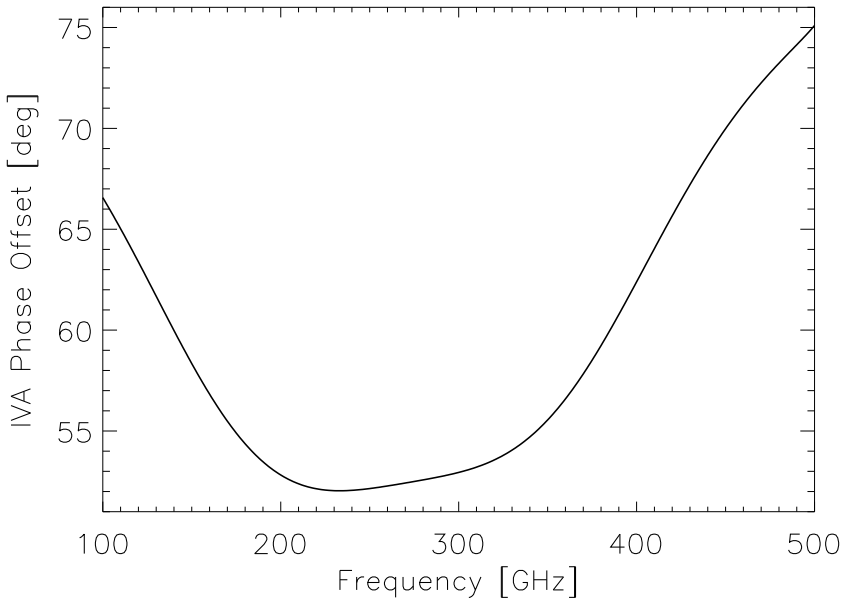

Figure 4.16: IVA phase offset vs frequency curve using the best fit EBEX AHWP parameters at room temperature and simulation parameters listed in Table 4.7.

nitrogen temperature), 300 K (room temperature) and 2000 K (black body source used in spectroscopic measurement of the AHWP at Cardiff University). First we consider the situations with only one incoming source spectrum. In these situations, the spectral shape (i.e. frequency scaling of signal) rather than the absolute level of the spectrum affects the result of the band averaged IVA phase offset. At the end of this section, we briefly discuss cases with more than one incoming source.

The spectrum of a black body with temperature T is

$$B(\nu, T) = \frac{2h\nu^3}{c^2} \frac{1}{e^{\frac{h\nu}{k_B T}} - 1}. \tag{4.31}$$

The CMB is a 2.725 K black body. The spectrum of the CMB anisotropy, which is the signal measured by EBEX, is the derivative of the black body spectrum, particularly

$$I_{CMB}(\nu) = \frac{dB(\nu, T_{CMB})}{dT} \Delta T = \frac{2h^2\nu^4 e^{\frac{h\nu}{kT_{CMB}}}}{c^2 k T_{CMB}^2 (e^{\frac{h\nu}{kT_{CMB}}} - 1)^2} \Delta T. \tag{4.32}$$

Galactic polarized thermal dust is modeled as a black body with temperature T_d and a power law emissivity with spectral index β,

$$I_{dust}(\nu) = C\nu^{\beta} B(\nu, T_d). \tag{4.33}$$

Here C is a scaling constant that determines the absolute amplitude of the dust signal. In correspondence with the recent all sky measurements [52], we set the spectral index $\beta = 1.59$ and the dust temperature $T_d = 19.6K$ here.

To study the effect of the incoming signal spectrum alone, we assume the bands have a top-hat shape. Specifically, the three designed EBEX bands and a broad band between 0 GHz to 600 GHz are used. In Table 4.8 we list the band averaged IVA phase offsets for each of the five incident spectra given these top-hat bands. We also list the results for a flat input spectrum as reference. As seen in Table 4.8, the band averaged IVA phase offset $\langle\phi\rangle$ for the three black body sources are similar. This is because the EBEX frequency range falls in the Rayleigh-Jeans tail of the these black body spectra and thus their spectral shapes in this frequency range are similar. For EBEX bands, the difference between CMB

Top-hat Bands	[133,173] GHz	[217,288] GHz	[366,450] GHz	[0,600] GHz
CMB Anisotropy	57.84°	52.25°	62.80°	56.81°
Dust	57.51°	52.31°	64.19°	64.67°
77K source	57.70°	52.29°	63.93°	62.38°
300K source	57.69°	52.29°	63.95°	62.58°
2000K source	57.69°	52.29°	63.96°	62.63°
Flat spectrum	57.97°	52.26°	63.51°	59.95°

Table 4.8: The band averaged IVA phase offset for different incoming signal spectra in the designed EBEX 150 GHz, 250 GHz and 410 GHz bands and a broad band from 0 GHz to 600 GHz. All bands are assumed to have a top-hat shape. The band edges of these bands are also listed here. Here we use the best fit AHWP parameters at room temperature in the simulation. The parameters are listed in Table 4.7

and dust IVA offset angles can be as big as 1.39° (in 410 GHz band), which translates to a 2.78° difference in rotation of the polarization angle α.

For CMB polarization experiments, there are typically more than one incident radiation. Over the entire sky, polarized galactic thermal dust emission is a dominant contamination source [27]. When both CMB and dust signal are present, the calculation of the band averaged IVA phase offset $\langle\phi\rangle$ have to include not only the spectral shape of the two signal components, but also the relative amplitude between the two signals. The spectral shape of the dust and the amplitudes of CMB and dust signals, however, need to be determined from the measurements. But during the analysis process to separate the CMB and dust signal in the observation, the IVA phase offset angles for CMB and dust are needed. These dependencies pose challenges to the data analysis for CMB polarization experiments utilizing an AHWP. I will address my work on dust foreground cleaning in the presence of an AHWP in Chapter 5 and Chapter 6.

4.2.6 Combined effect from bands and incident spectra

In Sec. 4.2.4 and Sec. 4.2.5 the effect of observation band and incoming signal spectrum are considered separately. In practice, these two effects are present simultaneously. In Table 4.9 we list the band averaged IVA phase offsets $\langle\phi\rangle$ and their uncertainties for different incoming signal spectra for the three measured EBEX bands in the 2012 LDB

EBEX LDB bands	150 GHz	250 GHz	410 GHz
CMB Anisotropy	$59.38^\circ \pm 0.10^\circ$	$52.21^\circ \pm 0.01^\circ$	$57.81^\circ \pm 0.11^\circ$
Galactic Dust	$59.06^\circ \pm 0.08^\circ$	$52.20^\circ \pm 0.01^\circ$	$58.63^\circ \pm 0.11^\circ$
77K source	$59.25^\circ \pm 0.09^\circ$	$52.20^\circ \pm 0.01^\circ$	$58.47^\circ \pm 0.11^\circ$
300K source	$59.25^\circ \pm 0.08^\circ$	$52.20^\circ \pm 0.01^\circ$	$58.49^\circ \pm 0.11^\circ$
2000K source	$59.24^\circ \pm 0.09^\circ$	$52.20^\circ \pm 0.01^\circ$	$58.49^\circ \pm 0.13^\circ$

Table 4.9: The band averaged IVA phase offset for different incoming signal spectra given the measured EBEX LDB flight bands. The uncertainties are calculated using Monte-Carlo simulation with the procedure listed in Sec. 4.2.4. Here we use the best fit AHWP parameters at cryogenic temperature in the simulation, which are listed in Table 4.4.

flight configuration (the bands are shown in Fig. 4.15). We include CMB anisotropy, galactic dust, 77 K black body, 300 K black body and 2000 K black body in the list of incident spectra. In the simulation we use the best fit AHWP parameters and frequency dependent indices of refraction of sapphire at cryogenic temperature, which are listed in Table 4.4. The procedure to calculate the uncertainty of $\langle\phi\rangle$ using Monte-Carlo simulation is described in Sec. 4.2.4.

4.2.7 Comparison with other predictive model

Given the parameters of the AHWP, the polarimetry can be modeled by either Mueller matrices or Jones matrices. Although Jones matrices can not treat partially polarized light, for the purpose of calculating the IVA phase angle, Jones matrices can be used with fully polarized light. EBEX collaborator G. Savini performed a Jones Matrix calculation using the best fit EBEX AHWP parameters with the procedures outlined in Savini *et al.*, 2006 [42]. In the calculation, electromagnetic field of the light is calculated as it propagates through the birefringent material. In contrary to the Mueller matrix calculation performed in this chapter, the absorption of the AHWP and multiple reflection between each plates are included in the calculation. Fig. 4.17 shows the comparison between the two models utilizing Mueller matrices or Jones matrices. The ϕ vs ν curves produced by the two predictive models agree on both general shape and absolute values.

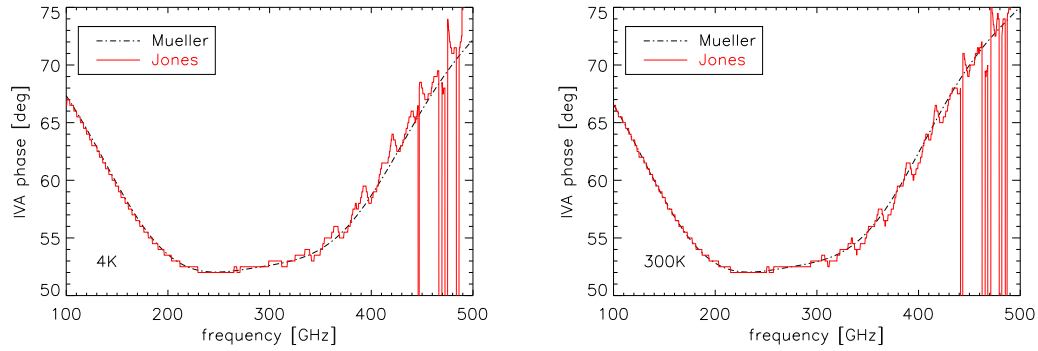

Figure 4.17: Comparison between ϕ vs ν curve calculated from different predictive models. Dot-dash: result from Mueller matrix calculation done in this chapter. Solid: result from Jones matrix calculation performed by EBEX collaborator G. Savini. Left: comparison of simulations for the EBEX AHWP operated at cryogenic temperature. Right: comparison of simulations for the EBEX AHWP operated at room temperature. Best fit thicknesses of the plates $\vec{d}$, best fit relative orientation angle between the plates $\vec{\theta}$ and constant indices of refraction n_o and n_e at corresponding temperature are used in all calculations.

4.2.8 Comparison with experimental data

To test the validity of the models, we compare the simulation results to two different sets of experimental data. The first data set is collected by EBEX collaborators W. Grainger, L. Spencer and L. Moncelsi at Cardiff University using Fourier Transform Spectroscopy (FTS). The experiment set up includes a polarized Martin Puplett FTS (pFTS), a collimating lens, a linear polarizer set to be horizontal, the EBEX AHWP, a second linear polarizer, a focusing lens and the detector. The second linear polarizer is set to align with the first linear polarizer. The transmission as a function of frequency is measured for AHWP angles at 5° intervals from -5° to 95°, and then at 130°, 135°, 140°, 175°, 180°, 185°, 265°, 270°, 275° and 360°. At each frequency, the IVA curve is fitted to compute the phase angle $\phi(\nu)$. The methodology is described in detail in Moncelsi *et al.*, 2014 [43]. A mark was made on the AHWP as a reference point so that the AHWP always returned in the same orientation during the measurement. The mark was determined by finding the orientation of the AHWP with the maximum white light fringe value over a band from 0-600 GHz. Since we do not know the exact band shape and source spectrum used when setting the

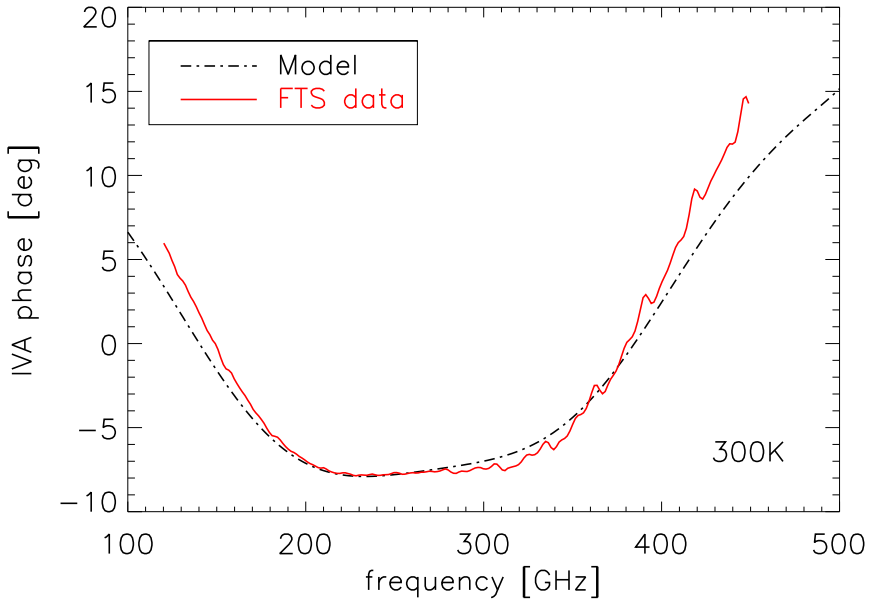

Figure 4.18: The comparison between ϕ vs ν curves from simulations using Mueller matrix formalism and measurements performed at Cardiff University by EBEX collaborators. Since the meaning of the absolute angle in this measurement is not exactly known (more discussed in the text), only the shape the two curves are compared. The simulated curve is arbitrarily shifted down by 59.94° to align the bottom flat part of the two curves.

mark, we can not interpret the meaning of the mark accurately. We only use this data set as a relative measurement to compare the shape of the ϕ vs ν curve. The EBEX AHWP was operated at room temperature in this measurement so we use the simulation with the best fit AHWP parameters and the frequency dependent indices of refraction at room temperature. The AHWP parameters are listed in Table 4.7. Fig. 4.18 shows the comparison of the ϕ vs ν curves between our simulation and the measurement. The simulated curve is arbitrarily shifted down by 59.94° to align the bottom flat part of the two curves. With the bottom flat part aligned, the measured data has steeper slopes within the frequency range $\nu < 200\ GHz$ and $\nu > 350\ GHz$. This discrepancy would induce uncertainty in the band integrated IVA phase offset.

The second data set is collected by former Cosmolab member J. Klein during the EBEX

2012 Palestine integration campaign. The description of the experimental set up and analysis is provided in detail in Klein's thesis [35]. The measurement is an end-to-end absolute calibration of the polarization angle for EBEX AHWP polarimetry. During the measurement the AHWP was operated at cryogenic temperature, so we use the best fit AHWP parameters at cryogenic temperature in the simulation. The AHWP parameters used in the simulation are listed in Table 4.4. Fig. 4.19 shows the comparison of detected polarization angle vs frequency curves between the measured data and model. In order to directly compare the model to the experimental data, the simulated curve is multiplied by -2 and then shifted by a value related to various geometry of the instrument. The detailed list of the angle transformations is provided in Klein's thesis [35]. One of the angle transformations is based on the relative orientation between the mark on the AHWP produced in the spectroscopic measurement and the optical axis of the AHWP. We calculated this angle shift using the band averaged IVA phase offset based on our simulation assuming flat band shape, 2000 K black body source spectrum , best fit AHWP parameters and frequency dependent indices of refraction of sapphire at room temperature. As we see in Fig. 4.19 the predicted curve is off by $\sim 4^\circ$ compared to the absolute calibration data. One possible source of this discrepancy is the difference between our simulated IVA phase offset angle vs frequency curve and the one from fitting the spectroscopic data (Fig. 4.18). The exact cause of the discrepancy between our model and calibration data still need to be sorted out.

4.2.9 Discussion

For all the simulations in this chapter, we assume perfect knowledge of the parameters of an ideal AHWP. In practice, however, the AHWP is not ideal and the parameters are measured with some uncertainty. For CMB experiments targeting the polarization signal, end to end polarization calibration is performed on known polarized source both on the ground and in flight. The calibration measurement always have uncertainty. For data analysis processes which rely on the AHWP rotation effect as an input, such as foreground cleaning, being able to tolerate the uncertainty of the AHWP induced rotation angle is essential. I will address this topic in more detail in Chapter 5 and Chapter 6.

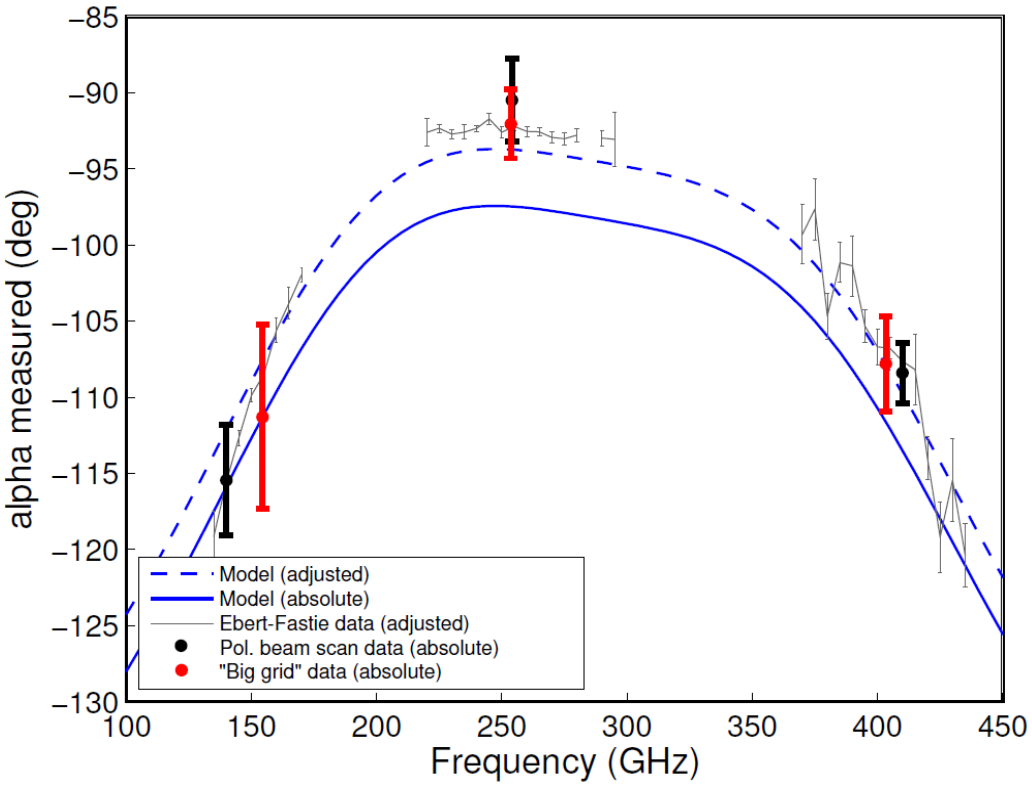

Figure 4.19: Comparison of polarization calibration angle as a function of frequency between the simulation described in this chapter and the polarization calibration measurement performed in EBEX 2012 Palestine integration campaign. The AHWP parameters in the simulation are listed in Table 4.4. The simulated curve needs to be shifted by $\sim 4^\circ$ to fit the calibration data.

Chapter 5

Simple Foreground Cleaning Method in the Presence of an Achromatic Half-Wave Plate

In Chapter 4 we discuss the AHWP frequency dependent rotation effect. When both CMB and galactic dust signals are present, the amount of rotation can be calculated and corrected with knowledge of the AHWP parameters, the spectrum and relative polarization intensity between the two signals. In reality, however, while the spectrum of the CMB component is well known, that of dust is not. The polarized intensities of dust and CMB are also not well known. These uncertainties may pose challenges in the extraction of the inflationary B-mode signal.

In this chapter, I will present my work on assessing the frequency dependent rotation effect of the AHWP in the context of removing the polarized galactic dust foreground contamination. The work has been published in Bao *et al.*, 2012 [44] and the majority of this chapter follows this paper. For concreteness in the simulation we adopt the AHWP model, frequency bands and approximate noise information that are applicable to EBEX [39].

In Sec. 5.1 we describe the basic components of the simulation. Sec. 5.2 focuses on quantifying the effect of rotation due to the AHWP in the 150 GHz band. In Sec. 5.3 we use multiple frequency information to account for rotation due to Galactic dust. In Sec. 5.4,

we study the additional effects of uncertainties in the spectral response of the instrument, and in Sec. 5.5 we make concluding remarks.

5.1 Description of the Simulation

We simulate input Stokes Q and U signals due to the CMB and Galactic dust emission on a $10^\circ \times 10^\circ$ area of the sky centered on $(l, b) = (252^\circ, -52^\circ)$ in Galactic coordinates which is close to the center of the area targeted by EBEX. The maps are smoothed with an $8'$ FWHM Gaussian beam then projected to a flat sky and pixelized with a square $6.9'$ pixel. Same simulations with a $20^\circ \times 20^\circ$ patch in the same region validate that conclusions presented in this paper do not depend on patch size. The input CMB polarization angular power spectra, including both the primordial and lensing signal, are generated with CAMB [53] using the best fit WMAP 7-year cosmological parameters [54] and $r = 0.05$, unless otherwise indicated. Our polarized foreground simulation follows the prescription detailed in Stivoli *et al.*, 2010 [55] and is briefly reviewed here. The dust intensity and its frequency scaling are given by 'model 8' of Finkebeiner *et al.*, 1999 [31]. The dust polarization fraction is modeled for cases of 2%, 5%, and 10%. A polarization fraction higher than 10% would exceed the limit based on WMAP observations at intermediate and high Galactic latitudes [29, 28]. Both the dust polarization fraction and the frequency scaling are assumed to be uniform over the simulated sky area. Observations suggest that this is a good approximation [56, 31]. The pattern of the polarization angles on large angular scales ($l \lesssim 100$) is given by the WMAP dust polarization template [29]. On smaller angular scales ($l \gtrsim 100$) we add a Gaussian fluctuation power adopting a recipe first presented by Giardino *et al.*, 2002 [57]. Fig. 5.1 shows the power spectra of the CMB and of Galactic dust. For a level of 5% fractional polarization the expected level of Galactic dust is comparable to the B-mode signal at $\ell = 90$.

To simulate the operation of the AHWP we use the Mueller matrix formalism as described by Matsumura *et al.*, 2009 [41]. The level of input polarized signal is calculated for each map pixel in 50 frequency bins for each of the experiment's three top-hat bands (see Table 5.1). For each map pixel the detected intensity as a function of AHWP angle, which we call intensity vs. angle (IVA), is calculated for each frequency bin with an angular resolution of 0.05° and the total per-band IVA is the average of the 50 IVAs. The detected

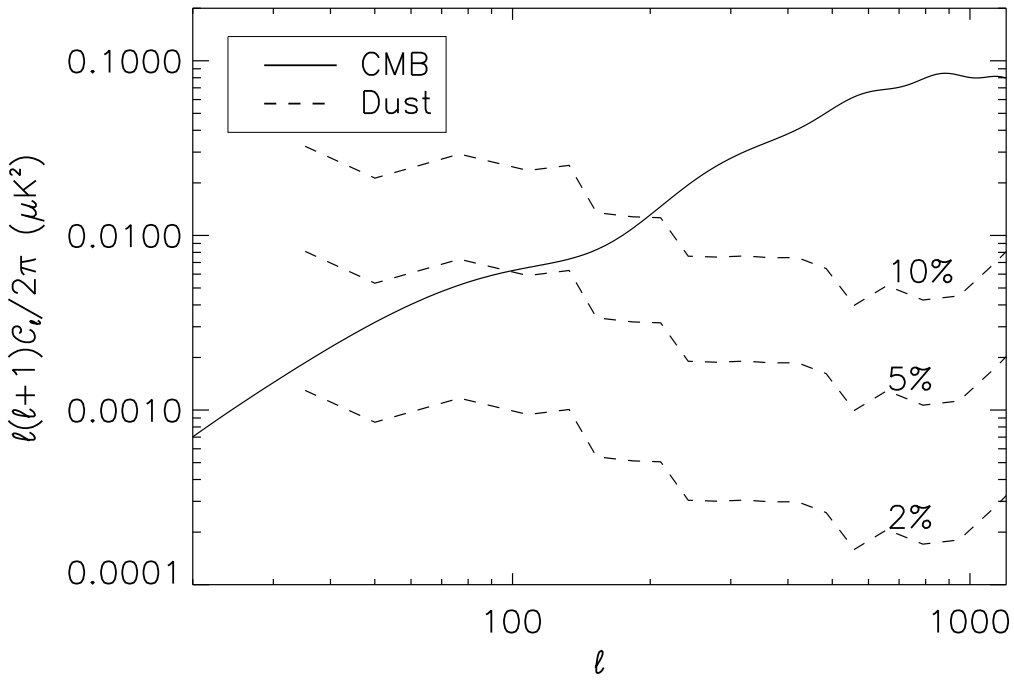

Figure 5.1: CMB (solid) and Galactic dust (dashed) B-mode power spectra at 150 GHz. The spectra from dust are for the specific area of sky simulated in this work and are given for three fractional polarization cases of 2, 5, and 10 %.

polarization angle, which is rotated relative to the input polarization angle, is encoded by the phase of the band-averaged IVA. To obtain the rotated map observed by the detector, we multiply each pixel of the input maps by a rotation matrix with the calculated phase of the band-averaged IVA. The frequency and IVA angular resolution are chosen to optimize computation time while giving negligible bias in the results. The construction parameters of the AHWP are given in Table 5.1.

Indices of refraction of AHWP	$n_o = 3.047$, $n_e = 3.364$
Thickness of each wave plate	1.69 mm
150 GHz band	133 - 173 GHz
250 GHz band	217 - 288 GHz
410 GHz band	366 - 450 GHz
Band shape	top-hat
Orientation angles of 5-stack AHWP	(0°, 25°, 88.5°, 25°, 0°)

Table 5.1: AHWP and band parameters used in the simulations.

We calculate both EE and BB power spectra simultaneously using the flat-sky approximation [58]. Each simulation is run 100 times with different CMB and noise realization, unless otherwise noted. In this study we focus on the BB power spectra. The result quoted for a given ℓ bin is the mean of the 100 simulations and the error bar is the standard deviation. Fig. 5.2 shows a validation of the process of generating CMB Q and U maps and estimating the underlying E and B-mode power spectra. No rotation due to the AHWP has been included in this validation.

For simulations that include the effects of instrumental noise we assume it is homogeneous and has a white spectrum, and add its realization to the signal to make a combined input map. In our simulation we use an instrumental noise per pixel of 1, 2.8, and 25 $\mu\mathrm{K}_{\mathrm{CMB}}$ for the 150, 250, and 410 GHz bands, respectively. Fig. 5.2 shows a validation of the noise generation and estimation process.

5.2 The Effect of Galactic Dust

If the shape of the frequency band is known then the rotation induced on the CMB signal alone can be calculated and compensated exactly because the spectrum of the CMB is

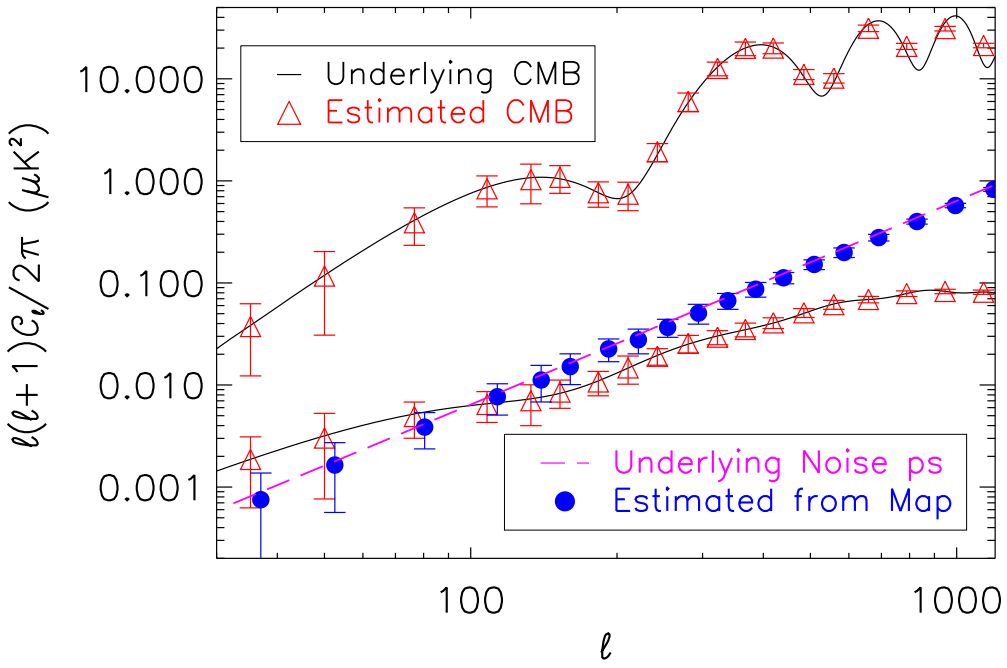

Figure 5.2: Validation of signal and noise power spectrum estimation. We generate 100 Q and U maps using an underlying power spectra (black solid curves) and use a flat-sky approximation to estimate the power spectra (red triangles with error bars). The size of error bars agrees with predictions for the contributions of cosmic and sample variance. We also make 100 noise only Q and U realizations using white noise with RMS of 1 μK (magenta dashed line) and estimate the power spectrum (blue solid circles with error bars). The estimated noise power spectrum is shown slightly offset in ℓ to enhance clarity.

known. This rotation is uniform across the sky and with the parameters given in Table 5.1 is 55° in the 150 GHz band. The presence of Galactic dust modifies the intensity and angle of the net incident polarization and thus the amount of rotation induced by the AHWP. The spectral dependence and spatial distribution of Galactic dust polarization is not precisely known and therefore the amount of rotation it induces can only be estimated. How big is this extra rotation? Can it simply be ignored because it is negligible? In the remainder of this section we assess these questions for the 150 GHz band.

These first simulations include CMB and dust, without instrumental noise. We calculate rotated Q and U maps resulting from passing the total (CMB+dust) incoming polarization through the AHWP. We then 'de-rotate' the maps by the calculated rotation angle for CMB only, simulating ignorance of the effects of the dust foreground on the rotation. We subtract the input dust Q and U maps from the de-rotated map to acknowledge the presence of the effects of dust *polarized intensity* on the total Q and U maps. Note however that the effect of *rotation due to dust polarization*, which is a consequence of the AHWP, is left in the map. We then calculate the angular power spectrum of the resulting maps for 2%, 5%, and 10% of dust polarization (see Fig. 5.3). For the fiducial value of $r = 0.05$ ignoring the effect of rotation introduces noticeable bias in the estimation of the CMB power spectrum for 10% dust polarization but not for 2% dust polarization. For 5% dust polarization bias is only noticeable at the lowest ℓ bin.

5.3 Removing AHWP Induced Rotation in Dust Subtraction

In the previous section we showed that for levels of polarized dust of more than 5% the effect of the rotation due to dust in the AHWP cannot be ignored. In this section we employ a simple form of dust subtraction in an attempt to correct for the rotation. In this approach we make two initial assumptions in order to extract the dust frequency scaling information:

1. the signal at the 150 GHz band is dominated by the CMB and dust can be neglected;

2. the signal at the 410 GHz band comes entirely from dust and CMB can be neglected;

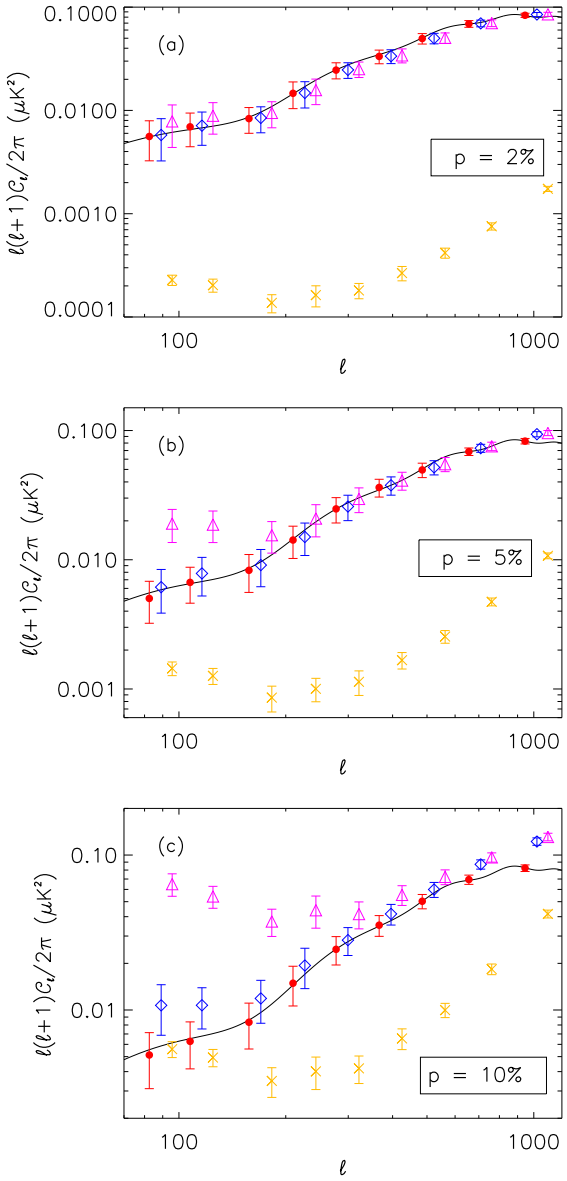

Figure 5.3: Effect of rotation due to 2%, 5%, and 10% polarized dust on the estimation of the B-mode power spectrum. The input CMB power spectrum (red solid circles) follows the underlying assumed power spectrum (black solid line). The difference between the input CMB and the power spectrum of the map after de-rotation by the rotation angle corresponding to the CMB alone (magenta triangles) indicates the effect of polarized dust. After subtracting the dust intensity, only the *rotation* due to the presence of dust remains (blue diamonds). The power spectrum of a map of the difference between the input map and the de-rotated, dust-subtracted map (yellow crosses) quantifies the effect of the rotation due to dust alone. Power spectra points are all calculated at the same ℓ bins but are shown slightly offset in ℓ to enhance clarity.

We prepare the total (CMB+dust) rotated polarization maps in 150, 250, and 410 GHz bands and add noise in the map domain. We then calculate the polarization intensity maps and the signal RMS in all three bands assuming that the noise RMS is exactly known. Following assumption 1 the map RMS of CMB at 150 GHz is known. We extrapolate the CMB level to 250 GHz and calculate the map RMS for dust at 250 GHz. Following assumption 2 we also obtain the map RMS for dust at 410 GHz. Using the dust levels at 250 and 410 GHz we fit a grey body dust model, given by a power law multiplied by an 18 K blackbody. The power law spectral index is taken to be uniform across the entire simulated sky area. The top hat spectral response of the instrument is assumed to be precisely known (we address uncertainties in the bandpass in Section 5.4). The fitted dust model is used to calculate the level of dust at the 150 GHz band, extrapolated from the 410 GHz map, and to calculate and correct for the rotation angle at this band due to the combination of dust and CMB. We make a final map that contains an estimate of the CMB alone after corrections for both dust polarized intensity and rotation induced by the AHWP. We calculate the power spectrum of this map including subtraction of an estimate of the noise spectrum. For an estimate of the noise spectrum we use the known input RMS. As a test of the entire pipeline we run it with no dust and no noise and validate that the extracted power spectrum agrees with the input CMB power spectrum.

For each set of 100 simulations, we determine whether the final estimated CMB power spectrum is biased or not. The power spectrum is conservatively assumed biased if the mean power estimated in *any* ℓ bin is outside of the 1-σ cosmic variance error bar. We find that for the nominal noise levels, $r = 0.01$ or above, and all dust polarized fractions at or below 10% the dust subtraction procedure recovers an unbiased estimate of the B-mode power spectrum. The results for 10% dust polarization fraction are shown in Fig. 5.4.Only data points with signal to noise ratio (SNR) > 1 are plotted. For $r = 0.009$ and lower, and 10% dust polarization fraction, we find that the recovered B-mode power spectrum is biased at the lowest ℓ bin. When the dust polarization is lower the r level that can be recovered without bias is higher because the higher relative noise at 410 GHz has a larger effect on the CMB estimate at 150 GHz. For 2% dust polarization fraction, we can recover r as low as 0.02.

We also use a different approach to quantify the bias caused by the dust subtraction procedure. We run 100 simulations with an input of $r = 0$ and 10% dust polarization fraction. We fit a non-zero r to the difference between the estimated and input CMB power spectrum at the lowest ℓ bin, while keeping the shape of the primordial B mode signal. We consider this fit as the lower limit of r value we can detect using this dust subtraction method. We find a best fit with $r = 0.01$, which is close to the result we found earlier.

5.4 Uncertainty in Detection Band and High Frequency Spectral Response

So far we assumed that the spectral response of the instrument is known. Only the frequency scaling of Galactic dust is determined from the fit. Uncertainty in the spectral response leads to uncertainty in the amount of rotation induced by the AHWP. To assess the level of this effect quantitatively we assume a top-hat band shape that is characterized by two parameters, center and width. We simulate CMB and dust signals with bands that have varying widths, or varying band-centers (but not both simultaneously), and analyze the maps using the dust subtraction algorithm discussed in the previous section but assuming *nominal* band-width or center. No instrumental noise is included. All simulations have 10% polarized dust and $r = 0.05$. We search for the level of shift in band-center or change in width that leads to bias in the estimation of the final CMB spectrum. We use the same criterion for bias as described in Section 5.3.

5.4.1 Shift of Band-Center

Simulations are carried out by shifting only one band-center, keeping the other two fixed at their nominal values. We find that shifts of more than 1, 9, and 20 GHz for the 150, 250, and 410 GHz bands, respectively, lead to biased power spectra. The limit for shift of the 150 GHz band is due to mixing between E and B modes: an error in band-center leaves the CMB slightly rotated after correction for the AHWP is applied (using the nominal band) and thus a portion of the E-mode signal is mixed into the B-mode signal. This is apparent in Fig. 5.5 (panel b), which shows a 2 GHz shift for the 150 GHz; the bias is primarily at

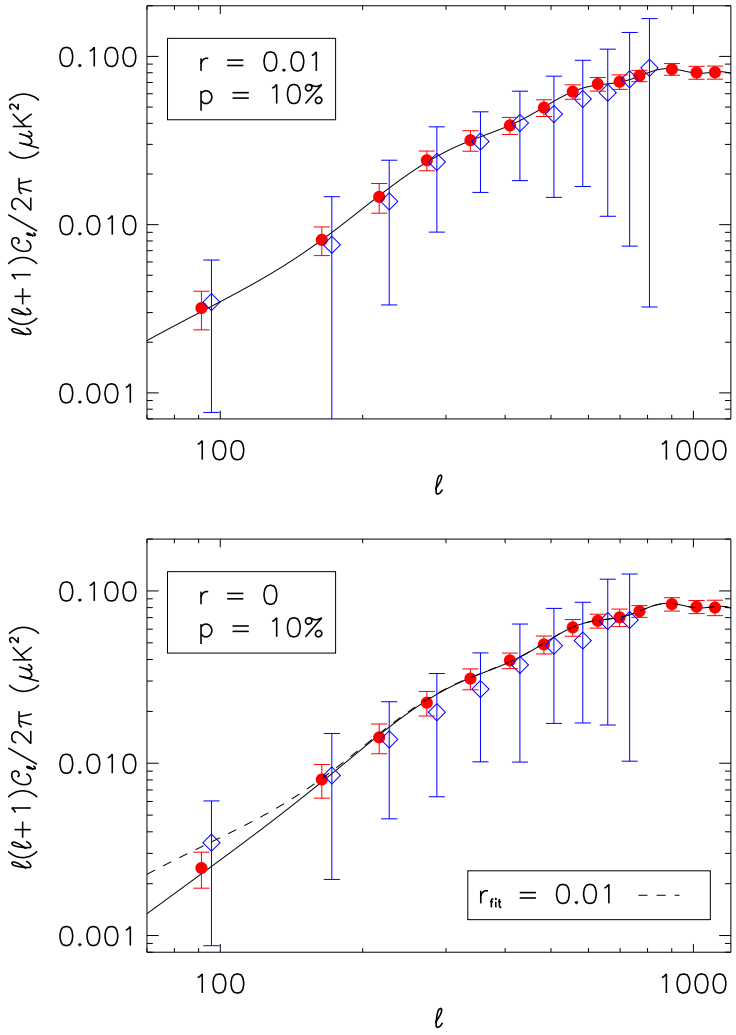

Figure 5.4: Comparison between the underlying CMB model (black line), the input CMB (red circles) and the estimate of the CMB power spectrum using a map in which the effects of both dust polarized intensity and dust induced extra rotation has been accounted for (blue diamonds). With 10% dust polarization, a crude dust subtraction algorithm (see text) can account for the rotation induced in the AHWP with an r value as low as 0.01 (top panel). The error bars quantify the effect of both instrument noise and cosmic variance. In the bottom panel the input r is zero and the underlying CMB spectrum has only a lensing signal; Galactic dust is 10% polarized. The estimated CMB spectrum has a best fit $r = 0.01$.

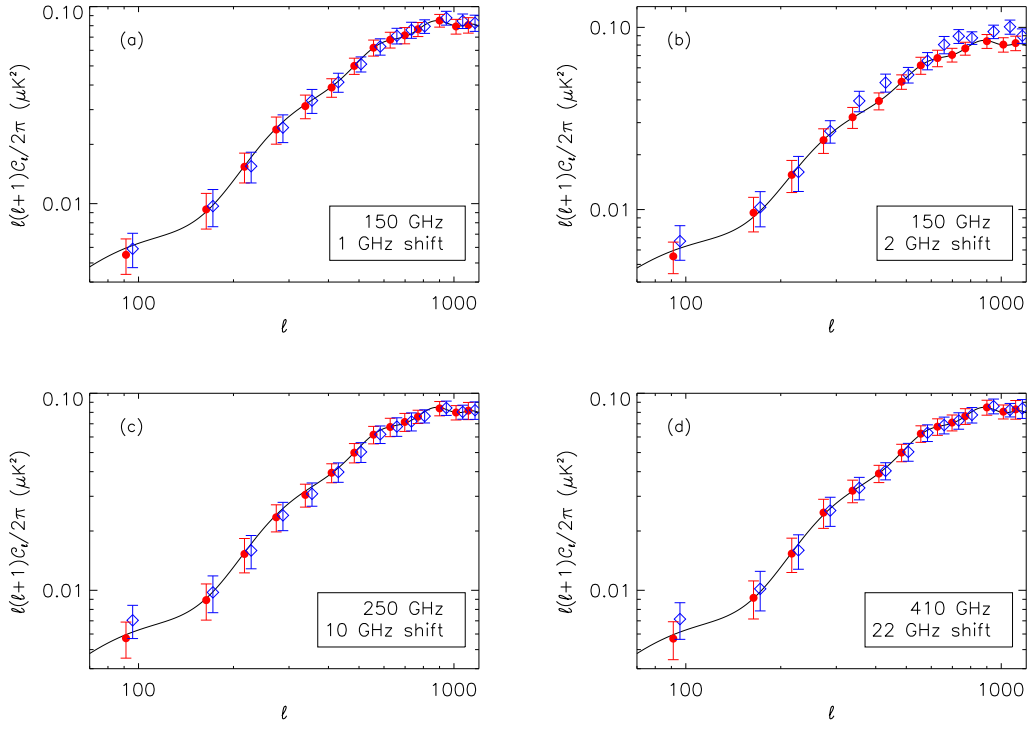

Figure 5.5: Effect of band-center shift of 1 GHz of the 150 GHz band (panel a), 2 GHz of the 150 GHz band (panel b), 10 GHz of the 250 GHz band (panel c) and 22 GHz of the 410 GHz band (panel d), respectively. In panel (b) excess power at high ℓ comes from mixing of E and B-mode. In panels (c) and (d) it comes from misestimate of the effects of dust. Figure symbols are the same as in Figure 5.4.

high ℓ. The limits on the 250 and 410 GHz bands mainly come from misestimate of rotation due to dust, but because dust is not dominant at the 150 GHz band the requirement is less stringent. Panels (c) and (d) in Fig. 5.5 show shifts of 10 and 22 GHz for the 250 and 410 GHz bands, in which bias due to dust is found only at the lowest ℓ bin.

5.4.2 Misestimate of Band-Width

Simulations are carried out by changing one band-width at a time, keeping the other two fixed at their nominal values. We find that a change of band-width by more than 0.8, 2,

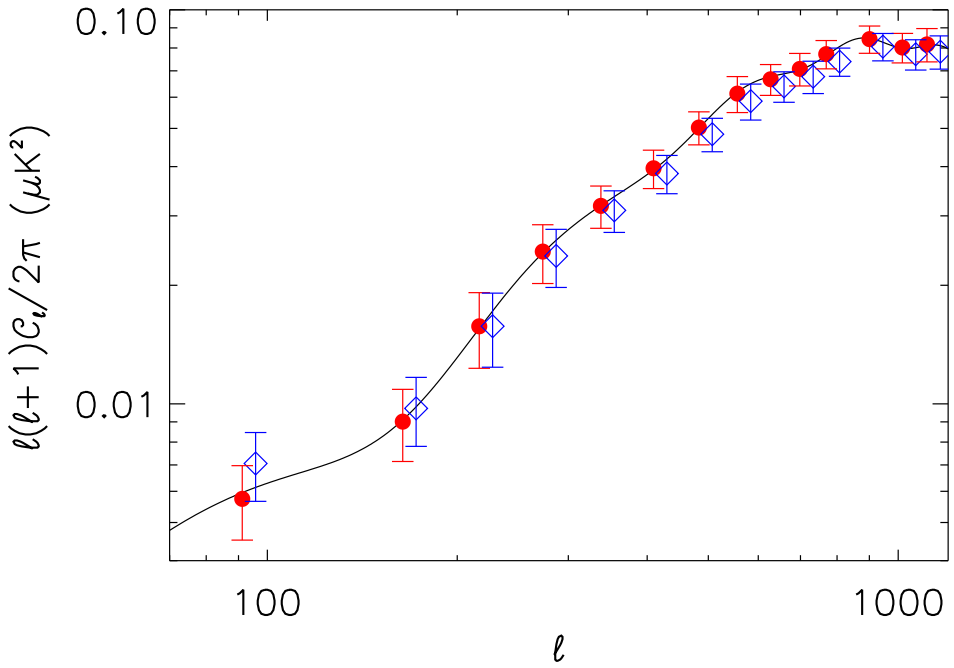

Figure 5.6: A 1 GHz increase in the band-width of the 150 GHz band relative to the width assumed leads to an underestimate of the level of dust in this band and thus to a misestimate of the rotation due to dust. This leads to excess power at low ℓ. Figure symbols are the same as in Fig. 5.4.

or 14 GHz for the 150, 250, and 410 GHz band, respectively, exceeds the criterion for no bias. The result for the 150 GHz band with a change of 1 GHz in width is shown in Figure 5.6. The cause of bias in any of the bands is a misestimate of total power detected at the particular band thus a misestimate of both the polarized dust intensity and the rotation due to dust. For this reason the bias is largest at the lowest ℓ bins.

5.4.3 Effects of High Frequency Spectral Leak

Dust intensity is rising up to ~ 2 THz. A higher than expected and unknown instrumental response at out-of-band frequencies, which is called a 'spectral leak', may bias the subtraction of the dust signal and by extension the estimate of the underlying CMB signal. We simulate two specific leaks, which are both top-hat in shape, a narrow leak between 1750 and 1850 GHz and a broad leak between 500 and 2000 GHz. For both cases the power in the leak is adjusted to be 0.1%, 1% or 1% of the in-band power for the 150, 250, and 410 GHz bands, respectively, as measured with a 300 K blackbody source. These values are readily achievable experimentally [59]. We properly include the change in the refraction indices of sapphire with frequency [47]. Maps are prepared with signals that include power in the leak, but are analyzed, including the steps of dust subtraction, assuming no knowledge of the leak. Instrumental noise is not included in the simulation. For both cases we find no biases in the estimate of the final CMB power spectrum. Figure 5.7 shows the case for the broad leak.

5.5 Discussion and Summary

The spectral response of an achromatic half-wave plate may induce biases in the estimation of polarized signals. We analyze the level of such biases as in the context of measurements of the B-mode signal of the CMB in the presence of Galactic dust, the dominant source of foreground emission in cases of interest here. We use the specific experimental configuration corresponding to the EBEX balloon-borne experiment.

For the area of sky considered we find that with reasonable assumptions about the magnitude and spectral shape of dust, the effects of rotation induced by the AHWP are only appreciable when dust is polarized at a level of about 5% and above and the tensor-to-scalar ratio r is less than ~ 0.05. In the regime when the effects of rotation are appreciable, even a crude process of dust estimation and subtraction mitigates the effects of AHWP rotation to below detectable levels. For example, using the crude dust subtraction process we find no bias in the estimation of the B-mode power spectrum for dust polarization fraction as large as 10% and r as low as 0.01. For 2% dust polarization fraction, r of 0.02 or higher is recovered without bias.

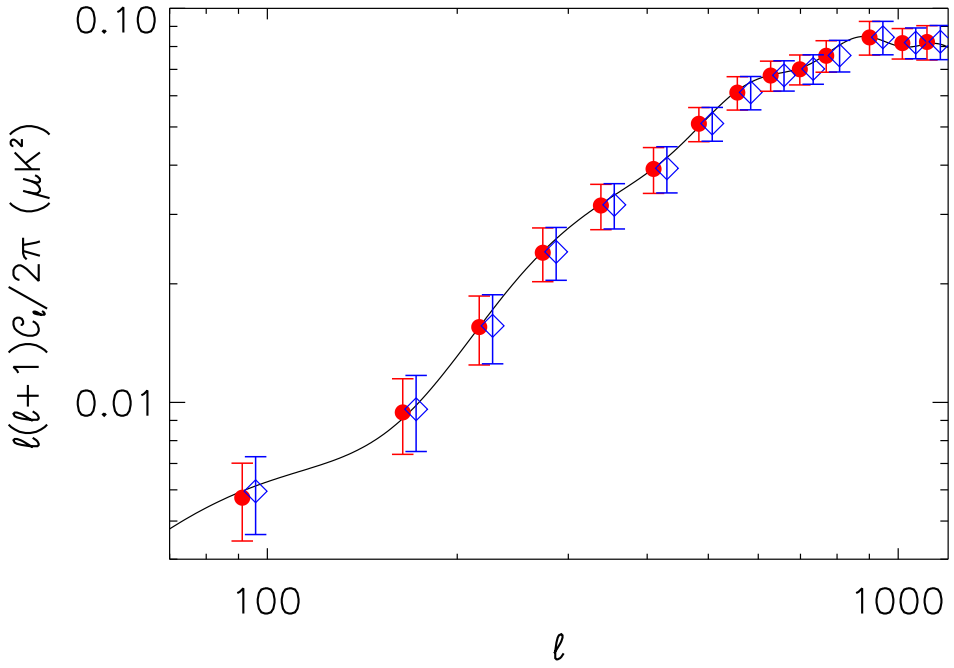

Figure 5.7: The effect of a broad high frequency spectral leak (see text for details) is negligible with $r = 0.05$ and 10% dust polarization. Figure symbols are the same as in Fig. 5.4.

Employing the same dust estimation and subtraction process, but now assuming errors in knowledge of the experiment's detection band-center and band-width, we find the accuracy with which these need to be measured. For example, for the particular experimental configuration considered, we found that band-center and band-width of the 150 GHz band need to be determined to better than 1 and 0.8 GHz, respectively. It is possible that this requirement may not need to be as stringent if a more sophisticated foreground estimation and subtraction process is used. This research is ongoing.

We explore the sensitivity of the particular experimental configuration to high frequency spectral leaks. Using a rejection level that is readily achievable experimentally we show that spectral leaks are not expected to pose challenges for the operation with an AHWP.

The analysis and subtraction approach discussed in this paper are applicable to other optical elements for which polarization rotation is a function of frequency. For example, O'Brient 2010 [60] describes a broadband, mm-wave detection technique that is based on sinuous antenna. It is well documented that such antennas change the phase response of polarized signals, and that this effect is frequency dependent. Thus they exhibit fundamentally the same behavior as an AHWP. Our methods and approach apply to such cases.

Chapter 6

Maximum Likelihood Foreground Cleaning in the Presence of Instrumental Effects

In Chapter 5 we discussed a simple foreground cleaning method in the presence of an AHWP. The simple method, though effective, assumes perfect knowledge of the properties of the AHWP and has rather stringent requirement on the knowledge of the frequency bands. In this chapter I develop a maximum likelihood foreground cleaning algorithm in the presence of instrumental effects. This algorithm is then applied to the challenges posed by using an AHWP specifically. I focus on two instrumental effects in this chapter: the band shape uncertainty and the frequency dependent polarization rotation effect. The algorithm is based on the maximum likelihood component separation technique proposed in Stompor *et al.*, 2009 [61]. In Sec. 6.1 I will address the mathematical framework of the algorithm, including the basic formalism, the extension to include the presence of instrumental effects and the error propagation. I will describe the details of the simulations in Sec. 6.2 and discuss the results in Sec. 6.3. Finally I will make the concluding remark in Sec. 6.4.

6.1 Theoretical Framework

In this section we discuss the mathematical framework of the maximum likelihood foreground cleaning algorithm. We start with a brief review of the basic formalism developed in Stompor *et al.*, 2009 [61] where no instrumental effect is included. Then we introduce the extended cases where band shape uncertainty and frequency dependent polarization rotation effect are incorporated into the framework.

6.1.1 Basic Formalism

In the absence of instrumental effect, the sky signal observed in multiple frequency channels for a single pixel can be modeled as

$$\boldsymbol{d}_p \;=\; \boldsymbol{A}_p\;\boldsymbol{s}_p \;+\; \boldsymbol{n}_p. \tag{6.1}$$

Here the subscript $_p$ denotes quantities for a single pixel; $\boldsymbol{d}_p$ is the data vector containing the measured signals for n_f frequency channels and n_s Stokes parameters; $\boldsymbol{s}_p$ is the underlying sky signal vector for n_c sky signal components and n_s Stokes parameters; $\boldsymbol{n}_p$ is the noise vector for n_f frequency channels and n_s Stokes parameters; $\boldsymbol{A}_p \equiv \boldsymbol{A}_p(\boldsymbol{\beta})$ is the component 'mixing matrix', which is parameterized by a set of unknown parameters $\{\beta_i\}$ describing the spectral shape of the components and has a rank of $n_f \times n_s$ by $n_c \times n_s$. Here we assume the parameters $\{\beta_i\}$ are uniform across the patch.

We can naturally extend the above equation to the case where there are n_p pixels in the observation. We can just remove the subscript $_p$ and the full data model becomes

$$\boldsymbol{d} \;=\; \boldsymbol{A}\;\boldsymbol{s} \;+\; \boldsymbol{n}. \tag{6.2}$$

With the data model defined above we can write the likelihood function for the full data set as

$$-2\;ln\;\mathcal{L}(\boldsymbol{s},\boldsymbol{\beta}) \;=\; const \;+\; (\boldsymbol{d}-\boldsymbol{A}\;\boldsymbol{s})^t\;\boldsymbol{N}^{-1}\;(\boldsymbol{d}-\boldsymbol{A}\;\boldsymbol{s}), \tag{6.3}$$

where $\boldsymbol{N}$ is the noise matrix. In the case where there is no correlated noise between different pixels, $\boldsymbol{N}$ is a rank $n_s \times n_f \times n_p$ square, symmetric, block diagonal noise matrix and the full data likelihood can be calculated as the summation of likelihood values calculated from

each pixels.

When the likelihood reaches its maximum for a particular set of parameters, we have the following relation

$$\boldsymbol{s} \;=\; (\boldsymbol{A}^t\ \boldsymbol{N}^{-1}\ \boldsymbol{A})^{-1}\boldsymbol{A}^t\ \boldsymbol{N}^{-1}\ \boldsymbol{d}. \tag{6.4}$$

By substituting Eq. 6.4 into Eq. 6.3 we get

$$-2\ ln\ \mathcal{L} \;=\; const \;-\; (\boldsymbol{A}^t\boldsymbol{N}^{-1}\boldsymbol{d})^t(\boldsymbol{A}^t\boldsymbol{N}^{-1}\boldsymbol{A})^{-1}(\boldsymbol{A}^t\boldsymbol{N}^{-1}\boldsymbol{d}). \tag{6.5}$$

For a given set of parameters $\{\beta_i\}$, the mixing matrix $\boldsymbol{A}$ can be calculated straightforwardly. Since the only unknown parameters in the likelihood function are the ones in the mixing matrix $\boldsymbol{A}$, the likelihood $\mathcal{L}$ can be directly calculated as well. This drives for a two-step component separation algorithm: first find the set of parameters that maximizes the likelihood function Eq. 6.5, then calculate the component signals given the maximum likelihood parameters using Eq. 6.4. The detailed performance and constraints for this maximum likelihood method has been discussed in Stompor *et al.*, 2009 [61].

6.1.2 Extension of the Basic Formalism

In the basic formalism, the mixing matrix $\boldsymbol{A}$ has $n_c \times n_f$ blocks. Each block is a n_s by n_s diagonal matrix with all of its diagonal elements equal to each other. The only unknown parameters in $\boldsymbol{A}$ are the spectral shape parameters β_i of the dust components. When extending the basic formalism to include instrumental effects, the mixing matrix $\boldsymbol{A}$ takes more complicated format while the main steps of the foreground cleaning algorithm remains. Here we extend the basic formalism to two cases: band shape uncertainty and frequency dependent polarization rotation effect. We will also discuss the combination of the two effects.

Band Shape Uncertainty

First we extend the formalism to include the band shape uncertainty. The band shape uncertainty is different from an overall band calibration factor which was addressed in Stompor *et al.*, 2009 [61]. The overall band calibration factor is a single multiplicative factor which applies to all signals in a specific band. The band shape uncertainty, however,

is related to the detailed structure of a specific band and affects different sky signals differently. A band is expressed in terms of transmission as a function of frequency $T(\nu)$. For an arbitrary band shape, we can define the band-center and band-width parameters to characterize the band shape. Here we use the same definition of band-center and band-width as in Chapter 4. The band-center ν_c is defined as

$$\nu_c \;=\; \frac{\int \nu\; T(\nu)\; d\nu}{\int T(\nu)\; d\nu}, \tag{6.6}$$

which is the mean frequency weighed by the transmission. The band-width is defined as

$$\Delta\nu \;=\; \nu_U - \nu_L, \tag{6.7}$$

where the lower and upper band edges are defined as

$$\nu_U \;=\; \frac{\int_{\nu_c}^{\infty} \nu T'(\nu) d\nu}{\int_{\nu_c}^{\infty} T'(\nu) d\nu}\;,\; \nu_L \;=\; \frac{\int_{0}^{\nu_c} \nu T'(\nu) d\nu}{\int_{0}^{\nu_c} T'(\nu) d\nu}. \tag{6.8}$$

Here $T'(\nu)$ is the derivative of the transmission curve $T(\nu)$. This definition of band edges favors frequencies where sharp transitions happen in the band curve [51]. Given the definitions above, any uncertainties in the band shape can be translated to uncertainties in band-center and band-width.

For any incoming sky signal, the band shape uncertainties propagate to the total measured in-band power, which is related to the emission spectral shape of the sky signal. In the case where there are multiple sky components with different spectral shapes, the in-band power of each component is affected differently. Here we characterize the uncertainty of the in-band power by introducing a scaling coefficient, denoted as $\boldsymbol{\eta}$. The scaling coefficient $\eta_{nu,s}$ is defined as the ratio between the actual in-band power and the assumed in-band power for component s at frequency band ν. Each sky signal component in each frequency band has a different value for the coefficient η. Fig. 6.1 shows a visualization of the definition of $\boldsymbol{\eta}$. In the case where the band is measured accurately, the band scaling coefficient is unity for any sky signal. When the spectral shape of the components are assumed to be uniform across the patch, these coefficients are considered to be universal across all pixels as well.

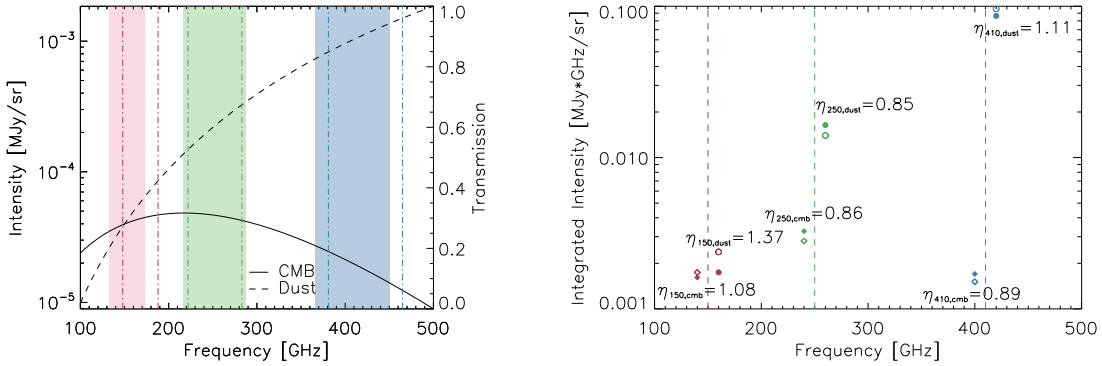

Figure 6.1: Illustration of the definition of in-band scaling coefficient η. In this example we have two sky signal components: the CMB and the polarized galactic thermal dust emission. There are three top-hat bands centered around 150 GHz, 250 GHz and 410 GHz in this example. Left panel: the CMB (solid) and the galactic thermal dust (dashed) spectra. The CMB spectrum is the CMB anisotropy spectrum assuming a $0.1\mu K_{CMB}$ signal level, which is the inflationary B-mode signal level at $\ell = 80$ with a tensor-to-scalar ratio $r = 0.1$. The dust spectrum is a 19.6 K black body with a 1.59 power law emissivity based on recent Planck measurement [52] with the signal level equal to 0.1 μK_{CMB} at 150 GHz. This is the dust B-mode signal level for a clean patch of the sky. The three solid bands are the assumed band shapes while the three dot-dashed bands are the actual bands in the simulation. Compared to the assumed bands, the actual 150 GHz band and the 410 GHz band are shifted by 15 GHz while having the same band-width; the 250 GHz band has a band-width reduced by 10 GHz while having the same band center. Right panel: the CMB (diamond) and dust (circle) intensity integrated over the bands. The CMB and dust data points are offset along the x-axis for clarity. The in-band scaling coefficients are the ratio between the actual band integrated signal (open symbols) and the assumed band integrated signal (filled symbols). The coefficients for CMB and dust at each frequency are labeled by the data points. Due to the difference between the CMB and dust spectra, the two components have different scaling coefficients given the same band mismatch.

To incorporate the band shape uncertainties into the foreground cleaning algorithm, we consider the band parameters as part of the unknown parameters in the mixing matrix and optimize these parameters with the maximum likelihood algorithm. We decide to approach the problem by fitting the band scaling coefficients instead of fitting for the band-center and band-width, because it is computationally expensive to calculate the mixing matrix using band-center and band-width. We introduce a new mixing matrix $\boldsymbol{A}_B(\boldsymbol{\beta}, \boldsymbol{\eta})$ with band uncertainty included , which has the same rank as the original mixing matrix $\boldsymbol{A}$. Each n_s by n_s block in $\boldsymbol{A}_B$ is multiplied by the band scaling coefficient for corresponding frequency channel and sky component. Since each of the coefficients are different, it is not trivial to express $\boldsymbol{A}_B(\boldsymbol{\beta}, \boldsymbol{\eta})$ as the multiplication between a scaling matrix and the original mixing matrix $\boldsymbol{A}$.

With $\boldsymbol{A}_B$ we can then rewrite the data model as

$$\widetilde{\boldsymbol{d}} \;=\; \boldsymbol{A}_B(\boldsymbol{\eta}, \boldsymbol{\beta})\; \boldsymbol{s} \;+\; \boldsymbol{n}, \tag{6.9}$$

where $\widetilde{\boldsymbol{d}}$ is the observed data with the band shape effect. And we can rewrite the likelihood function as

$$-2\; ln\; \mathcal{L}_B(\boldsymbol{s}, \boldsymbol{\beta}) \;=\; const \;+\; (\widetilde{\boldsymbol{d}} - \boldsymbol{A}_B\; \boldsymbol{s})^t\; \boldsymbol{N}^{-1}\; (\widetilde{\boldsymbol{d}} - \boldsymbol{A}_B\; \boldsymbol{s}). \tag{6.10}$$

When the likelihood reaches maximum we have

$$-2\; ln\; \mathcal{L}_B \;=\; const \;-\; (\boldsymbol{A}_B^t \boldsymbol{N}^{-1} \widetilde{\boldsymbol{d}})^t (\boldsymbol{A}_B^t \boldsymbol{N}^{-1} \boldsymbol{A}_B)^{-1} (\boldsymbol{A}_B^t \boldsymbol{N}^{-1} \widetilde{\boldsymbol{d}}), \tag{6.11}$$

and

$$\boldsymbol{s} \;=\; (\boldsymbol{A}_B^t\; \boldsymbol{N}^{-1}\; \boldsymbol{A}_B)^{-1} \boldsymbol{A}_B^t\; \boldsymbol{N}^{-1}\; \widetilde{\boldsymbol{d}}. \tag{6.12}$$

There are two types of degeneracies between the unknown parameters here. First, there is a degeneracy between the signal level and all three band scaling coefficients for a particular sky component. Multiplying the band scaling coefficients by a factor at the same time is equivalent to having the sky signal multiplied by the same factor. Second, there is a degeneracy between the dust spectral parameters and the dust in-band scaling coefficients. Tilting the spectrum is equivalent to changing two of the scaling coefficients at

corresponding factors. Fig. 6.2 shows an illustration of this degeneracy. In the example, a mis-estimate of the dust spectral index by 0.2 has the same η_{150} and η_{250} as a mis-estimate of the band-center at the 150 band by -8.5 GHz and the band-width at the 250 band by -6 GHz.

To lift the degeneracies, we can set prior constraints on the scaling coefficients. In practice, the bands are typically measured to certain accuracy level so it is reasonable to constrain the coefficients to a subset of the parameter space. If we assume η_i is measured with an uncertainty σ_{η_i} around some value $\bar{\eta_i}$, then the likelihood function can be modified to

$$-2\ ln\ \mathcal{L}_B(\boldsymbol{\eta},\boldsymbol{\beta}) = const - (\boldsymbol{A}_B^t \boldsymbol{N}^{-1} \widetilde{\boldsymbol{d}})^t (\boldsymbol{A}_B^t \boldsymbol{N}^{-1} \boldsymbol{A}_B)^{-1} (\boldsymbol{A}_B^t \boldsymbol{N}^{-1} \widetilde{\boldsymbol{d}}) + \sum_i \frac{(\eta_i - \bar{\eta_i})^2}{\sigma_{\eta_i}^2}, \quad (6.13)$$

where the last term represents the prior constraints on the scaling coefficients. We can use Eq. 6.13 to find the best estimates of the spectral parameters and the scaling coefficients. Then we can use those parameters in the second step to recover best fit sky component signals.

Frequency Dependent Polarization Rotation Effect

Next we extend the formalism to include the frequency dependent polarization rotation effect. As an concrete example, we use the rotation effect caused by the EBEX AHWP discussed in Chapter 4. The rotation effect 'mixes' the Q and U signal from the sky in the observed data. The rotation of total signal detected within certain band depends on the spectral shape of the incoming signal, the AHWP characteristic parameters and the observation band shapes.

To incorporate the frequency dependent rotation effect into the maximum likelihood foreground cleaning algorithm, we rewrite the model for the whole data set as

$$\widetilde{\boldsymbol{d}} \ = \ \boldsymbol{A}_R(\boldsymbol{\theta},\boldsymbol{\beta})\ \boldsymbol{s} \ + \ \boldsymbol{n}, \quad (6.14)$$

where $\widetilde{\boldsymbol{d}}$ denotes the observed data with the rotation effect; $\boldsymbol{A}_R$ is the new mixing matrix with the rotation effect incorporated in which has the same rank as the original mixing matrix $\boldsymbol{A}$; $\boldsymbol{\theta} \equiv \boldsymbol{\theta}(\boldsymbol{\beta})$ is the vector of rotation angles for each sky signal component in each

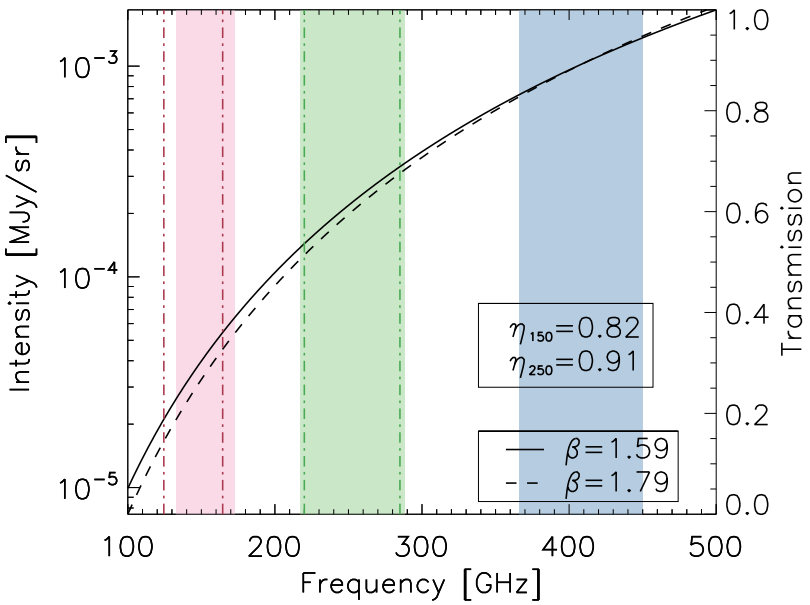

Figure 6.2: Illustration of degeneracy between the in-band scaling coefficient for dust η_d and the dust spectral index β. We have an assumed dust spectrum (solid) and three frequency bands (filled color bands). The dust spectrum has a spectral index of 1.59 and a signal level of 0.1 μK_CMB at 150 GHz. If the actual dust spectrum (dashed) has a spectral index of 1.79 and is normalized to the assumed dust spectrum at 410 GHz band, we have $\eta_{150} = 0.82$ and $\eta_{250} = 0.91$. If the actual 150 GHz band is shifted by -8.5 GHz and the actual 250 GHz band has reduced band-width by 6 GHz compared to the assumed bands, we also have $\eta_{150} = 0.82$ and $\eta_{250} = 0.91$. In this case, a mis-estimate of the dust spectral index has the same η_{150} and η_{250} as a mis-estimate of the 150 and 250 bands.

frequency channel; $\boldsymbol{s}$ and $\boldsymbol{n}$ remains the same definition as in Sec. 6.1.1. Once we introduce the rotation effect, the mixing matrix $\boldsymbol{A}_R$ is not block diagonal any more. Instead, the 2×2 Q-U blocks for each sky signal component at each frequency channel in $\boldsymbol{A}_R$ are multiplied by rotation matrices with non-zero rotation angles $\boldsymbol{\theta}_{s,\nu}$.

Here we choose to include the rotation angles $\boldsymbol{\theta}$ directly as unknown parameters instead of calculating them from instrumental parameters. The algorithm fits the dust spectral indices simultaneously with the rotation angles. There are two advantages of this treatment: first it does not require accurate knowledge of the instrumental parameters such as observation band shapes and AHWP characteristic parameters, second it is less computationally expensive.

Given the definition of $\boldsymbol{A}_R$, we can write the new likelihood function of the full data set as

$$-2\ ln\ \mathcal{L}_R(\boldsymbol{s},\boldsymbol{\beta})\ =\ const\ +\ (\widetilde{\boldsymbol{d}}-\boldsymbol{A}_R\ \boldsymbol{s})^t\ \boldsymbol{N}^{-1}\ (\widetilde{\boldsymbol{d}}-\boldsymbol{A}_R\ \boldsymbol{s}). \tag{6.15}$$

When the likelihood reaches its maximum we have

$$-2\ ln\ \mathcal{L}_R\ =\ const\ -\ (\boldsymbol{A}_R^t\boldsymbol{N}^{-1}\widetilde{\boldsymbol{d}})^t(\boldsymbol{A}_R^t\boldsymbol{N}^{-1}\boldsymbol{A}_R)^{-1}(\boldsymbol{A}_R^t\boldsymbol{N}^{-1}\widetilde{\boldsymbol{d}}), \tag{6.16}$$

and

$$\boldsymbol{s}\ =\ (\boldsymbol{A}_R^t\ \boldsymbol{N}^{-1}\ \boldsymbol{A}_R)^{-1}\boldsymbol{A}_R^t\ \boldsymbol{N}^{-1}\ \widetilde{\boldsymbol{d}}. \tag{6.17}$$

The two step structure of the foreground cleaning method remains: first we find the set of parameters that maximizes the likelihood function Eq. 6.16, then we calculate the sky signals given the maximum likelihood parameters using Eq. 6.17.

There exists a degeneracy between the instrumental rotation effect and the polarization angle of the incoming signal. Changing the rotation angles of a sky component in all bands by a given amount is equivalent to changing the incoming polarization signal by the same amount. In practice, the frequency dependent rotation effects can be calibrated to some accuracy. So a prior of the polarization angle can be set to life the degeneracy. If we assume θ_i is determined within an uncertainty σ_{θ_i} around some value $\bar{\theta}_i$ given the knowledge of

the instrument and the incoming signals, the likelihood function can be modified to

$$-2\ ln\ \mathcal{L}_R(\boldsymbol{\eta},\boldsymbol{\beta}) = const - (\boldsymbol{A}_R^t\boldsymbol{N}^{-1}\widetilde{\boldsymbol{d}})^t(\boldsymbol{A}_R^t\boldsymbol{N}^{-1}\boldsymbol{A}_R)^{-1}(\boldsymbol{A}_R^t\boldsymbol{N}^{-1}\widetilde{\boldsymbol{d}}) + \sum_i \frac{(\theta_i-\bar{\theta}_i)^2}{\sigma_{\theta_i}^2}, \quad (6.18)$$

where the last term originates from the prior constraints on the rotation angles. We can maximize Eq. 6.18 to find the best estimates of spectral parameters and rotation angles. Then we can use those values in the second step with Eq. 6.18 to recover the best fit sky component signals.

Combining the Band Shape and Rotation effect

In this section we extend the formalism to cases where both the band shape uncertainty and the frequency dependent polarization rotation effect are present. First we can rewrite the data model as

$$\widetilde{\boldsymbol{d}} \ = \ \boldsymbol{A}_C(\boldsymbol{\theta},\boldsymbol{\eta},\boldsymbol{\beta})\ \boldsymbol{s} \ + \ \boldsymbol{n}, \quad (6.19)$$

where $\boldsymbol{A}_C(\boldsymbol{\theta},\boldsymbol{\eta},\ \boldsymbol{\beta})$ is the combined mixing matrix which contains the rotation angles $\boldsymbol{\theta}$, the band shape scaling coefficients $\boldsymbol{\eta}$ and the dust spectral parameters $\boldsymbol{\beta}$ as unknown parameters. Each n_s by n_s block in $\boldsymbol{A}_C$ is multiplied by the in-band scaling coefficient η_i for the corresponding signal component and frequency band. Also each of the 2×2 Q-U block within the n_s by n_s block is multiplied by a rotation matrix with rotation angle θ_i.

We can then rewrite the likelihood function of the data set as

$$-2\ ln\ \mathcal{L}_C(\boldsymbol{s},\boldsymbol{\beta}) \ = \ const \ + \ (\widetilde{\boldsymbol{d}} - \boldsymbol{A}_C\ \boldsymbol{s})^t\ \boldsymbol{N}^{-1}\ (\widetilde{\boldsymbol{d}} - \boldsymbol{A}_C\ \boldsymbol{s}). \quad (6.20)$$

When the likelihood reaches its maximum we have

$$-2\ ln\ \mathcal{L}_C \ = \ const \ - \ (\boldsymbol{A}_C^t\boldsymbol{N}^{-1}\widetilde{\boldsymbol{d}})^t(\boldsymbol{A}_C^t\boldsymbol{N}^{-1}\boldsymbol{A}_C)^{-1}(\boldsymbol{A}_C^t\boldsymbol{N}^{-1}\widetilde{\boldsymbol{d}}), \quad (6.21)$$

and

$$\boldsymbol{s} \ = \ (\boldsymbol{A}_C^t\ \boldsymbol{N}^{-1}\ \boldsymbol{A}_C)^{-1}\boldsymbol{A}_C^t\ \boldsymbol{N}^{-1}\ \widetilde{\boldsymbol{d}}. \quad (6.22)$$

The two step structure of the foreground cleaning method remains the same: first we maximize the likelihood function Eq. 6.21 to find the best fit dust spectral parameters,

the in-band scaling coefficients and the instrumental polarization rotation angles; then we calculate the component signals with the maximum likelihood parameters using Eq. 6.22.

Due to the degeneracies mentioned in Sec. 6.1.2 and Sec. 6.1.2, to recover the signals correctly we set prior constraints to the parameters fitted by the algorithm. When the in-band scaling coefficients $\boldsymbol{\eta}$ and the band averaged rotation angles $\boldsymbol{\theta}$ have prior constraints, we have the updated likelihood function

$$-2\ ln\ \mathcal{L}_C(\boldsymbol{\eta},\boldsymbol{\beta})\ =\ const\ -\ (\boldsymbol{A}_C^t\boldsymbol{N}^{-1}\widetilde{\boldsymbol{d}})^t(\boldsymbol{A}_C^t\boldsymbol{N}^{-1}\boldsymbol{A}_C)^{-1}(\boldsymbol{A}_C^t\boldsymbol{N}^{-1}\widetilde{\boldsymbol{d}}) + \sum_i \frac{(\eta_i-\bar{\eta_i})^2}{\sigma_{\eta_i}^2}\ +\ \sum_i \frac{(\theta_i-\bar{\theta_i})^2}{\sigma_{\theta_i}^2}, \quad (6.23)$$

where the last two terms come from the prior constraints.

6.1.3 Error Propagation

When noise is present in the observation, there exist uncertainties in the estimated sky signals. The uncertainties in the estimated sky component maps can be calculated from the noise in the observed maps by

$$\hat{\boldsymbol{N}} \equiv (\boldsymbol{A}^t\boldsymbol{N}^{-1}\boldsymbol{A})^{-1}, \quad (6.24)$$

when the the dust spectral parameters and the instrumental parameters in the mixing matrix are perfectly known. When the parameters are also estimated by the algorithm, any uncertainties in the estimated parameters propagate to the estimated sky component signals.

Here we estimate the covariance matrix for the parameters using the inverse of the curvature matrix calculated at the maximum likelihood. Specifically, for the basic formalism we have

$$\tilde{\boldsymbol{N}}_{\beta\beta} = \{(\boldsymbol{A}_{,\beta_i}\,\boldsymbol{s})^t\boldsymbol{N}^{-1}(\boldsymbol{A}_{,\beta_j}\,\boldsymbol{s}) - (\boldsymbol{A}_{,\beta_i\beta_j}\,\boldsymbol{s})^t\boldsymbol{N}^{-1}(\boldsymbol{d}-\boldsymbol{A}\,\boldsymbol{s}) - \boldsymbol{M}^t\hat{\boldsymbol{N}}\boldsymbol{M}\}^{-1} \quad (6.25)$$

for the spectral parameters, where the $\boldsymbol{M}$ matrix is defined as

$$\boldsymbol{M}\ =\ \boldsymbol{A}^t\boldsymbol{N}^{-1}\boldsymbol{A}_{,\beta}\,\boldsymbol{s} - \boldsymbol{A}^t{}_{,\beta}\,\boldsymbol{N}^{-1}(\boldsymbol{d}-\boldsymbol{A}\,\boldsymbol{s}). \quad (6.26)$$

Here $\hat{\boldsymbol{N}}$ is the estimated uncertainty matrix without error propagation. $\boldsymbol{A}_{,\boldsymbol{\beta}}$ and $\boldsymbol{A}_{,\boldsymbol{\beta\beta}}$ are the first and second order derivatives of the mixing matrix with respect to the spectral parameters. The matrices are estimated at the best fit values for the parameters. Then the noise matrix of the estimated sky signals with error propagation included is

$$\tilde{\boldsymbol{N}}_{ss} = \hat{\boldsymbol{N}} + (\hat{\boldsymbol{N}}\boldsymbol{M})\tilde{\boldsymbol{N}}_{\beta\beta}(\hat{\boldsymbol{N}}\boldsymbol{M})^t. \tag{6.27}$$

For error propagation in the extended cases, the mixing matrix $\boldsymbol{A}$ in Eq. 6.27, Eq. 6.25 and Eq. 6.26 is changed to the corresponding extended mixing matrix ($\boldsymbol{A}_B$, $\boldsymbol{A}_R$ or $\boldsymbol{A}_C$) and the derivative of the mixing matrix is performed with respect to all corresponding unknown parameters including the dust spectral parameters $\boldsymbol{\beta}$, the in-band scaling coefficients $\boldsymbol{\eta}$ and the band averaged rotation angles $\boldsymbol{\theta}$.

6.2 Simulations

To test the effectiveness of the extended algorithm, we implement and apply the algorithm on simulated data. As a concrete example, we use the parameters from the E and B experiment [39] as the input in the simulation. We select a $20^\circ \times 20^\circ$ sky patch centered on RA $= 55^\circ$, DEC $= -45^\circ$ which overlaps with the planned EBEX patch. Here we only consider CMB and dust as the sky components in the patch. The input CMB angular power spectra are generated with Code for Anisotropies in the Microwave Background [53] using the Wilkinson Microwave Anisotropy Probe (WMAP) seven-year best-fit cosmological parameters [54] and a tensor to scalar ratio of $r = 0.05$. For galactic dust foreground we adopt the process detailed in Stivoli *et. al*, 2010 [55] and we briefly review the process here. The dust intensity and its frequency scaling are given by an $19.6K$ black body with a 1.59 power law emissivity according to the recent Planck measurement [52]. The dust polarization fraction is set to 10%. Both the dust frequency scaling and the dust polarization fraction are assumed to be uniform across the chosen sky area. The large scale polarization angle patterns ($l \lesssim 100$) is derived from WMAP dust polarization template [29]. On small angular scales a Gaussian fluctuation power is added using the recipe described in Giardino *et. al*, 2002 [57]. Fig. 6.3 shows the Q and U maps of the CMB and dust signal in the selected sky patch.

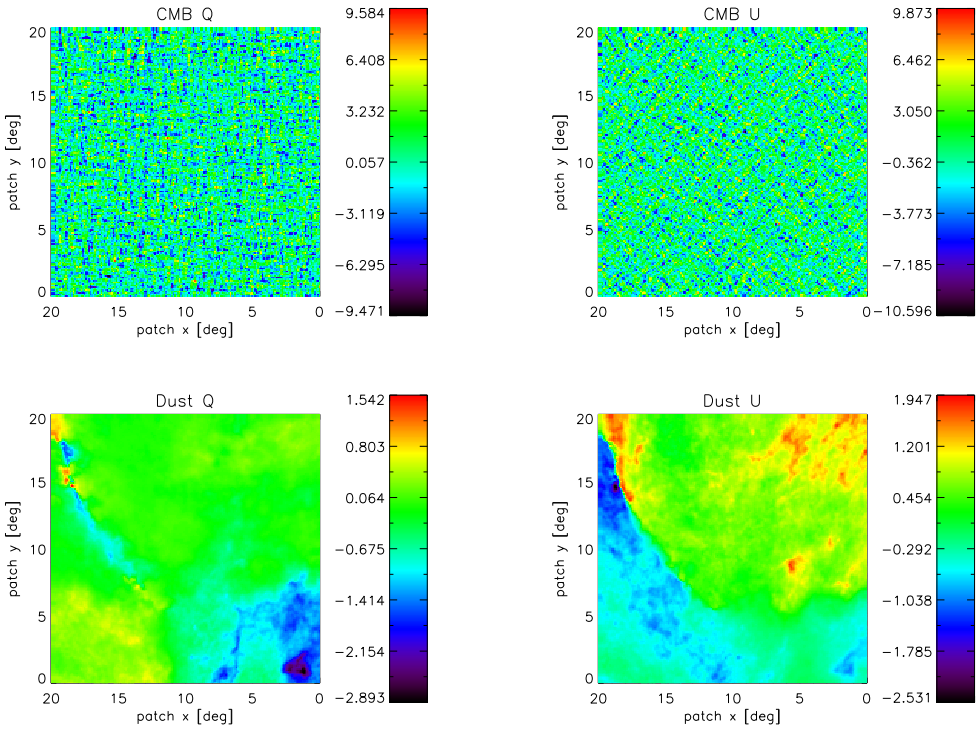

Figure 6.3: Q (left column) and U (right column) maps of one realization of CMB (top row) and dust (bottom row) at 150 GHz band on the sky patch chosen for simulation. The maps are in units of μK_{RJ}.

EBEX top-hat band	Band frequency range [GHz]	Noise in Q and U maps [μK_{RJ}]
150 GHz	[133, 173]	0.8
250 GHz	[217, 288]	1.0
410 GHz	[366, 450]	1.4

Table 6.1: EBEX bands and the corresponding noise per $6.87' \times 6.87'$ pixel in the Q and U maps which are used in the simulation.

The observations are simulated in three top-hat bands centered at 150 GHz, 250 GHz and 410 GHz, which are the designed EBEX frequency bands. The frequency ranges for the three bands are listed in Table 6.1. The noise levels per $6.87' \times 6.87'$ pixel in the Q and U maps at the three bands are also listed in Table 6.1. The noise is assumed to be uniform and white across the patch. The noise realization is added to the signal in the map domain in all simulations. EBEX utilizes a continuously rotating achromatic half-wave plate which induces a frequency dependent polarization rotation effect. In the simulation we use a five-stack AHWP based on the designed EBEX AHWP. It is composed of single sapphire HWPs with a thickness of 1.65 mm each. The designed relative orientation angles between the optical axis of the plates and the first plate in the stack are 0°, 28°, 94°, 28°, 0°. Since the EBEX AHWP is operated at cryogenic temperature, the spectral indices of the sapphire at cryogenic temperature are used in the calculation, i.e. $n_o = 3.047$ and $n_e = 3.361$. Given the frequency bands, the input dust spectrum and the AHWP parameters, the rotation angles are 115.66°, 103.64°, 110.76° for CMB and 115.02°, 103.68°, 112.88° for dust at 150,250,410 GHz bands, respectively. Fig. 6.4 shows the observed Q and U maps at 150 GHz band after the AHWP rotation effect and instrumental noise.

The EE and BB power spectra on the patch are calculated simultaneously using the flat-sky approximation [58]. For each set of input parameters, the simulation is run 100 times with different CMB and noise realization while the dust signal is kept the same. The result shown for any given ℓ bin is the mean of the 100 simulations and the plotted error bar is the standard deviation of the 100 simulations.

Given the simulation parameters we can write out the specific data model for the problem in the basic case without instrumental effects:

$$\boldsymbol{d} = \boldsymbol{A}\,\boldsymbol{s} + \boldsymbol{n}, \tag{6.28}$$

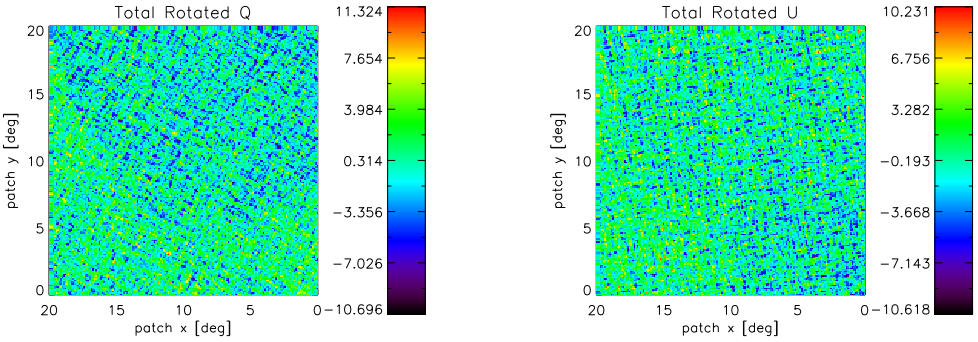

Figure 6.4: Q (left) and U (right) maps of observation at 150 GHz band with AHWP rotation effect and instrumental noise included. This is one realization of the CMB and instrumental noise. The maps are in units of μK_{RJ}.

becomes

$$\begin{pmatrix} I_{150} \\ Q_{150} \\ U_{150} \\ I_{250} \\ Q_{250} \\ U_{250} \\ I_{410} \\ Q_{410} \\ U_{410} \end{pmatrix} = \begin{pmatrix} A_{150,c} & 0 & 0 & A_{150,d}(\beta) & 0 & 0 \\ 0 & A_{150,c} & 0 & 0 & A_{150,d}(\beta) & 0 \\ 0 & 0 & A_{150,c} & 0 & 0 & A_{150,d}(\beta) \\ A_{250,c} & 0 & 0 & A_{250,d}(\beta) & 0 & 0 \\ 0 & A_{250,c} & 0 & 0 & A_{250,d}(\beta) & 0 \\ 0 & 0 & A_{250,c} & 0 & 0 & A_{250,d}(\beta) \\ A_{410,c} & 0 & 0 & A_{410,d}(\beta) & 0 & 0 \\ 0 & A_{410,c} & 0 & 0 & A_{410,d}(\beta) & 0 \\ 0 & 0 & A_{410,c} & 0 & 0 & A_{410,d}(\beta) \end{pmatrix} \begin{pmatrix} I_{CMB} \\ Q_{CMB} \\ U_{CMB} \\ I_{dust} \\ Q_{dust} \\ U_{dust} \end{pmatrix} + \begin{pmatrix} n_{I_{150}} \\ n_{Q_{150}} \\ n_{U_{150}} \\ n_{I_{250}} \\ n_{Q_{250}} \\ n_{U_{250}} \\ n_{I_{410}} \\ n_{Q_{410}} \\ n_{U_{410}} \end{pmatrix}. \quad (6.29)$$

Here I, Q and U are the polarization stokes parameters. The subscripts denote frequency channels and components. The elements in the mixing matrix related to CMB are known since the CMB spectrum is known. For any given frequency ν, the elements in the mixing matrix related to dust can be expressed as

$$A_{\nu,d}(\beta) \;=\; (\frac{\nu}{\nu_0})^{\beta} B_{\nu}(T_d, \nu), \quad (6.30)$$

where ν_0 is a reference frequency typically set to be the highest frequency channel of the experiment, B_ν is the black body spectrum, T_d is the dust temperature which is assumed to be a known value in the simulations here and β is the spectral index of dust which is

the sole unknown parameter in this case.

For the extended case where the band uncertainties are included, the mixing matrix becomes

$$\boldsymbol{A}_B = \begin{pmatrix} A_{150,c}\eta_{150,c} & 0 & 0 & A_{150,d}(\beta)\eta_{150,d} & 0 & 0 \\ 0 & A_{150,c}\eta_{150,c} & 0 & 0 & A_{150,d}(\beta)\eta_{150,d} & 0 \\ 0 & 0 & A_{150,c}\eta_{150,c} & 0 & 0 & A_{150,d}(\beta)\eta_{150,d} \\ A_{250,c}\eta_{250,c} & 0 & 0 & A_{250,d}(\beta)\eta_{250,d} & 0 & 0 \\ 0 & A_{250,c}\eta_{250,c} & 0 & 0 & A_{250,d}(\beta)\eta_{250,d} & 0 \\ 0 & 0 & A_{250,c}\eta_{250,c} & 0 & 0 & A_{250,d}(\beta)\eta_{250,d} \\ A_{410,c}\eta_{410,c} & 0 & 0 & A_{410,d}(\beta)\eta_{410,d} & 0 & 0 \\ 0 & A_{410,c}\eta_{410,c} & 0 & 0 & A_{410,d}(\beta)\eta_{410,d} & 0 \\ 0 & 0 & A_{410,c}\eta_{410,c} & 0 & 0 & A_{410,d}(\beta)\eta_{410,d} \end{pmatrix}. \quad (6.31)$$

Here $\{\eta_{\nu,s}\}$ are the in-band scaling coefficients and the subscripts denotes the frequency channel and the sky signal component. Each block in $\boldsymbol{A}_B$ remains diagonal and the elements of each block are multiplied by the corresponding coefficients. Once band uncertainties are introduced into the problem, the number of unknowns expands up to seven: the spectral index and six scaling coefficients.

For the extended case where the frequency dependent rotation effect of an AHWP is included, the mixing matrix becomes

$$\boldsymbol{A}_R = \begin{pmatrix} \boldsymbol{A}_{R_{150,c}} & \boldsymbol{A}_{R_{150,d}} \\ \boldsymbol{A}_{R_{250,c}} & \boldsymbol{A}_{R_{250,d}} \\ \boldsymbol{A}_{R_{410,c}} & \boldsymbol{A}_{R_{410,d}} \end{pmatrix}, \quad (6.32)$$

with the blocks $\boldsymbol{A}_{R_{\nu,s}}$ for CMB and dust at frequency channel ν are

$$\boldsymbol{A}_{R_{\nu,c}} = \begin{pmatrix} A_{\nu,c} & 0 & 0 \\ 0 & A_{\nu,c}Cos\theta_{\nu,c} & -A_{\nu,c}Sin\theta_{\nu,c} \\ 0 & A_{\nu,c}Sin\theta_{\nu,c} & A_{\nu,c}Cos\theta_{\nu,c} \end{pmatrix},$$

$$\boldsymbol{A}_{R_{\nu,d}} = \begin{pmatrix} A_{\nu,d}(\beta) & 0 & 0 \\ 0 & A_{\nu,d}(\beta)Cos\theta_{\nu,d}(\beta) & -A_{\nu,d}(\beta)Sin\theta_{\nu,d}(\beta) \\ 0 & A_{\nu,d}(\beta)Sin\theta_{\nu,d}(\beta) & A_{\nu,d}(\beta)Cos\theta_{\nu,d}(\beta) \end{pmatrix},$$

where the subscript ν runs for 150, 250 and 410. Here $\{\theta_{\nu,s}\}$ are the AHWP induced rotation angles and the subscripts denotes the frequency channel and the sky signal component. Each Q and U block in $\boldsymbol{A}_R$ is multiplied by a rotation matrix with the corresponding rotation angle and is not diagonal any more. With the rotation angles, there are seven unknown parameters fitted simultaneously by the algorithm: spectral index and six rotation angles.

For the extended case where both the band shape uncertainty and the frequency dependent rotation effect of the AHWP are considered, the mixing matrix with the combined effects becomes

$$\boldsymbol{A}_C = \begin{pmatrix} \boldsymbol{A}_{C_{150,c}} & \boldsymbol{A}_{C_{150,d}} \\ \boldsymbol{A}_{C_{250,c}} & \boldsymbol{A}_{C_{250,d}} \\ \boldsymbol{A}_{C_{410,c}} & \boldsymbol{A}_{C_{410,d}} \end{pmatrix}, \tag{6.33}$$

with the blocks $\boldsymbol{A}_{C_{\nu,s}}$ for CMB and dust at frequency channel ν are

$$\boldsymbol{A}_{C_{\nu,c}} = \begin{pmatrix} \eta_{\nu,c}A_{\nu,c} & 0 & 0 \\ 0 & \eta_{\nu,c}A_{\nu,c}Cos\theta_{\nu,c} & -\eta_{\nu,c}A_{\nu,c}Sin\theta_{\nu,c} \\ 0 & \eta_{\nu,c}A_{\nu,c}Sin\theta_{\nu,c} & \eta_{\nu,c}A_{\nu,c}Cos\theta_{\nu,c} \end{pmatrix},$$

$$\boldsymbol{A}_{C_{\nu,d}} = \begin{pmatrix} \eta_{\nu,d}A_{\nu,d}(\beta) & 0 & 0 \\ 0 & \eta_{\nu,d}A_{\nu,d}(\beta)Cos\theta_{\nu,d}(\beta) & -\eta_{\nu,d}A_{\nu,d}(\beta)Sin\theta_{\nu,d}(\beta) \\ 0 & \eta_{\nu,d}A_{\nu,d}(\beta)Sin\theta_{\nu,d}(\beta) & \eta_{\nu,d}A_{\nu,d}(\beta)Cos\theta_{\nu,d}(\beta) \end{pmatrix},$$

where the subscript ν runs for 150, 250 and 410. Each 3 by 3 $\boldsymbol{A}_{\nu,s}$ block is multiplied by the corresponding in-band scaling factor $\eta_{\nu,s}$ and the Q and U block is multiplied by a rotation matrix with corresponding rotation angle $\theta_{\nu,s}$. There are a total of 13 unknown parameters in $\boldsymbol{A}_C$: the spectral index, six in-band power scaling coefficients and six band averaged rotation angles.

6.3 Results

In this section we present simulation results in various configurations from the extended algorithm with band shape uncertainty and frequency dependent polarization rotation effect included. In all the results presented here, we consider the mean recovered CMB B-mode signal being biased if it is twice the cosmic variance away from the mean input

CMB B-mode signal. This is a rather stringent requirement. Implementing a more relaxed requirement for bias can be a topic for future research.

First we demonstrate that the extended algorithm produces the same result as the basic formalism in the simple case where both the band shape uncertainty and the frequency dependent polarization rotation effect are not present. The in band scaling coefficients and the rotation angles are included in the calculation, but are assumed to be perfectly known rather than being estimated by the algorithm. Nominal EBEX instrumental noise is included in all maps and the only parameter estimated by the algorithm is the spectral index of dust. As shown in Figure 6.5, the method can recover the input CMB B-mode power spectrum without any bias in this case. The data points of the estimated CMB B-mode power spectrum are plotted offset along the x-axis for clarity and this applies to all the power spectra plots in this section. In all of the results we also plot the theoretical CMB B-mode power spectrum assuming $r = 0.05$ where the input CMB maps are generated from.

6.3.1 Band Shape Uncertainty

Here we assess the capability of the algorithm to extract the CMB B-mode signal in the presence of band shape uncertainty. All the band averaged rotation angles are assumed to be perfectly known and fixed at the input values in the simulations.

No noise

We first assess the intrinsic bias to the extracted CMB signal induced by the method itself. The simulations are performed in the absence of instrumental noise. Due to the degeneracies mentioned in Sec. 6.1.2, when allowing more than one band to change the algorithm has trouble converging on the best fit parameters. So in this part of the simulation we fix two of the bands to be the input value and fit for the scaling coefficients related to the last band together with the spectral index.

Fig. 6.6 shows the result when 250 GHz and 410 GHz bands are perfectly known and 150 GHz band has a band-center mismatch of 10 GHz. The algorithm is capable of fitting for the right spectral index and scaling coefficients for CMB and dust at 150 GHz. The recovered CMB B-mode power spectrum has no bias. Similarly when there is a 10 GHz

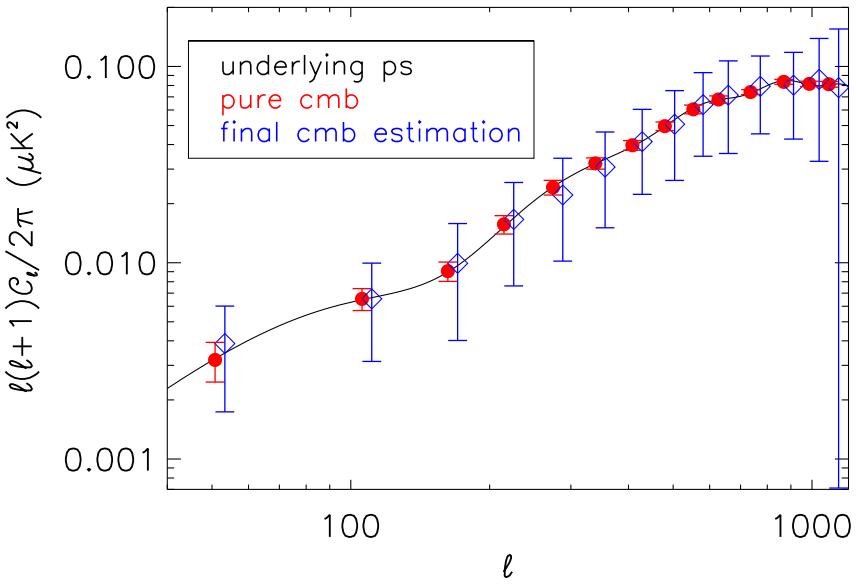

Figure 6.5: Demonstration of the validity of the extended algorithm by fixing the parameters related to the band shape uncertainty and the AHWP rotation effect. In-band power scaling coefficients and rotation angles are included in the calculation but are assumed to be perfectly known. The dust spectral index is the only parameter estimated by the algorithm. The estimated final CMB B-mode power spectrum (blue diamond) agrees with the input (red dot) and no bias is introduced. The error bars plotted are the standard deviation of 100 simulations in each ℓ bin. The solid black line is the theoretical CMB B-mode power spectrum assuming $r = 0.05$.

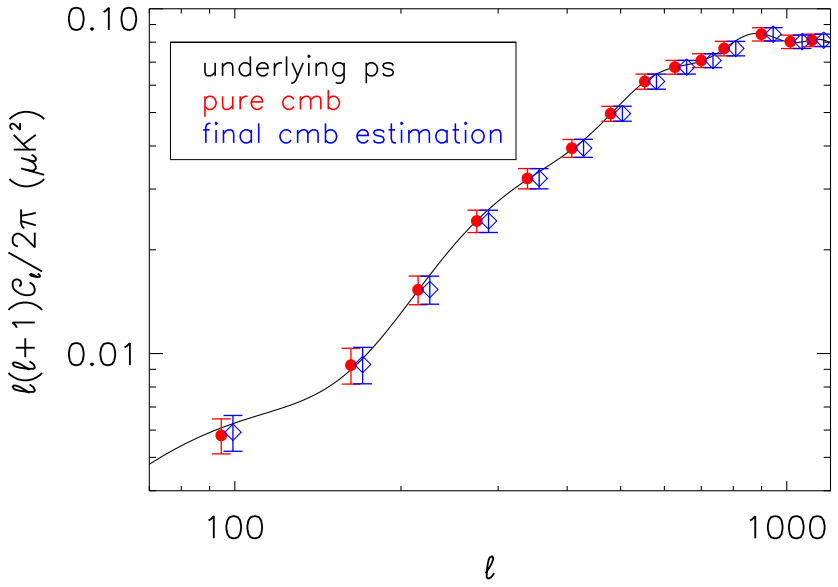

Figure 6.6: Noiseless simulation where the band-center of the 150 GHz band is shifted by 10 GHz and the 250 GHz and 410 GHz bands are perfectly known. The spectral index, scaling coefficient in 150 GHz bands for dust and CMB are recovered accurately. The estimated final CMB B-mode power spectrum (blue diamond) agrees with the input (red dot) and no bias is introduced.

band-center mismatch in 250 GHz or 410 GHz band, there is no bias in the estimated CMB B-mode power spectrum. We also run simulations where the band-width of each band is changed by 10 GHz and the algorithm recovers the input CMB B-mode signal without any bias.

With noise

After assuring there is no intrinsic bias caused by the algorithm, we move on to cases with nominal noise level stated in Table 6.1. First we address the cases where there is uncertainty in only one of the bands. We observe a degeneracy between dust spectral index and in-band dust scaling coefficient. This is the degeneracy mentioned in Sec. 6.1.2:

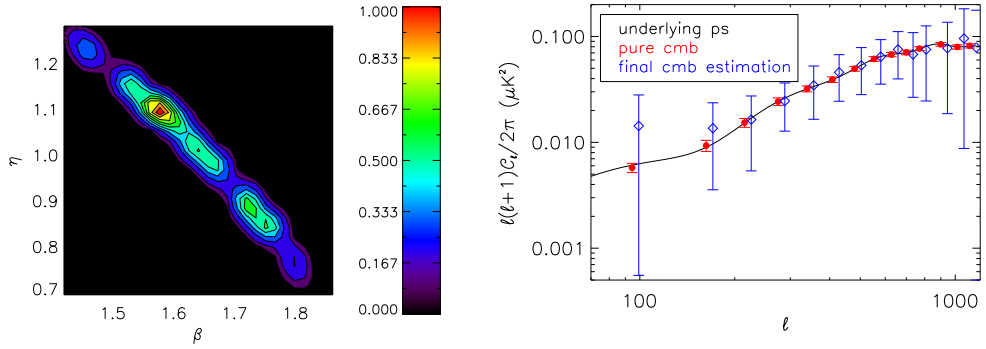

Figure 6.7: Degeneracy between spectral index and in-band dust scaling coefficient exists and it causes bias in the observed CMB B-mode power spectrum at low ℓ. Here the scaling coefficients at 250 GHz and 410 GHz bands are known perfectly. Only the two coefficients at 150 GHz are being optimized. Left: 2D likelihood plot between the dust spectral index β and the in-band dust scaling coefficient η_d at 150 GHz. The bright diagonal stripe in the 2D parameter space shows that points along the line give similar likelihood value and thus are degenerate. Right: Power spectrum of CMB B-mode. The extracted CMB signal (blue diamond) is biased at the two lowest ℓ-bins (15 and 4 times the cosmic variance away from the input CMB signal at the lowest and the second lowest ℓ bins, respectively) compared to the input (red dot).

when there is noise in the observation, changing the tilt of the dust spectrum or the scaling of the dust observation in one band give similar likelihood value. The degeneracy causes bias in the recovered CMB power spectrum, particularly in the low ℓ bin where the dust signal is high and the inflationary B-mode signal resides. Fig. 6.7 shows the 2D likelihood plot between the dust spectral index and the dust in-band scaling coefficient (left panel) and the recovered CMB B-mode power spectrum (right panel) of a simulation where there is uncertainty in the 150 GHz band. The bright diagonal feature in the 2D likelihood plot shows the correlation between the dust spectral index and the dust in-band scaling coefficient. The likelihood value along the line is similar thus the algorithm can not distinguish pairs of values along the line. When the parameters are mis-estimated, the estimated B-mode signal is biased by the residual dust signal at low ℓ.

In practice, the observation bands are measured to certain accuracy, which means we can set prior constraints to the band scaling coefficients according to the knowledge of the

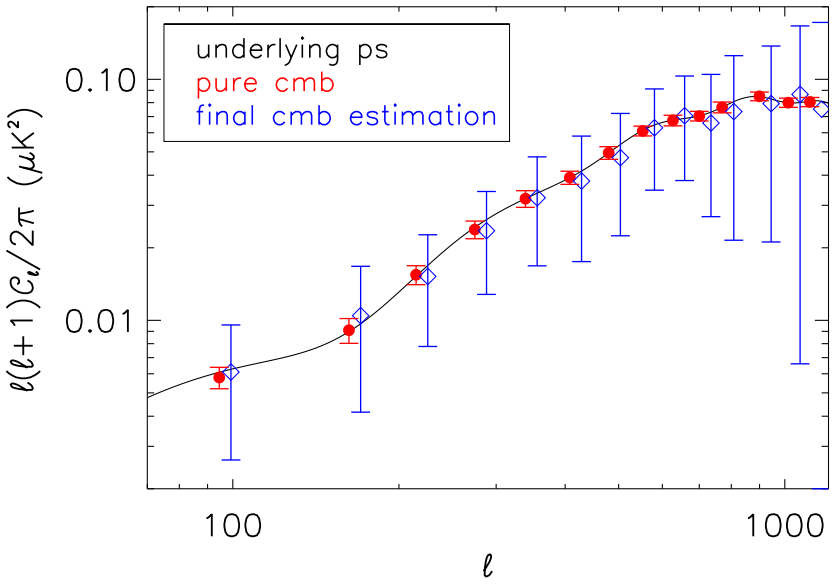

Figure 6.8: Simulated results with prior constraints on in-band scaling coefficients. Only coefficients at 150 GHz band are optimized in the algorithm here and the coefficients at 250 GHz and 410 GHz bands are assumed to be perfectly known. There is 15% prior constraints on the in-band scaling coefficients at 150 GHz band. The extracted CMB signal (blue diamond) agrees with the input (red dot).

frequency bands. By doing so, we are limiting the parameter space in which the algorithm searches for best fit values. When the prior constraint is sufficiently tight, we can lift the degeneracy and extract the parameters and sky signals properly. We first assess the case where only one band has uncertainty and generate a direct comparison to the simulation discussed above and show the effect of setting prior constraints. Fig. 6.8 shows the result where we set 15% Gaussian priors on the in-band scaling coefficients for both CMB and dust at 150 GHz band. Compared to the result in Fig. 6.7, Fig. 6.8 demonstrates that with mild prior constraints the algorithm can recover the CMB B-mode power spectrum accurately.

We then extend the simulation to cases where all three bands are only known to certain accuracy. Since changing the sky signal is equivalent to shifting the scaling coefficients in

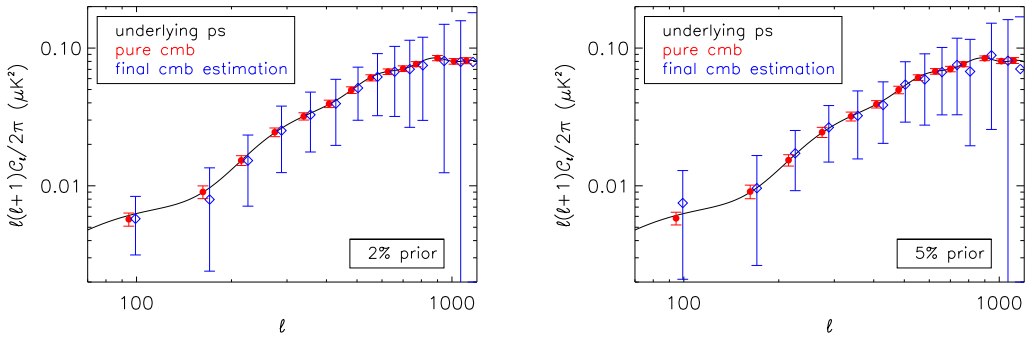

Figure 6.9: Simulation results where scaling coefficients for all three bands are allowed to vary with Gaussian prior constraints and are fitted by the algorithm. Left: 2% prior around the input value. Right: 5% prior around the input value. When there is a 2% prior the algorithm the extracted CMB B-mode signal (blue diamond) agrees with the input CMB signal (red dot). When the prior constraint is relaxed to 5%, the extracted B-mode signal at the lowest ℓ bin is biased at 2.7 times the cosmic variance away from the input value.

all three bands simultaneously by the same ratio, there exists degeneracy between the sky signal and the scaling coefficients. We need to set prior constraints on all scaling coefficients. In order to not introduce bias in the estimated CMB B-mode signal, the constraints here are more stringent than the one where only one band has uncertainty. When all in-band scaling coefficients have 2% Gaussian priors, the algorithm can recover the CMB B-mode signal accurately. When the prior constraints are relaxed to 5% for all scaling coefficients, the extracted CMB B-mode signal at the lowest ℓ bin is biased at 2.7 times the cosmic variance away from the input value. Fig. 6.9 shows the results of these two configurations.

It is worth pointing out that the prior requirement mainly come from dust scaling coefficients due to their degeneracy with the dust spectral index. Thus the excess bias in the final CMB B-mode estimation takes the power spectrum feature of the galactic dust, which has higher power at low ℓ. Given the designed EBEX top-hat bands, the corresponding band-center and band-width mismatches to a 2% or 5% dust scaling mismatch are shown in Table 6.2.

EBEX top-hat band mismatch	2% dust scaling mismatch		5% dust scaling mismatch	
	Band-center	Band-width	Band-center	Band-width
150 GHz	2 GHz	0.8 GHz	4.5 GHz	2 GHz
250 GHz	3 GHz	1.5 GHz	7.5 GHz	3.5 GHz
410 GHz	5 GHz	1.7 GHz	12 GHz	4.2 GHz

Table 6.2: The band-center and band-width mismatches correspond to a 2% or 5% dust scaling mismatch for the designed EBEX top-hat bands at 150 GHz, 250 GHz and 410 GHz.

On the other hand, given the measured EBEX frequency bands and their uncertainties in LDB flight configuration shown in Fig. 4.15, we can calculate the uncertainties on the in-band scaling coefficients for the CMB and dust sky signals by using Monte-Carlo simulations. The uncertainties of the scaling coefficients are 5%, 4%, 5% for CMB and 5%, 3%, 4% for dust in the 150 GHz, 250 GHz, 410 GHz bands, respectively. When using these uncertainties as the prior constraints of the corresponding scaling coefficients, the algorithm can extract the CMB B-mode signal without any bias. Fig. 6.10 shows the resulting power spectra from the simulation.

6.3.2 Frequency Dependent Rotation Effect

Here we assess the capability of the algorithm to estimate the CMB B-mode signal in the presence of frequency dependent polarization rotation effect. As an example, we use the rotation effect from the EBEX AHWP in the simulation. In the simulations here all the in-band scaling coefficients are assumed to be perfectly known and fixed at unity which is the input value.

No noise

We first assess the intrinsic bias induced by the algorithm in the final extracted CMB B-mode signal. The simulations in this analysis are performed in the absence of instrumental noise. Due to the degeneracy between the polarization angle of the incoming signal and the AHWP induced rotation mentioned in Sec. 6.1.2, we fit for the rotation angles in one band at a time while assuming the ones in the other two bands are perfectly known. Here we do not assume any prior knowledge of the rotation angle.

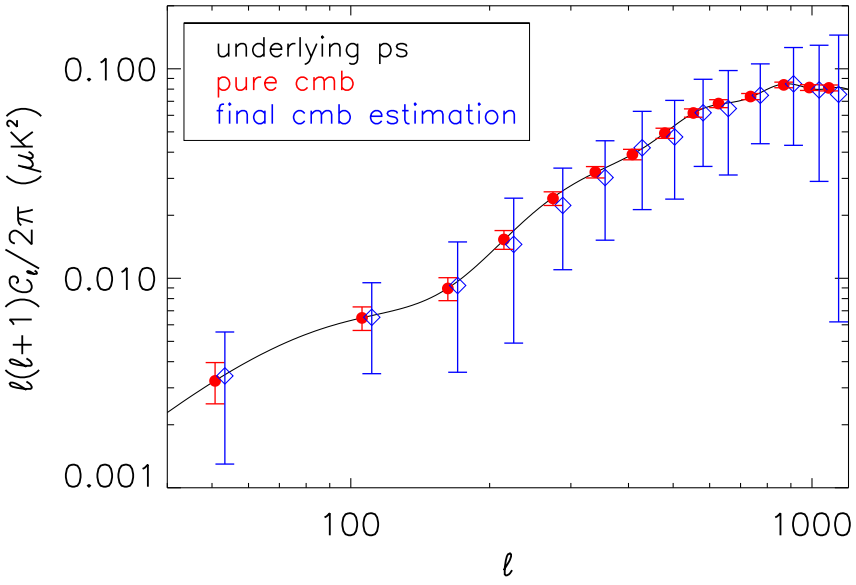

Figure 6.10: Results of simulation with LDB configuration prior constraints on in-band scaling coefficients. The band measurements are shown in Fig. 4.15. The uncertainty of the in-band scaling coefficients calculated from Monte-Carlo simulations are 5%, 4%, 5% for CMB and 5%, 3%, 4% for dust in the 150 GHz, 250 GHz, 410 GHz bands, respectively. The extracted CMB signal (blue diamond) is not biased compare to the input (red dot).

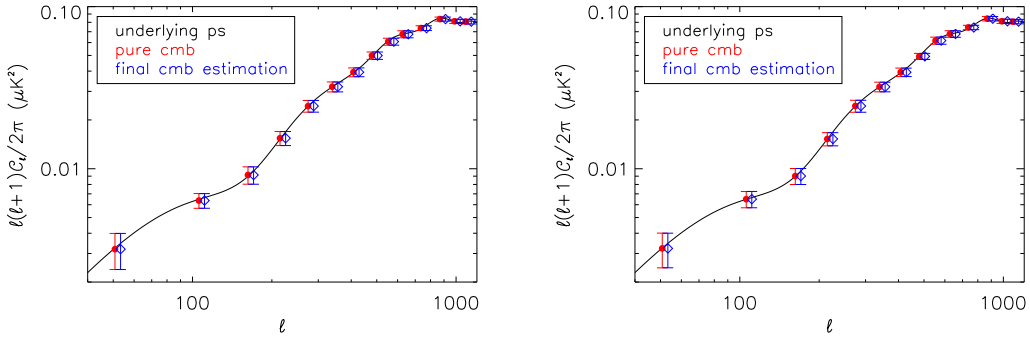

Figure 6.11: Noiseless simulation where rotation angles in 250 GHz and 410 GHz bands are fixed as the input value. The spectral index, rotation angles in 150 GHz band for dust and CMB are fitted and recovered accurately. No prior constraints are set on the parameters optimized by the algorithm. **Left**: the initial knowledge of the rotation angles is accurate; **Right**: the initial knowledge of the rotation angles is off by 10°. The estimated CMB B-mode power spectrum (blue diamond) in both cases agree with the input (red dot) and no bias is induced.

Fig. 6.11 shows the result when only the dust spectral index and the rotation angles in the 150 GHz band are fitted by the algorithm. The rotation angles in 250 GHz and 410 GHz bands are assumed to be perfectly known. The result shows that in the absence of noise, the algorithm can fit for the dust spectral index and rotation angles accurately and extract the CMB B-mode signal without any bias even when the initial knowledge of the rotation angles is off by 10°. We get the same results when only fitting for rotation angles in 250 GHz or 410 GHz band.

With noise

After checking that the extension to the algorithm does not cause any intrinsic bias, we proceed to introduce noise in the simulation. We use nominal EBEX noise level stated in Table 6.1 in the simulation. First we assess the situation where the rotation angles in only one frequency band have uncertainties and the rotation angles in the rest two bands are perfectly known. In this situation, there is no degeneracy between the parameters so no prior constraints need to be set for the rotation angles. Fig. 6.12 shows the results of

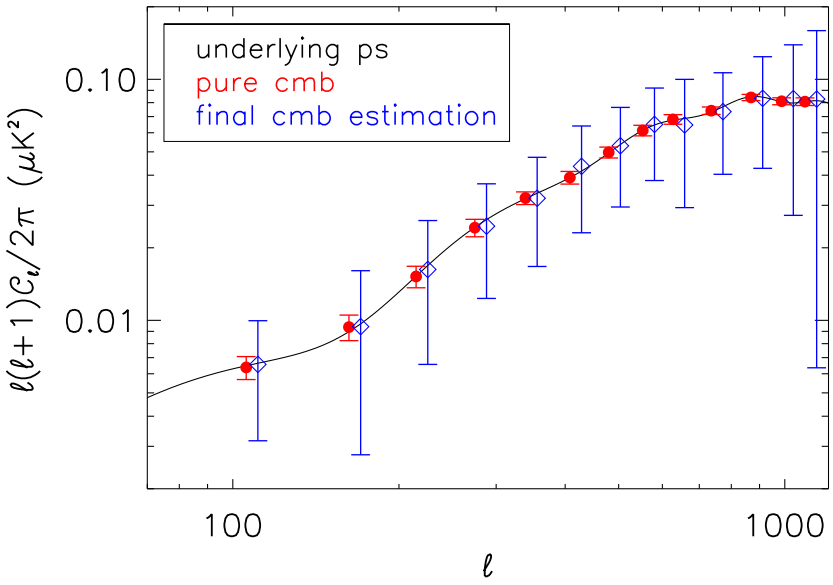

Figure 6.12: Simulation results where AHWP induced band averaged rotation angles for 150 GHz band are fitted by the algorithm. No prior constraints are set on the rotation angles at 150 GHz. All angles at 250 GHz and 410 GHz bands are assumed to be perfectly known. Nominal EBEX noise is included in the simulation. The extracted CMB B-mode signal (blue diamond) agrees with the input signal (red dot).

a simulation where the rotation angles at 150 GHz band are estimated by the algorithm while the rotation angles at 250 GHz and 410 GHz bands are assumed to be perfectly known. In this case, the algorithm can extract the CMB B-mode signal without any bias with nominal EBEX noise.

Next we allow the rotation angles in all three frequency bands for both the CMB and dust signals to be estimated by the algorithm. Due to the degeneracy between AHWP induced rotation and polarization angle of the incoming signal, the algorithm does not converge on the parameter values without prior constraints on the band averaged polarization rotation angles. In practice, the AHWP parameters and frequency bands are measured to certain accuracy. Thus the rotation angles can be predetermined within some range. Fig. 6.13 shows that with 4° Gaussian priors on all band averaged rotation angles, the final

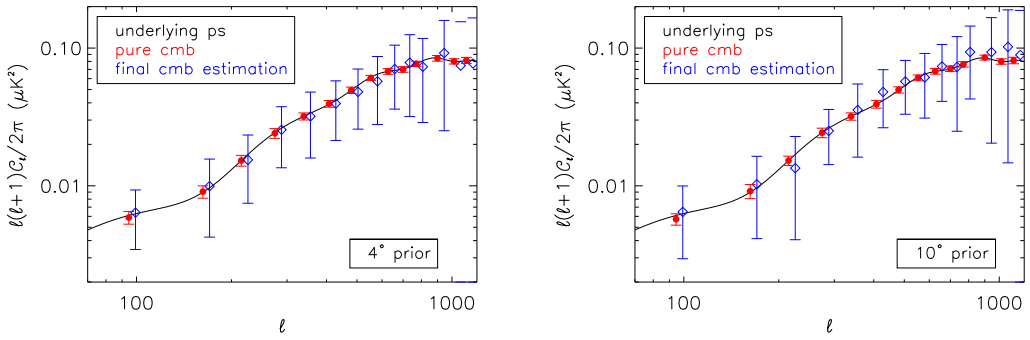

Figure 6.13: Simulation results where AHWP induced band averaged rotation angles for all three bands are fitted by the algorithm. All angles have Gaussian priors. Left: 4° for rotation angles. Right: 10° prior for rotation angles. When the prior is 4° the extracted the CMB B-mode signal (blue diamond) agrees with the input signal (red dot). When the prior constraint is 10°, there exists bias of more than 5 times the cosmic variance at some high ℓ bins due to the mixing of E-mode signal into B-mode signal.

estimated CMB B-mode signal is not biased. When the prior constraint is relaxed to 10° the extracted CMB B-mode signal in a few high ℓ bins are biased at more than 5 times the cosmic variance away from the input value. Since there is a degeneracy between the AHWP rotation angles and the incoming polarization angle, a less stringent prior constraint on the AHWP rotation results in a bigger uncertainty on the estimated polarization angle of the incoming signal. The inaccuracy of determining polarization angle causes leakage from CMB E-mode signal to B-mode signal which has a bigger effect at high ℓ bins.

Given the uncertainty of the band averaged IVA phase angles for the measured EBEX LDB bands in Sec. 4.2.6 and the ground polarization calibration results shown in Sec. 4.2.8, the rotation angles can be constrained to sub-degree level with calibration, which is within the 4° prior constraint set above. So the algorithm can extract CMB B-mode signal without bias given the accuracy of the knowledge of the instrument.

6.3.3 Combining Band Shape Uncertainty and Frequency Dependent Rotation Effect

In this section we show the results of simulations where both the band shape uncertainty and the frequency dependent rotation effect are present in the observation. In these simulations we assume uncertainties in the knowledge of both the observation bands and the AHWP characteristic parameters. Particularly, when there is mis-estimation of band parameters, even though the knowledge of AHWP is accurate, the band averaged rotation angles are mis-estimated as well. In this case, all in-band scaling coefficients and band averaged polarization rotation angles are estimated by the algorithm.

No noise

First we assess the capability of the algorithm to recover the input spectral parameters, instrumental parameters and the signals in the absence of noise. We assume top-hat band shapes for all frequency bands. In the simulations we vary one band at a time while keeping the other two bands fixed as the nominal input bands. When varying the bands, we either shift the band-center while keeping the band-width fixed or change the band-width while keeping the band-center fixed. Fig. 6.14 shows that when the 150 GHz band-center is mis-estimated by 15 GHz or the band-width is mis-estimated by 15 GHz, the algorithm can recover the actual band parameters and extract the CMB B-mode signal without any bias. We find that with a mis-estimation of 15 GHz of the band-center at 250 GHz or 410 GHz band, the algorithm can recover the CMB B-mode signal accurately. For the band-width, we find that with a mis-estimation of 15 GHz and 20 GHz at 250 GHz and 410 GHz band, respectively, the extracted CMB B-mode signal has no bias. Compared to the results in Sec. 5.4 we see that in the absence of noise this maximum likelihood method requires much less stringent accuracy of the band shape measurements compared to the simple method.

With noise

Next we add nominal EBEX noise to the input maps of the simulation and assess the capability of the algorithm to extract CMB B-mode signal. We start with the case where only the parameters at 150 GHz band is fitted by the algorithm while the ones at 250 GHz

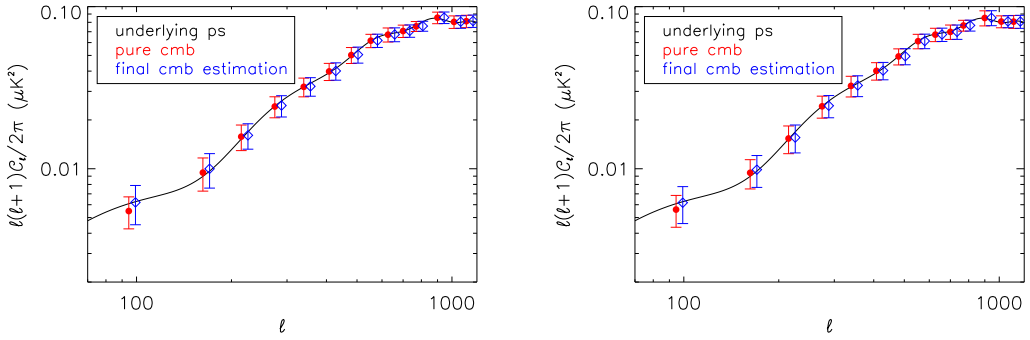

Figure 6.14: Simulation results where the in-band scaling coefficients and AHWP induced band averaged rotation angles for the 150 GHz band are fitted by the algorithm. The instrumental parameters for 250 GHz and 410 GHz bands are assumed to be perfectly known. The band-center of the 150 GHz band is mis-estimated by 15 GHz (left) or the band-width of the 150 GHz band is mis-estimated by 15 GHz (right). In both cases there is no bias of the extracted the CMB B-mode signal (blue diamond) compared to the input signal (red dot).

and 410 GHz are assume to be perfectly known. Due to the degeneracies mentioned in Sec. 6.1.2, we set a 15% Gaussian prior to the in-band scaling coefficients for CMB and dust at 150 GHz band. There is no prior constraints on the spectral index and the band averaged rotation angles. Fig. 6.15 shows that in this case the algorithm can correctly estimate the CMB B-mode signal without any bias.

Then we fit for the instrumental effects at all three bands. Due to the degeneracies, we set prior constraints to all of the parameters. For the priors, we use the uncertainties of the in-band scaling coefficients and the band averaged rotation angles of the measured EBEX bands in LDB configuration. These uncertainties are the standard deviation of the instrumental parameters calculated from 500 Monte-Carlo simulations. The priors are listed in Table 6.3. Fig. 6.16 shows the power spectra of the simulation. With the prior constraints, the foreground cleaning algorithm can recover the input CMB B-mode signal without introducing bias.

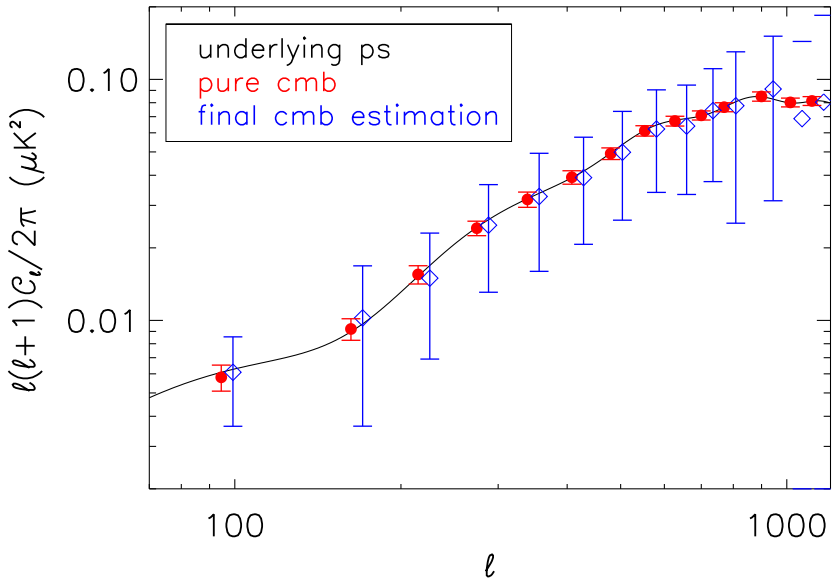

Figure 6.15: Simulation results where both the in-band scaling coefficients and the AHWP induced band averaged rotation angles for the 150 GHz band are fitted by the algorithm. There are 15% prior constraints on the in-band scaling coefficients and no prior constraints on the band-averaged rotation angles. All parameters at 250 GHz and 410 GHz bands are assumed to be perfectly known. Nominal noise is included in the simulation. There is no bias in the extracted the CMB B-mode signal (blue diamond) compares to the input signal (red dot).

Prior Constraints	150 GHz band	250 GHz band	410 GHz band
η_{CMB}	5%	4%	5%
η_{dust}	5%	3%	4%
θ_{CMB}	0.2°	0.02°	0.2°
θ_{dust}	0.2°	0.02°	0.2°

Table 6.3: Prior constraints of in-band scaling coefficients η and band averaged rotation angles θ for the three EBEX bands in LDB configuration. These values are the standard deviation of the instrumental parameters calculated from 100 Monte-Carlo simulations.

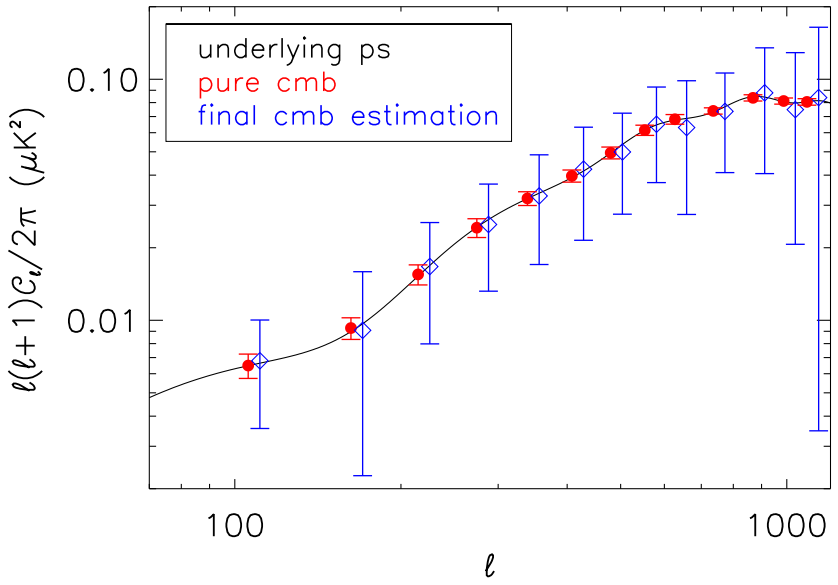

Figure 6.16: Simulation results where both the band shape uncertainty and the AHWP induced band averaged rotation angles for all three frequency bands are fitted by the algorithm. All instrumental parameters have prior constraints based on their uncertainty at the three EBEX LDB bands given by Monte-Carlo simulation, which are listed in Table 6.3. The extracted CMB B-mode signal (blue diamond) agree with the input signal (red dot) without any bias.

6.4 Discussion

Based on the most recent observation of galactic dust from Planck [27], galactic dust foreground is a dominant contaminating source in all regions on the sky for CMB polarimeters targeting the inflationary B-mode signal. The galactic dust signal needs to be removed and robust foreground cleaning is essential. In this chapter I present a maximum likelihood foreground removal algorithm particularly in the presence of two instrumental effects: band shape uncertainty and frequency dependent polarization rotation effect. This algorithm fits for the instrumental parameters simultaneously with the dust spectral index which allows for imperfect knowledge of the instrumental parameters. There exist various degeneracies: the degeneracy between the dust spectral index and the in-band scaling coefficients for dust, the degeneracy between the in-band scaling coefficients and the signals, and the degeneracy between the AHWP induced rotation angles and the incoming polarization angles of the signals. Due to the degeneracies, prior constraints need to be set on the instrumental parameters in order to not induce bias to the extracted CMB B-mode signal.

In the presence of both instrumental effects and the absence of noise, we vary the band-center or band-width of one band at a time. The designed EBEX top-hat bands are used as input in the simulation. The algorithm can recover the CMB B-mode signal without any bias when there is a band-center shift of 15 GHz, 15 GHz, 15 GHz and a band-width change of 15 GHz, 15 GHz , 20 GHz for 150 GHz, 250 GHz, 410 GHz band, respectively. Compared to the simple foreground cleaning method discussed in Chapter 5, the maximum likelihood foreground cleaning algorithm has less stringent requirement for the band measurement accuracy. The algorithm developed here also does not require accurate knowledge of the AHWP characteristic parameters compared to the simple method discussed in Chapter 5.

When nominal EBEX noise is present in the observation, we fit for both instrumental effects at all three frequency bands. There exists degeneracies between parameters and signals. With practical priors on parameters from calibration measurements, the algorithm can recover the CMB B-mode signal without any bias.

The foreground cleaning method developed here is applicable to CMB experiments other than EBEX as well. The band shape uncertainty is a common instrumental effect. The frequency dependent rotation effect is not unique to achromatic half-wave plate either. Sinuous antenna detectors [62], the novel detector technology which is going to be used in

next generation CMB polarimeters, have been reported to have the frequency dependent polarization rotation effect as well.

Chapter 7

Atmospheric Loading

One of the important inputs for the EBEX detector design is the atmospheric loading at balloon flight altitude. To maximize the sensitivity of the receiver, the thermal conductance of the detector has to be optimized. The thermal conductance is designed based on the expected total loading power of the detector. The atmospheric loading is the minimum optical loading power of the detectors. If the atmospheric loading is underestimated, the saturation power of the detector is less than the optical loading and the detectors are saturated during observation. If the atmospheric loading is overestimated, the electronic and Johnson noise rather than photon noise dominates the detector noise and the detector is less sensitive. EBEX is the first experiment to operate the transition edge sensor (TES) detector at balloon flight altitude. Without previous measurements, the atmospheric loading has to be derived through theoretical calculation and simulation. In this chapter, my work on predicting the atmospheric loading in the EBEX bands is presented.

7.1 Software packages to model the atmosphere

First we introduce the software packages used in this chapter to model the atmosphere. To cross check the results, two independent atmosphere modeling software packages are used: ATM package for ALMA (described in Sec. 7.1.1), *am* (described in Sec. 7.1.2). For extra cross check, EBEX collaborator G. Tucker also used the Atmospheric Transmission (AT) Software (described in Sec. 7.1.3) to produce atmosphere predictions. The results from

these software packages are compared in Sec. 7.1.4.

7.1.1 ATM package for ALMA

ATM for ALMA is a library based on Atmospheric Transmission at Microwave (ATM) model [63]. It calculates atmospheric opacity, phase, and radiative transfer. The main input parameters are: frequency range, frequency resolution, elevation angle, site altitude, site atmospheric pressure, site atmospheric temperature and precipitable water vapor (PWV). Although the software is originally developed for ground observation sites, it can compute the atmosphere property at balloon flight altitude by setting the site altitude of the observatory to balloon altitude. There exists tabulated atmospheric pressure and temperature data at high altitude for various location considered in this chapter. However, the precipitable water vapor is lack of direct measurement and has to be calculated.

The precipitable water vapor is defined as the depth of the atmospheric water vapor contained in a vertical column of unit cross-sectional area extending between two specified levels if condensed. If the mixing ratio of water is known, the PWV can be expressed as:

$$PWV = \frac{1}{g} \int_{p_1}^{p_2} x \, \mathrm{d}p. \tag{7.1}$$

Here g is the gravitational acceleration, x is the mixing ratio and p is the atmospheric pressure. At the balloon flight altitude (between 32 to 37 km) the gravitational acceleration is 9.69 m/s^2, the mixing ratio of water vapor above 25 km is 3.5×10^{-6} [64]. When calculating the PWV for certain altitude, the limit of the integral runs from 0 to the pressure at that altitude.

The output of the software includes opacity, transmission and effective temperature as a function of frequency. Specifically, we use the transmission data in this chapter for further atmospheric loading calculation. The transmission vs frequency curve contains two components: transmission line from molecules in the atmosphere and a continuum.

For ground observations considered in ATM package, absorption lines of H_2O, O_2, O_3 and other trace elements in the atmosphere are apparent at sub-millimeter ranges. For the flight altitude of EBEX, the H_2O content is small and the water lines are not dominant in the transmission curve. The main emission line contribution comes from O_2 and O_3. At

flight altitude, the collisional broadening mechanism (i.e. pressure broadening) dominates the line shape. In general the broadening is roughly 2-3 MHz/mBar [63] for most molecules. So in the case of flight altitude where the pressure is less than 10 mBar, the line width is less than 30 MHz.

In ATM, the continuum-like terms across the sub-millimeter range are also included. There are H_2O pseudo-continuum and dry pseudo-continuum. These two terms have different functional forms and the coefficients of the terms are fitted from previous measurements. At EBEX float altitude, water content is small and thus the dry continuum dominates. The expression of the dry continuum used in ATM [63] is

$$\kappa_{c,dry} = 2.612 \cdot 10^{-6} (\frac{p_d}{1013})^2 (\frac{300}{T})^{3.5} (\frac{\nu}{225})^2. \tag{7.2}$$

Here $\kappa_{c,dry}$ is the dry continuum absorption coefficient in unit of m^{-1}, p_d is the pressure of the dry component in unit of mBar, T is the temperature of the atmosphere in unit of K and ν is the frequency in unit of GHz. When substituting in the atmospheric parameters at balloon flight altitude, the continuum level is less than 10^{-6} within the EBEX frequency range.

7.1.2 *am*

am is a program to perform radiative transfer computations at microwave to sub-millimeter wavelengths, written by Scott Paine at Smithsonian Astrophysical Observatory [65]. *am* models the propagation paths as a sequence of planar layers. *am* includes thermal emission, absorption, and excess delay when calculating spectra. Although *am* are primarily used in radio astronomy and ground-based atmospheric radiometry, the program can also be used to calculate atmospheric loading for EBEX. *am* takes a configuration file as input. Such files contains the model propagation path described in several layers and other parameters controlling the model computation.

When defining each layers of the atmosphere, parameters such as pressure and temperature can be read directly or interpolated from tabulated values. Precipitable water vapor (PWV) is calculated from the water volume mixing ratio (VMR). As pointed out in an example *am* configuration file for a balloon launched from Alice Springs, the VMR can be

approximated as linear in log(Pressure) for 4 ppm at 100 mBar to 6 ppm at 1 mBar, and constant at 6 ppm for $P < 1$ mBar [66]. The PWV at each altitude can then be expressed as:

$$PWV \;=\; \sum_i \frac{VMR_i \times P(H_i) \times \Delta H_i \times \mu_{H_2O}}{\rho_{H_2O} \times R\, T(H_i)}, \tag{7.3}$$

where i runs through all the layers above the observation altitude, P denotes pressure, H denotes altitude, ΔH_i denotes thickness of each layer, μ denotes the molar mass, ρ denotes the density, R is the gas constant and T denotes the temperature. The PWV of the top layer is calculated with Eq. 7.3 assuming 6 ppm VMR. The PWV calculated from Eq. 7.3 is 10-20% larger than the ones calculated using Eq. 7.1.

7.1.3 AT – Atmospheric Transmission Software

As a separate cross check, EBEX collaborator G. Tucker used the Atmospheric Transmission software (AT) [67] to calculate atmospheric property independently. This software is a package used by the astronomical community to calculate atmospheric transmission at various sites. The input includes latitude, elevation and zenith angle. The Air Force Cambridge Research Laboratories (AFCRL) line catalog is used to create the transmission curve for the atmosphere. There are seven contributing molecules to the line catalog: H_2O, CO_2, O_3, CH_4, N_2O, CO, and O_2. The atmospheric profiles are based on [68] and user supplied local temperature and pressure data.

7.1.4 Comparison between different models

Here we compare the transmission vs frequency curves calculated by the three atmosphere modeling software packages. During the EBEX NA flight the gondola elevation is 15° and the average flight altitude is 34 km. So we choose the outputs from ATM, AT and *am* for north America atmosphere at 34 km altitude and 15° elevation as an example. The detailed atmospheric parameters are listed in Table 7.1.

Fig. 7.1 shows the atmosphere transmission as a function of frequency calculated by ATM, AT and *am* software packages. The locations of the spectral lines in the transmission spectra agree while the line depths of the spectrum differ. Table 7.2 lists the in band atmospheric loading power for the EBEX 150 GHz, 250 GHz and 410 GHz bands from the

Atmosphere Software	ATM	AT	*am*
Altitude (km)	34	34	34
Elevation	15°	15°	15°
Frequency Resolution (MHz)	10	10	10
Air pressure (mBar)	6.46	6.46	6.46
Air temperature (K)	234.25	222.97	242.36
PWV (μm)	0.233	0.258	0.126

Table 7.1: Atmospheric parameters used in ATM, AT and *am* for north America atmosphere at 34 km and 15° elevation.

Atmosphere Software	ATM	AT	*am*
Loading in 150 GHz band (pW)	0.093	0.111	0.098
Loading in 250 GHz band (pW)	0.96	1.15	0.99
Loading in 410 GHz band (pW)	4.83	4.63	4.32

Table 7.2: Atmospheric loading calculated by ATM, AT and *am* for north America atmosphere at 34 km and 15° elevation in the EBEX 150 GHz, 250 GHz and 410 GHz bands.

three software packages. The detail of the calculation is explained in Sec. 7.2.1. The loading powers agree within 20% among the calculations. Given the detector loading budget [37], 40% uncertainty in the atmosphere loading calculation induces less than 5% uncertainty in the total saturation power of the detectors.

7.2 Atmospheric loading calculation

In this section we present the calculation from the transmission vs frequency curve to in band atmospheric loading power for EBEX (Sec. 7.2.1). The transmission curve is calculated using the ATM software package unless otherwise noticed. We show the results for EBEX north America (NA) flight (Sec. 7.2.2), EBEX long duration balloon (LDB) flight (Sec. 7.2.3) and various ground sites (Sec. 7.2.4).

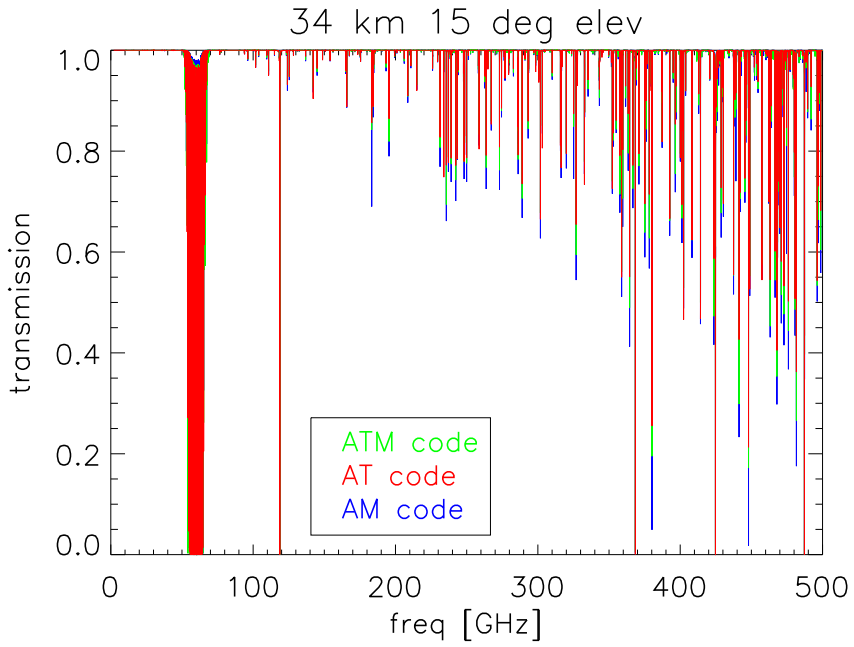

Figure 7.1: Comparison of atmospheric transmission spectra calculated by ATM, AT and *am* codes. We use parameters for north America atmosphere at 34 km altitude and 15 degree elevation as an example here. The parameters are listed in Table 7.1

7.2.1 From transmission curve to atmospheric loading power

Given the transmission of the atmosphere at a particular frequency and the air temperature, the intensity of the emission from the atmosphere can be calculated as

$$I(\nu) \;=\; B(\nu, T_{air}) \times (1 - t(\nu)). \tag{7.4}$$

Here $t(\nu)$ denotes the transmission output from the atmospheric software. $1 - t(\nu)$ is the absorption of the atmosphere. In equilibrium, the absorbed energy is re-emitted by the atmosphere. T_{air} is the air temperature, $B(\nu, T_{air})$ denotes the radiation spectrum of a black body at T_{air}. The intensity can also be expressed as antenna temperature using the Rayleigh-Jeans law

$$T_{ant}(\nu) \;=\; \frac{c^2[B(\nu, T_{air}) \times (1 - t(\nu))]}{2\nu^2 k_B}. \tag{7.5}$$

Here T_{ant} is the antenna temperature of the atmosphere, c is the speed of light and k_B is the Boltzmann constant.

The radiation flux from the atmosphere for a telescope can then be calculated as

$$f(\nu) \;=\; A\Omega \times I(\nu) \;=\; A\Omega \times B(\nu, T_{air}) \times (1 - t(\nu)), \tag{7.6}$$

where A is the surface area of the telescope mirror and Ω is the solid angle of the beam. Specifically, $A\Omega$ is the throughput of the telescope. For EBEX the throughput can be approximated as λ^2 where λ is the wavelength. So for EBEX the atmospheric emission flux as a function of frequency can be written as

$$f(\nu) \;=\; \lambda^2 \times B(\nu, T_{air}) \times (1 - t(\nu)), \tag{7.7}$$

To get the total in band atmospheric loading power p_{atm}, the flux $f(\nu)$ is integrated between the band edges

$$p_{atm} = \int_{\nu_L}^{\nu_U} f(\nu) d\nu, \tag{7.8}$$

where ν_L and ν_U are the lower and upper frequency edge of the observation band. In the case of simulation where the transmission is calculated numerically, a discrete summation of $f(\nu)\Delta\nu$ is performed rather than the integral.

Altitude (km)	Pressure (mBar)	Temperature (K)	PWV (μm)
32	8.68	228.65	0.314
33	7.48	231.45	0.270
34	6.46	234.25	0.233
35	5.59	237.05	0.202
36	4.84	239.85	0.175
37	4.20	242.65	0.152

Table 7.3: Atmospheric parameters for EBEX NA flight used in ATM software to calculate the atmosphere transmission as a function of frequency. Here the transmission is calculated from 10 GHz to 500 GHz with 10 MHz resolution.

It is worth pointing out that the atmospheric loading power calculated here is the value at the window of the instrument rather than at the detector. To get the detected power by the detectors at a frequency channel, the optical efficiency of the instrument and detector needs to be taken into account.

7.2.2 Atmospheric loading for EBEX north America flight

EBEX had an engineering test flight in north America (NA) in 2009. To calculated the atmospheric loading during EBEX NA flight, we use the air pressure and air temperature from the US standard atmosphere model [69] as input parameters for ATM. Table 7.3 lists the parameters for altitude between 32 km and 37 km at every 1 km interval. The precipitable water vapor is calculated using Eq. 7.1.

Since the elevation during NA flight went as low as 15°, we calculate the atmospheric loading at 15°, 30°, 45°, 60° and 90° elevation. As an example, in Fig. 7.2 and Fig. 7.3 we show the transmission and the antenna temperature of the atmosphere as a function of frequency at 34 km and 15° elevation.The low transmission band at ∼60 GHz is caused by O_2 absorption but it is out of the EBEX frequency range.

Given the atmospheric emission at each frequency, we calculate the in band atmospheric loading power for the EBEX 150 GHz, 250 GHz and 410 GHz band using Eq. 7.8 and Eq. 7.7. The band is assumed to have a top-hat shape. We use the designed EBEX band edges, which are [133 GHz,173 GHz], [217 GHz,288 GHz] and [366 GHz, 450 GHz] for 150 GHz, 250 GHz and 410 GHz bands, respectively. Fig. 7.4 shows the atmospheric loading as a

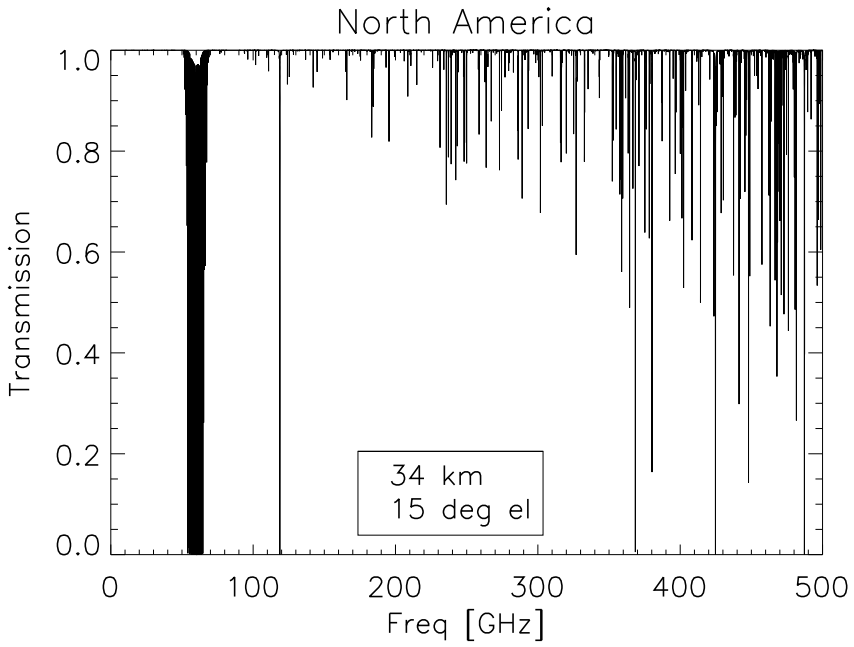

Figure 7.2: Transmission of the atmosphere as a function of frequency during EBEX NA flight. We use the US standard atmospheric model [69] at 34 km and 15° elevation here as an example.

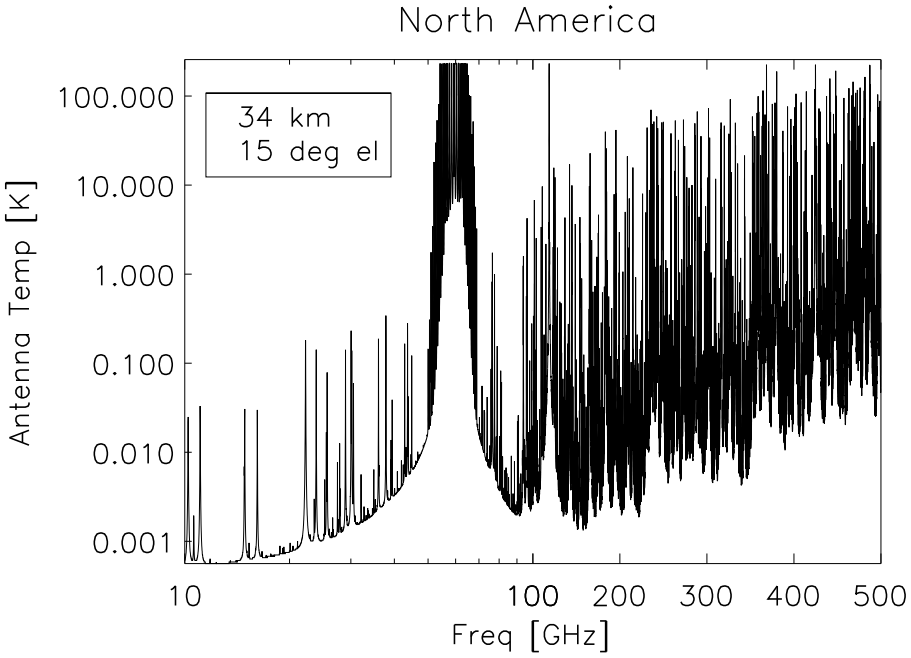

Figure 7.3: Emission of the atmosphere expressed in antenna temperature as a function of frequency during EBEX NA flight. Here we use the US standard atmospheric model [69] at 34 km and 15° elevation as an example.

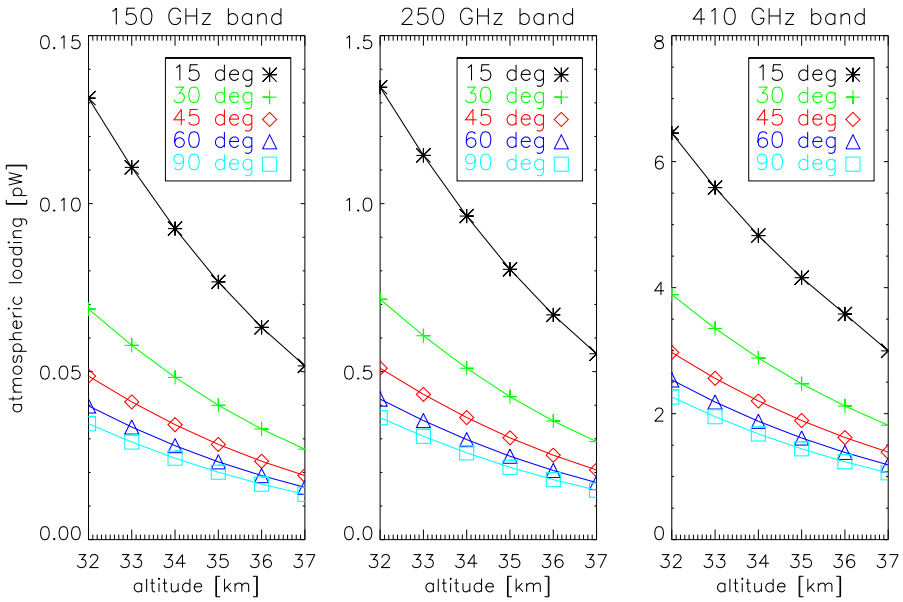

Figure 7.4: In band atmospheric loading as a function of altitude at 15°, 30°, 45°, 60° and 90° elevations for EBEX 150 GHz, 250 GHz and 410 GHz bands during NA flight. The atmospheric parameters used as input are listed in Table 7.3. The shape of the curves for the three bands are similar but the ranges of the y-axes have different orders of magnitude.

function of altitude at different elevation for the three bands. At 34 km altitude and 15° elevation, the atmospheric loading is 0.093 pW, 0.96 pW and 4.83 pW in the EBEX 150 GHz, 250 GHz and 410 GHz band, respectively.

In EBEX NA flight, the electronics on board from the Columbia Scientific Balloon Facility (CSBF) measured the pressure and temperature of the atmosphere throughout the flight. The measured values deviate from the US standard atmosphere value. Within a 15% pressure and a 20 K air temperature change the variation of the sky loading is less than 10%.

Altitude (km)	Pressure (mBar)	Temperature (K)	PWV (μm)
25	27.0	235.6	1.359
26	23.42	236.7	1.191
27	20.31	238.0	1.043
28	17.62	240.4	0.913
29	15.28	243.3	0.798
30	13.26	247.2	0.698
31	11.60	251.1	0.615
32	10.15	255.0	0.541
33	8.87	258.6	0.475
34	7.76	262.0	0.417
35	6.791	265.3	0.366
36	5.94	268.5	0.321

Table 7.4: Parameters from CIRA for Antarctica atmosphere used in the ATM software for EBEX LDB flight. Here the transmission is calculated from 10 GHz to 500 GHz with 10 MHz resolution.

7.2.3 Atmospheric loading for EBEX long duration balloon flight

Following the same procedure for NA flight, we calculate the atmospheric loading for EBEX 2012 LDB flight using the atmosphere transmission output from ATM. Table 7.4 lists the input atmosphere parameters for ATM, which are extrapolated from the mean January 80S latitude data in Cospar International Reference Atmosphere (CIRA-86) data[70]. The precipitable water vapor is calculated using Eq. 7.1.

For EBEX LDB flight, we calculate the atmospheric loading at 30°, 45°, 60° and 90° elevation. Fig. 7.5 and Fig. 7.6 show the transmission and antenna temperature of the atmosphere vs frequency at 34 km altitude and 30° elevation as an example. The curves have comparable amplitude and shape to the ones from the NA flight.

Given the atmospheric emission vs frequency curve, we use Eq. 7.8 and Eq. 7.7 to calculate the in band atmospheric loading power for the EBEX 150 GHz, 250 GHz and 410 GHz bands. In the calculation we assume designed EBEX top hat bands with band edges at [133 GHz, 173 GHz], [217 GHz, 288 GHz] and [366 GHz, 450 GHz]. Fig. 7.7 shows the atmospheric loading as a function of altitude at different elevation for the three bands. At 34 km altitude and 45° elevation, the atmospheric loading is 0.043 pW, 0.45 pW and 2.70

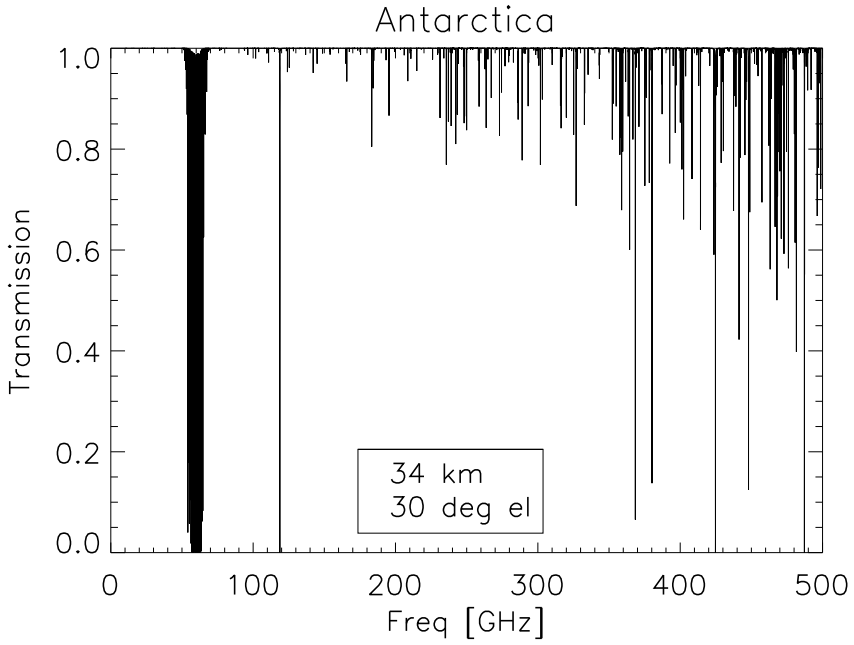

Figure 7.5: Transmission of the atmosphere as a function of frequency during EBEX LDB flight. Here we use the mean January 80S latitude data in CIRA [70] data at 34 km and 15° elevation as example parameters.

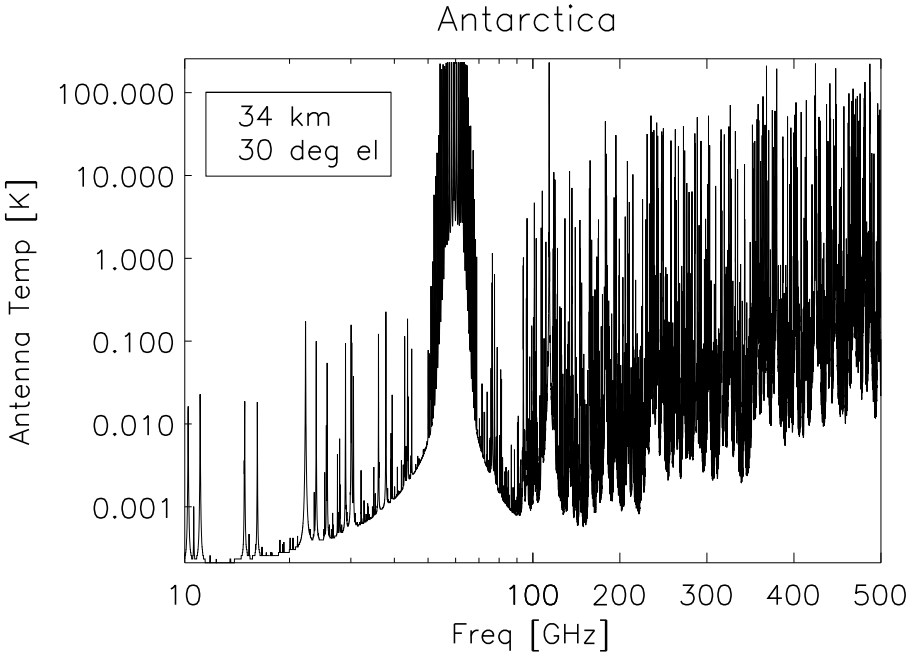

Figure 7.6: Emission of the atmosphere expressed in antenna temperature as a function of frequency during EBEX LDB flight. Here we use the mean January 80S latitude data in CIRA [70] data at 34 km and 15° elevation as example parameters.

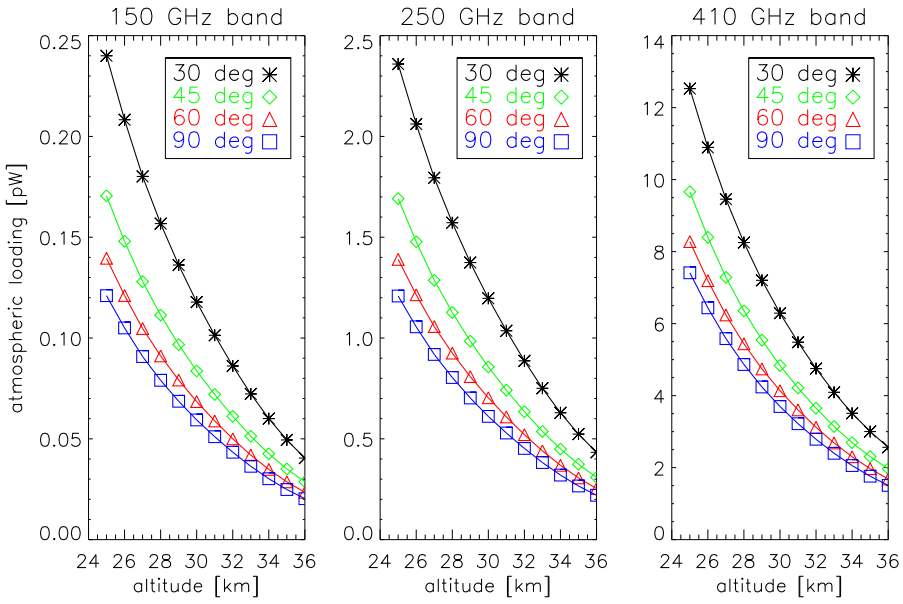

Figure 7.7: LDB in band atmospheric loading as a function of altitude for antarctic atmosphere at 30°, 45°, 60° and 90° elevations. Here we use the mean January 80S latitude data in CIRA [70] data at 34 km and 15° elevation as example parameters.

pW in the EBEX 150 GHz, 250 GHz and 410 GHz bands, respectively.

7.2.4 Atmospheric loading at ground observation sites

As a comparison, we also calculate the atmospheric loading for ground sites including the Atacama Large Millimeter/sub-millimeter Array (ALMA) site located on the Chajnantor plateau in northern Chile, the south pole and Palestine, TX. The ALMA site and the south pole are two of the best CMB observation site on the ground due to the altitude and dryness of the sites. Palestine is where EBEX had its integration field campaign before LDB flight in 2012. Table 7.5 lists the atmospheric parameters used for the three sites. The parameters for Palestine, TX are taken from the weather data in June because the EBEX integration campaign lasted from May to July in 2012.

Fig. 7.8 and Fig. 7.9 show the atmosphere transmission and antenna temperature of

Site	ALMA site	South pole	Palestine, TX
Altitude (km)	5	2.85	0.15
Air pressure (mBar)	560.0	691.0	996.1
Air temperature (K)	270.0	253.2	294.26
Water	PWV 1 mm	PWV 0.5 mm	71% humidity
Elevation	45°	45°	[15°,30°,45°,60°,75°,90°]

Table 7.5: Atmospheric parameters for ground sites including ALMA site, south pole and Palestine, TX. The water content is expressed in terms of precipitable water vapor (PWV) or relative humidity.

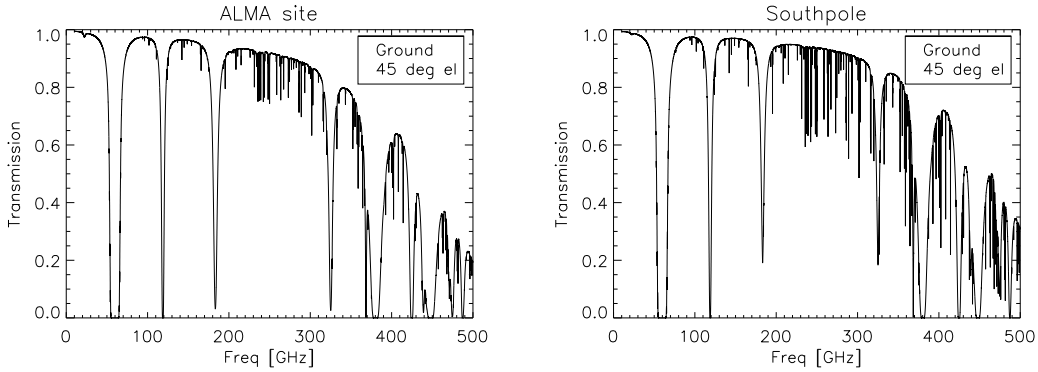

Figure 7.8: Atmosphere transmission as a function of frequency for ALMA site in northern Chile (left) and south pole (right) at 45° elevation. The transmission drops significantly beyond 300 GHz.

the atmospheric emission as a function of frequency for ALMA site and south pole at 45° elevation. Even as the two best CMB observation site on ground, these two sites do not have access to frequency ranges beyond 300 GHz. At 45° elevation, the atmospheric loading is 13.46, 47.62 and 417.43 pW at ALMA site and 10.30, 34.90 and 346.11 pW at south pole in the EBEX 150 GHz, 250 GHz and 410 GHz, respectively. Having access to higher frequency channels is an advantage of balloon CMB experiments compared to ground CMB experiments.

Fig. 7.10 shows the transmission and the antenna temperature of the atmosphere emission for Palestine, TX at various elevation angles. The relative humidity is set to be 71% which is toward the high end of the humidity at Palestine during the summer. The

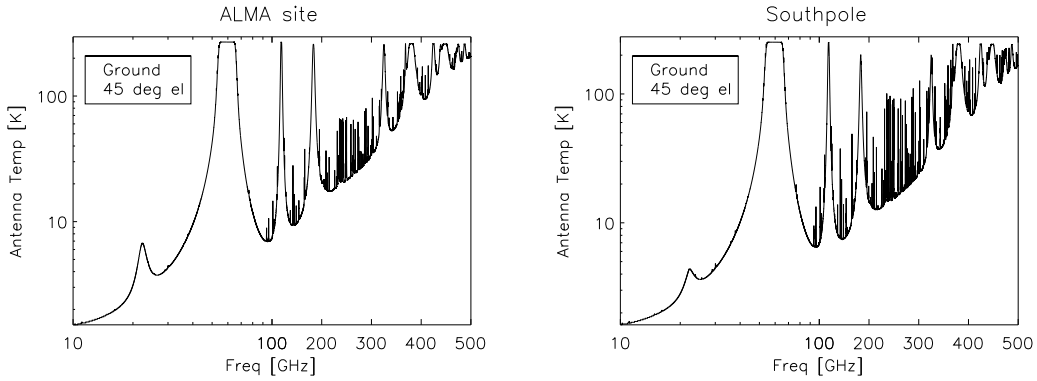

Figure 7.9: Emission of the atmosphere expressed in antenna temperature as a function of frequency for ALMA site in northern Chile (left) and south pole (right) at 45° elevation. Even as two of the best CMB observation site on the ground, the atmospheric emission antenna temperature is more than an order of magnitude higher than at balloon flight altitude.

atmosphere has less than 50% transmission beyond 150 GHz. Table 7.6 lists the in band atmospheric loading power for the three EBEX bands at each elevation angle. Compared to the LDB flight, the atmospheric loading on the ground is more than 2 orders of magnitude higher in all frequency bands.

Band	150	250	410
Frequency Range (GHz)	[133, 173]	[217, 288]	[366, 450]
Loading at 15° elevation (pW)	311.568	565.885	661.075
Loading at 30° elevation (pW)	274.471	561.055	661.075
Loading at 45° elevation (pW)	242.159	547.380	661.075
Loading at 60° elevation (pW)	220.653	531.997	661.074
Loading at 75° elevation (pW)	208.657	520.989	661.074
Loading at 90° elevation (pW)	204.816	517.081	661.074

Table 7.6: Atmospheric loading in unit of pW for Palestine, TX at 15°, 30°, 45°, 60°, 75° and 90° elevation. The atmosphere parameters are listed in Table 7.5.

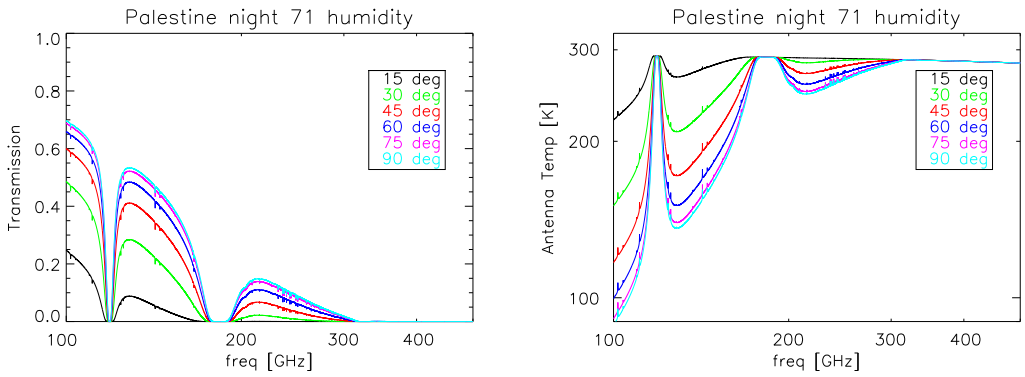

Figure 7.10: Emission of the atmosphere expressed in antenna temperature as a function of frequency for Palestine, TX at 15°, 30°, 45°, 60°, 75° and 90° elevation. The atmosphere has less than 70% transmission between 100 GHz and 500 GHz.

Chapter 8

Conclusion

The measurement of inflationary CMB B-mode polarization offers a unique probe to the physics of the extreme early universe. The inflationary CMB B-mode signal, however, is subject to contamination from the polarized galactic thermal dust emission foreground. In this work I presented two methods to remove foreground contamination particularly in the presence of the uncertainty of instrumental spectral response and frequency dependent polarization rotation effect. Although I focused on an example of the frequency dependent polarization rotation effect which is caused by an achromatic half-wave plate, the technique have a broad application to other systems with similar effect.

Based on simulations using parameters from the E and B experiment as inputs, I found that there exists some degeneracies among the instrumental parameters, the dust spectral parameters and the CMB and dust signals. With prior constraints on the parameters based on realistic measurements of EBEX instrument, the maximum likelihood foreground removal method can recover the inflationary B-mode signal without bias.

For future work I plan to apply the method to other ground and sub-orbital CMB polarimeter configurations with simulation. Eventually I would test this technique on real observation data and separate the galactic dust foreground contamination from the CMB B-mode signal.

References

[1] A. A. Penzias and R. W. Wilson. A Measurement of Excess Antenna Temperature at 4080 Mc/s. *Ap. J.*, 142:419–421, July 1965.

[2] Planck Collaboration, R. Adam, P. A. R. Ade, N. Aghanim, Y. Akrami, M. I. R. Alves, M. Arnaud, F. Arroja, J. Aumont, C. Baccigalupi, and et al. Planck 2015 results. I. Overview of products and scientific results. *ArXiv e-prints*, February 2015, 1502.01582.

[3] Planck Collaboration, P. A. R. Ade, N. Aghanim, M. Arnaud, M. Ashdown, J. Aumont, C. Baccigalupi, A. J. Banday, R. B. Barreiro, J. G. Bartlett, and et al. Planck 2015 results. XIII. Cosmological parameters. *ArXiv e-prints*, February 2015, 1502.01589.

[4] W. Hu and M. White. A CMB polarization primer. *New Astronomy*, 2:323–344, 1997. astro-ph/9706147.

[5] E. M. Leitch, J. M. Kovac, N. W. Halverson, J. E. Carlstrom, C. Pryke, and M. W. E. Smith. Degree Angular Scale Interferometer 3 Year Cosmic Microwave Background Polarization Results. *Ap. J.*, 624:10–20, May 2005, astro-ph/0409357.

[6] T. E. Montroy, P. A. R. Ade, J. J. Bock, J. R. Bond, J. Borrill, A. Boscaleri, P. Cabella, C. R. Contaldi, B. P. Crill, P. de Bernardis, G. De Gasperis, A. de Oliveira-Costa, G. De Troia, G. di Stefano, E. Hivon, A. H. Jaffe, T. S. Kisner, W. C. Jones, A. E. Lange, S. Masi, P. D. Mauskopf, C. J. MacTavish, A. Melchiorri, P. Natoli, C. B. Netterfield, E. Pascale, F. Piacentini, D. Pogosyan, G. Polenta, S. Prunet, S. Ricciardi, G. Romeo, J. E. Ruhl, P. Santini, M. Tegmark, M. Veneziani, and N. Vittorio. A

Measurement of the CMB EE Spectrum from the 2003 Flight of BOOMERANG. *Ap. J.*, 647:813–822, August 2006, astro-ph/0507514.

[7] J. H. P. Wu, J. Zuntz, M. E. Abroe, P. A. R. Ade, J. Bock, J. Borrill, J. Collins, S. Hanany, A. H. Jaffe, B. R. Johnson, T. Jones, A. T. Lee, T. Matsumura, B. Rabii, T. Renbarger, P. L. Richards, G. F. Smoot, R. Stompor, H. T. Tran, and C. D. Winant. MAXIPOL: Data Analysis and Results. *Ap. J.*, 665:55–66, August 2007, arXiv:astro-ph/0611392.

[8] J. L. Sievers, C. Achermann, J. R. Bond, L. Bronfman, R. Bustos, C. R. Contaldi, C. Dickinson, P. G. Ferreira, M. E. Jones, A. M. Lewis, B. S. Mason, J. May, S. T. Myers, N. Oyarce, S. Padin, T. J. Pearson, M. Pospieszalski, A. C. S. Readhead, R. Reeves, A. C. Taylor, and S. Torres. Implications of the Cosmic Background Imager Polarization Data. *Ap. J.*, 660:976–987, May 2007, astro-ph/0509203.

[9] C. Bischoff, L. Hyatt, J. J. McMahon, G. W. Nixon, D. Samtleben, K. M. Smith, K. Vanderlinde, D. Barkats, P. Farese, T. Gaier, J. O. Gundersen, M. M. Hedman, S. T. Staggs, B. Winstein, and CAPMAP Collaboration. New Measurements of Fine-Scale CMB Polarization Power Spectra from CAPMAP at Both 40 and 90 GHz. *Ap. J.*, 684:771–789, September 2008, 0802.0888.

[10] M. R. Nolta, J. Dunkley, R. S. Hill, G. Hinshaw, E. Komatsu, D. Larson, L. Page, D. N. Spergel, C. L. Bennett, B. Gold, N. Jarosik, N. Odegard, J. L. Weiland, E. Wollack, M. Halpern, A. Kogut, M. Limon, S. S. Meyer, G. S. Tucker, and E. L. Wright. Five-Year Wilkinson Microwave Anisotropy Probe Observations: Angular Power Spectra. *Ap. J. Suppl.*, 180:296–305, February 2009, 0803.0593.

[11] M. L. Brown, P. Ade, J. Bock, M. Bowden, G. Cahill, P. G. Castro, S. Church, T. Culverhouse, R. B. Friedman, K. Ganga, W. K. Gear, S. Gupta, J. Hinderks, J. Kovac, A. E. Lange, E. Leitch, S. J. Melhuish, Y. Memari, J. A. Murphy, A. Orlando, C. O'Sullivan, L. Piccirillo, C. Pryke, N. Rajguru, B. Rusholme, R. Schwarz, A. N. Taylor, K. L. Thompson, A. H. Turner, E. Y. S. Wu, M. Zemcov, and The QUa D collaboration. Improved Measurements of the Temperature and Polarization of the

Cosmic Microwave Background from QUaD. *Ap. J.*, 705:978–999, November 2009, 0906.1003.

[12] H. C. Chiang, P. A. R. Ade, D. Barkats, J. O. Battle, E. M. Bierman, J. J. Bock, C. D. Dowell, L. Duband, E. F. Hivon, W. L. Holzapfel, V. V. Hristov, W. C. Jones, B. G. Keating, J. M. Kovac, C. L. Kuo, A. E. Lange, E. M. Leitch, P. V. Mason, T. Matsumura, H. T. Nguyen, N. Ponthieu, C. Pryke, S. Richter, G. Rocha, C. Sheehy, Y. D. Takahashi, J. E. Tolan, and K. W. Yoon. Measurement of Cosmic Microwave Background Polarization Power Spectra from Two Years of BICEP Data. *Ap. J.*, 711:1123–1140, March 2010, 0906.1181.

[13] The POLARBEAR Collaboration, P. A. R. Ade, Y. Akiba, A. E. Anthony, K. Arnold, M. Atlas, D. Barron, D. Boettger, J. Borrill, S. Chapman, Y. Chinone, M. Dobbs, T. Elleflot, J. Errard, G. Fabbian, C. Feng, D. Flanigan, A. Gilbert, W. Grainger, N. W. Halverson, M. Hasegawa, K. Hattori, M. Hazumi, W. L. Holzapfel, Y. Hori, J. Howard, P. Hyland, Y. Inoue, G. C. Jaehnig, A. H. Jaffe, B. Keating, Z. Kermish, R. Keskitalo, T. Kisner, M. Le Jeune, A. T. Lee, E. M. Leitch, E. Linder, M. Lungu, F. Matsuda, T. Matsumura, X. Meng, N. J. Miller, H. Morii, S. Moyerman, M. J. Myers, M. Navaroli, H. Nishino, H. Paar, J. Peloton, D. Poletti, E. Quealy, G. Rebeiz, C. L. Reichardt, P. L. Richards, C. Ross, I. Schanning, D. E. Schenck, B. D. Sherwin, A. Shimizu, C. Shimmin, M. Shimon, P. Siritanasak, G. Smecher, H. Spieler, N. Stebor, B. Steinbach, R. Stompor, A. Suzuki, S. Takakura, T. Tomaru, B. Wilson, A. Yadav, and O. Zahn. A Measurement of the Cosmic Microwave Background B-Mode Polarization Power Spectrum at Sub-Degree Scales with POLARBEAR. *ArXiv e-prints*, March 2014, 1403.2369.

[14] S. Naess, M. Hasselfield, J. McMahon, M. D. Niemack, G. E. Addison, P. A. R. Ade, R. Allison, M. Amiri, N. Battaglia, J. A. Beall, F. de Bernardis, J. R. Bond, J. Britton, E. Calabrese, H.-m. Cho, K. Coughlin, D. Crichton, S. Das, R. Datta, M. J. Devlin, S. R. Dicker, J. Dunkley, R. Dünner, J. W. Fowler, A. E. Fox, P. Gallardo, E. Grace, M. Gralla, A. Hajian, M. Halpern, S. Henderson, J. C. Hill, G. C. Hilton, M. Hilton, A. D. Hincks, R. Hlozek, P. Ho, J. Hubmayr, K. M. Huffenberger, J. P. Hughes, L. Infante, K. Irwin, R. Jackson, S. Muya Kasanda, J. Klein, B. Koopman,

A. Kosowsky, D. Li, T. Louis, M. Lungu, M. Madhavacheril, T. A. Marriage, L. Maurin, F. Menanteau, K. Moodley, C. Munson, L. Newburgh, J. Nibarger, M. R. Nolta, L. A. Page, C. Pappas, B. Partridge, F. Rojas, B. L. Schmitt, N. Sehgal, B. D. Sherwin, J. Sievers, S. Simon, D. N. Spergel, S. T. Staggs, E. R. Switzer, R. Thornton, H. Trac, C. Tucker, M. Uehara, A. Van Engelen, J. T. Ward, and E. J. Wollack. The Atacama Cosmology Telescope: CMB polarization at $200 < l < 9000$. *JCAP*, 10:7, October 2014, 1405.5524.

[15] R. Keisler, S. Hoover, N. Harrington, J. W. Henning, P. A. R. Ade, K. A. Aird, J. E. Austermann, J. A. Beall, A. N. Bender, B. A. Benson, L. E. Bleem, J. E. Carlstrom, C. L. Chang, H. C. Chiang, H. Cho, R. Citron, T. M. Crawford, A. T. Crites, T. de Haan, M. A. Dobbs, W. Everett, J. Gallicchio, J. Gao, E. M. George, A. Gilbert, N. W. Halverson, D. Hanson, G. C. Hilton, G. P. Holder, W. L. Holzapfel, Z. Hou, J. D. Hrubes, N. Huang, J. Hubmayr, K. D. Irwin, L. Knox, A. T. Lee, E. M. Leitch, D. Li, D. Luong-Van, D. P. Marrone, J. J. McMahon, J. Mehl, S. S. Meyer, L. Mocanu, T. Natoli, J. P. Nibarger, V. Novosad, S. Padin, C. Pryke, C. L. Reichardt, J. E. Ruhl, B. R. Saliwanchik, J. T. Sayre, K. K. Schaffer, E. Shirokoff, G. Smecher, A. A. Stark, K. T. Story, C. Tucker, K. Vanderlinde, J. D. Vieira, G. Wang, N. Whitehorn, V. Yefremenko, and O. Zahn. Measurements of Sub-degree B-mode Polarization in the Cosmic Microwave Background from 100 Square Degrees of SPTpol Data. *ArXiv e-prints*, March 2015, 1503.02315.

[16] H. C. Ohanian and R. Ruffini. *Gravitation and Spacetime*. W. W. Norton & Company Ltd., 10 Coptic Street, London, WCA1 1PU, 1994.

[17] A. H. Guth. Inflationary universe: A possible solution to the horizon and flatness problems. *Phys. Rev. D.*, 23:347–356, January 1981.

[18] A. D. Linde. A New Inflationary Universe Scenario: A Possible Solution of the Horizon, Flatness, Homogeneity, Isotropy and Primordial Monopole Problems. *Phys. Lett.*, B108:389–393, 1982.

[19] A. A. Starobinsky. Dynamic of Phase Transition in the New Inflationary Universe Scenario and Generation of Perturbationss. *Phys. Lett.*, B117:175–178, 1982.

[20] A. A. Starobinskii. The Perturbation Spectrum Evolving from a Nonsingular Initially De-Sitter Cosmology and the Microwave Background Anisotropy. *Soviet Astronomy Letters*, 9:302–+, June 1983.

[21] V. A. Rubakov, M. V. Sazhin, and A. V. Veryaskin. Graviton creation in the inflationary universe and the grand unification scale. *Phys. Lett. B.*, 115:189–192, September 1982.

[22] L. P. Grishchuk. Amplification of gravitational waves in an istropic universe. *Sov. Phys. JETP*, 40:409–415, 1975.

[23] L. F. Abbott and M. B. Wise. Constraints on generalized inflationary cosmologies. *Nuclear Physics B*, 244:541–548, October 1984.

[24] M. Kamionkowski, A. Kosowsky, and A. Stebbins. Statistics of Cosmic Microwave Background Polarization. *Phys. Rev. D.*, 55:7368–7388, June 1997.

[25] U. Seljak and M. Zaldarriaga. Signature of Gravity Waves in the Polarization of the Microwave Background. *Phys. Rev. Lett.*, 78:2054–2057, March 1997. astro-ph/9609169.

[26] Planck Collaboration, P. A. R. Ade, N. Aghanim, D. Alina, M. I. R. Alves, C. Armitage-Caplan, M. Arnaud, D. Arzoumanian, M. Ashdown, F. Atrio-Barandela, and et al. Planck intermediate results. XIX. An overview of the polarized thermal emission from Galactic dust. *ArXiv e-prints*, May 2014, 1405.0871.

[27] Planck Collaboration, R. Adam, P. A. R. Ade, N. Aghanim, M. Arnaud, J. Aumont, C. Baccigalupi, A. J. Banday, R. B. Barreiro, J. G. Bartlett, and et al. Planck intermediate results. XXX. The angular power spectrum of polarized dust emission at intermediate and high Galactic latitudes. *ArXiv e-prints*, September 2014, 1409.5738.

[28] B. Gold, C. L. Bennett, R. S. Hill, G. Hinshaw, N. Odegard, L. Page, D. N. Spergel, J. L. Weiland, J. Dunkley, M. Halpern, N. Jarosik, A. Kogut, E. Komatsu, D. Larson, S. S. Meyer, M. R. Nolta, E. Wollack, and E. L. Wright. Five-Year Wilkinson Microwave Anisotropy Probe Observations: Galactic Foreground Emission. *Ap. J. Suppl.*, 180:265–282, February 2009, 0803.0715.

[29] L. Page, G. Hinshaw, E. Komatsu, M. R. Nolta, D. N. Spergel, C. L. Bennett, C. Barnes, R. Bean, O. Doré, J. Dunkley, M. Halpern, R. S. Hill, N. Jarosik, A. Kogut, M. Limon, S. S. Meyer, N. Odegard, H. V. Peiris, G. S. Tucker, L. Verde, J. L. Weiland, E. Wollack, and E. L. Wright. Three-Year Wilkinson Microwave Anisotropy Probe (WMAP) Observations: Polarization Analysis. *Ap. J. Suppl.*, 170:335–376, June 2007, arXiv:astro-ph/0603450.

[30] A. A. Fraisse, P. A. R. Ade, M. Amiri, S. J. Benton, J. J. Bock, J. R. Bond, J. A. Bonetti, S. Bryan, B. Burger, H. C. Chiang, C. N. Clark, C. R. Contaldi, B. P. Crill, G. Davis, O. Doré, M. Farhang, J. P. Filippini, L. M. Fissel, N. N. Gandilo, S. Golwala, J. E. Gudmundsson, M. Hasselfield, G. Hilton, W. Holmes, V. V. Hristov, K. Irwin, W. C. Jones, C. L. Kuo, C. J. MacTavish, P. V. Mason, T. E. Montroy, T. A. Morford, C. B. Netterfield, D. T. O'Dea, A. S. Rahlin, C. Reintsema, J. E. Ruhl, M. C. Runyan, M. A. Schenker, J. A. Shariff, J. D. Soler, A. Trangsrud, C. Tucker, R. S. Tucker, A. D. Turner, and D. Wiebe. SPIDER: probing the early Universe with a suborbital polarimeter. *JCAP*, 4:47, April 2013, 1106.3087.

[31] D. P. Finkbeiner, M. Davis, and D. J. Schlegel. Extrapolation of Galactic Dust Emission at 100 Microns to Cosmic Microwave Background Radiation Frequencies Using FIRAS. *Ap. J.*, 524:867–886, October 1999, arXiv:astro-ph/9905128.

[32] A. M. Meisner and D. P. Finkbeiner. Modeling Thermal Dust Emission with Two Components: Application to the Planck High Frequency Instrument Maps. *Ap. J.*, 798:88, January 2015, 1410.7523.

[33] B. Reichborn-Kjennerud. *Building and flying the E and B Experiment to measure the polarization of the cosmic microwave background.* PhD thesis, Columbia University, November 2010.

[34] K. T. Zilic. *Calibration and Design of the E and B EXperiment (EBEX) Cryogenic Receiver.* PhD thesis, University of Minnesota, 2014.

[35] J. M. Klein. *Design, Implementation, and Calibration of Half-Wave Plate Polarimetry for the E and B Experiment.* PhD thesis, University of Minnesota, 2014.

[36] J. Hubmayr. *Bolometric detectors for EBEX: A balloon-borne cosmic microwave background polarimeter*. PhD thesis, University of Minnesota, 2009.

[37] F. Aubin. *Detector readout electronics for EBEX : a balloon-borne cosmic microwave background polarimeters*. PhD thesis, McGill University, 2012.

[38] J. Bock, S. Church, M. Devlin, G. Hinshaw, A. Lange, A. Lee, L. Page, B. Partridge, J. Ruhl, M. Tegmark, P. Timbie, R. Weiss, B. Winstein, and M. Zaldarriaga. Task Force on Cosmic Microwave Background Research, April 2006, arXiv:astro-ph/0604101.

[39] B. Reichborn-Kjennerud, A. M. Aboobaker, P. Ade, F. Aubin, C. Baccigalupi, C. Bao, J. Borrill, C. Cantalupo, D. Chapman, J. Didier, M. Dobbs, J. Grain, W. Grainger, S. Hanany, S. Hillbrand, J. Hubmayr, A. Jaffe, B. Johnson, T. Jones, T. Kisner, J. Klein, A. Korotkov, S. Leach, A. Lee, L. Levinson, M. Limon, K. MacDermid, T. Matsumura, X. Meng, A. Miller, M. Milligan, E. Pascale, D. Polsgrove, N. Ponthieu, K. Raach, I. Sagiv, G. Smecher, F. Stivoli, R. Stompor, H. Tran, M. Tristram, G. S. Tucker, Y. Vinokurov, A. Yadav, M. Zaldarriaga, and K. Zilic. EBEX: a balloon-borne CMB polarization experiment. In *Society of Photo-Optical Instrumentation Engineers (SPIE) Conference Series*, volume 7741 of *Society of Photo-Optical Instrumentation Engineers (SPIE) Conference Series*, July 2010, 1007.3672.

[40] K. Arnold, P. A. R. Ade, A. E. Anthony, F. Aubin, D. Boettger, J. Borrill, C. Cantalupo, M. A. Dobbs, J. Errard, D. Flanigan, A. Ghribi, N. Halverson, M. Hazumi, W. L. Holzapfel, J. Howard, P. Hyland, A. Jaffe, B. Keating, T. Kisner, Z. Kermish, A. T. Lee, E. Linder, M. Lungu, T. Matsumura, N. Miller, X. Meng, M. Myers, H. Nishino, R. O'Brient, D. O'Dea, C. Reichardt, I. Schanning, A. Shimizu, C. Shimmin, M. Shimon, H. Spieler, B. Steinbach, R. Stompor, A. Suzuki, T. Tomaru, H. T. Tran, C. Tucker, E. Quealy, P. L. Richards, and O. Zahn. The POLARBEAR CMB polarization experiment. In *Society of Photo-Optical Instrumentation Engineers (SPIE) Conference Series*, volume 7741 of *Society of Photo-Optical Instrumentation Engineers (SPIE) Conference Series*, July 2010.

[41] Tomotake Matsumura, Shaul Hanany, Peter Ade, Bradley R. Johnson, Terry J. Jones, Prashanth Jonnalagadda, and Giorgio Savini. Performance of three- and five-stack achromatic half-wave plates at millimeter wavelengths. *Appl. Opt.*, 48(19):3614–3625, Jul 2009.

[42] G. Savini, G. Pisano, and P. A. R. Ade. Achromatic half-wave plate for submillimeter instruments in cosmic microwave background astronomy: modeling and simulation. *Appl. Optics*, 45:8907–8915, December 2006.

[43] L. Moncelsi, P. A. R. Ade, F. E. Angilè, S. J. Benton, M. J. Devlin, L. M. Fissel, N. N. Gandilo, J. O. Gundersen, T. G. Matthews, C. B. Netterfield, G. Novak, D. Nutter, E. Pascale, F. Poidevin, G. Savini, D. Scott, J. D. Soler, L. D. Spencer, M. D. P. Truch, G. S. Tucker, and J. Zhang. Empirical modelling of the BLASTPol achromatic half-wave plate for precision submillimetre polarimetry. *MNRAS*, 437:2772–2789, January 2014, 1208.4866.

[44] C. Bao, B. Gold, C. Baccigalupi, J. Didier, S. Hanany, A. Jaffe, B. Johnson, S. Leach, T. Matsumura, A. Miller, and D. O'Dea. The impact of the spectral response of an achromatic half-wave plate on the measurement of cosmic microwave background polarization. *Ap. J.*, 747:97, 2012. astro-ph/1112.3057.

[45] T. Matsumura. *A cosmic microwave background radiation polarimeter using superconducting magnetic bearings*. PhD thesis, University of Minnesota, Minnesota, USA, 2006.

[46] S. Pancharatnam. Achromatic combinations of birefringent plates part ii. an achromatic quarter-wave plate. *Proceedings of the Indian Academy of Sciences, Section A*, 41:137–144, 1955.

[47] E. V. Loewenstein, D. R. Smith, and R. L. Morgan. Optical constants of far infrared materials. 2: Crystalline solids. *Appl. Optics*, 12:398–+, February 1973.

[48] M. N. Afsar and H. Chi. Millimeter Wave Complex Refractive Index and Dielectric Permittivity Measurements of Crystalline Sapphire between 4 and 300 K. In *Society*

of Photo-Optical Instrumentation Engineers (SPIE) Conference Series, 16th International Conference on Infrared and Millimeter Waves, 1991. ISBN 0-8194-0707-0, M. R. Siegrist, M. Q. Tran and T. M. Tran, Lausanne, Switzerland, Aug 26-30, 1991.

[49] B. R. Johnson. *MAXIPOL: a bolometric, balloon-borne experiment for measuring the polarization anisotropy of the cosmic microwave background radiation.* PhD thesis, University of Minnesota/Twin Cities, 2004.

[50] M. N. Afsar. Precision millimeter-wave dielectric measurements of birefringent crystalline sapphire and ceramic alumina. *IEEE Transactions on Instrumentation Measurement*, 36:554–559, June 1987.

[51] M. C. Runyan, P. A. R. Ade, R. S. Bhatia, J. J. Bock, M. D. Daub, J. H. Goldstein, C. V. Haynes, W. L. Holzapfel, C. L. Kuo, A. E. Lange, J. Leong, M. Lueker, M. Newcomb, J. B. Peterson, C. Reichardt, J. Ruhl, G. Sirbi, E. Torbet, C. Tucker, A. D. Turner, and D. Woolsey. ACBAR: The Arcminute Cosmology Bolometer Array Receiver. *Ap. J. Suppl.*, 149:265–287, December 2003, astro-ph/0303515.

[52] Planck Collaboration, P. A. R. Ade, M. I. R. Alves, G. Aniano, C. Armitage-Caplan, M. Arnaud, F. Atrio-Barandela, J. Aumont, C. Baccigalupi, A. J. Banday, and et al. Planck intermediate results. XXII. Frequency dependence of thermal emission from Galactic dust in intensity and polarization. *Astron. Astrophys., submitted*, 2014, arXiv:1405.0874.

[53] A. Lewis, A. Challinor, and A. Lasenby. Efficient Computation of Cosmic Microwave Background Anisotropies in Closed Friedmann-Robertson-Walker Models. *Ap. J.*, 538:473–476, August 2000, arXiv:astro-ph/9911177.

[54] E. Komatsu, K. M. Smith, J. Dunkley, C. L. Bennett, B. Gold, G. Hinshaw, N. Jarosik, D. Larson, M. R. Nolta, L. Page, D. N. Spergel, M. Halpern, R. S. Hill, A. Kogut, M. Limon, S. S. Meyer, N. Odegard, G. S. Tucker, J. L. Weiland, E. Wollack, and E. L. Wright. Seven-year Wilkinson Microwave Anisotropy Probe (WMAP) Observations: Cosmological Interpretation. *Ap. J. Suppl.*, 192:18–+, February 2011, 1001.4538.

[55] F. Stivoli, J. Grain, S. M. Leach, M. Tristram, C. Baccigalupi, and R. Stompor. Maximum likelihood, parametric component separation and CMB B-mode detection in suborbital experiments. *MNRAS*, 408:2319–2335, November 2010, 1004.4756.

[56] Planck Collaboration, P. A. R. Ade, N. Aghanim, M. Arnaud, M. Ashdown, J. Aumont, C. Baccigalupi, A. Balbi, A. J. Banday, R. B. Barreiro, and et al. Planck early results. XIX. All-sky temperature and dust optical depth from Planck and IRAS. Constraints on the "dark gas" in our Galaxy. *Astron. Astrophys.*, 536:A19, December 2011, 1101.2029.

[57] G. Giardino, A. J. Banday, K. M. Górski, K. Bennett, J. L. Jonas, and J. Tauber. Towards a model of full-sky galactic synchrotron intensity and linear polarisation: A re-analysis of the Parkes data. *Astron. Astrophys.*, 387:82–97, May 2002.

[58] N. Kaiser. Weak gravitational lensing of distant galaxies. *Ap. J.*, 388:272–286, April 1992.

[59] D. E. Polsgrove. *Calibration of the E and B EXperiment (EBEX), a balloon-borne cosmic microwave background polarimeter*. PhD thesis, University of Minnesota, 2009.

[60] R. C. O'Brient. *A Log-Periodic Focal-Plane Architecture for Cosmic Microwave Background Polarimetry*. PhD thesis, University of California Berkeley, 2010.

[61] R. Stompor, S. Leach, F. Stivoli, and C. Baccigalupi. Maximum likelihood algorithm for parametric component separation in cosmic microwave background experiments. *MNRAS*, 392:216–232, January 2009, 0804.2645.

[62] R. O'Brient, J. Edwards, K. Arnold, G. Engargiola, W. Holzapfel, A. T. Lee, M. Myers, E. Quealy, G. Rebeiz, P. Richards, H. Spieler, and H. Tran. Sinuous antennas for cosmic microwave background polarimetry. In *Society of Photo-Optical Instrumentation Engineers (SPIE) Conference Series*, volume 7020 of *Presented at the Society of Photo-Optical Instrumentation Engineers (SPIE) Conference*, August 2008.

[63] J. R. Pardo, J. Cernicharo, and E. Serabyn. Atmospheric transmission at microwaves (ATM): an improved model for millimeter/submillimeter applications. *IEEE Transactions on Antennas and Propagation*, 49:1683–1694, December 2001.

[64] R. Zander. Water vapor above 25 km altitude. *Pure and Applied Geophysics*, 106:1346–1351, December 1973.

[65] S. Paine. The am atmospheric model, 2011. SMA technical memo No.152 version 7.2.

[66] K. H. Rosenlof, A. F. Tuck, K. K. Kelly, J. M. Russell, and M. P. McCormick. Hemispheric asymmetries in water vapor and inferences about transport in the lower stratosphere. *Journal of Geophysical Research*, 102:13213, June 1997.

[67] E. Grossman. Atmospheric transmission software user's manual, version 1.5, 1989. Airhead Software Co., Boulder, CO.

[68] USWB NASA, USAF. U.s. standard atmospheres and supplements, 1962 and 1966. U.S. Governemnt Printing Office, Washington D.C.

[69] National Geophysical Data Center. U.s. standard atmosphere (1976). *Planetary and Space Science*, 40:553–554, April 1992.

[70] Committee on Space Research; NASA National Space Science Data Center (2006): Global Climatology of Atmospheric Parameters from the Committee on Space Research (COSPAR) International Reference Atmosphere (CIRA-86) Project. NCAS British Atmospheric Data Centre. Global climatology of atmospheric parameters from the committee on space research (cospar) international reference atmosphere (cira-86) project. http://catalogue.ceda.ac.uk/uuid/4996e5b2f53ce0b1f2072adadaeda262, 2006.

Appendix A

AHWP Simulation for EBEX Bands in Ground Calibration Configuration

In this appendix I present the calculation of the band averaged IVA phase offset for the EBEX bands in the ground calibration configuration. During the EBEX 2012 Palestine ground calibration campaign, the instrument had a different set of filters compared to the long duration balloon (LDB) flight. This results in slightly different shapes of the three EBEX bands. Fig. A.1 shows the frequency band shapes in the ground calibration configuration. The detailed analysis to derive these bands from the measurements is presented in former Cosmolab member K. Zilic's thesis [34].

Table A.1 lists the equivalent top-hat band-centers and band-widths derived from the measurements for all three EBEX bands. Given the error bars of the data points, Zilic used Monte Carlo simulation to calculate the uncertainties of the band parameters, which are also listed in Table A.1.

During the ground calibration the EBEX AHWP is operated at cryogenic temperature. For the results presented here we use the best fit EBEX AHWP parameters at cryogenic temperature, which are listed in Table 4.4. In Table A.2 we list the band averaged IVA phase offsets $\langle\phi\rangle$ and their uncertainties for different incoming signal spectra for the three measured EBEX bands in the ground calibration configuration. We include CMB

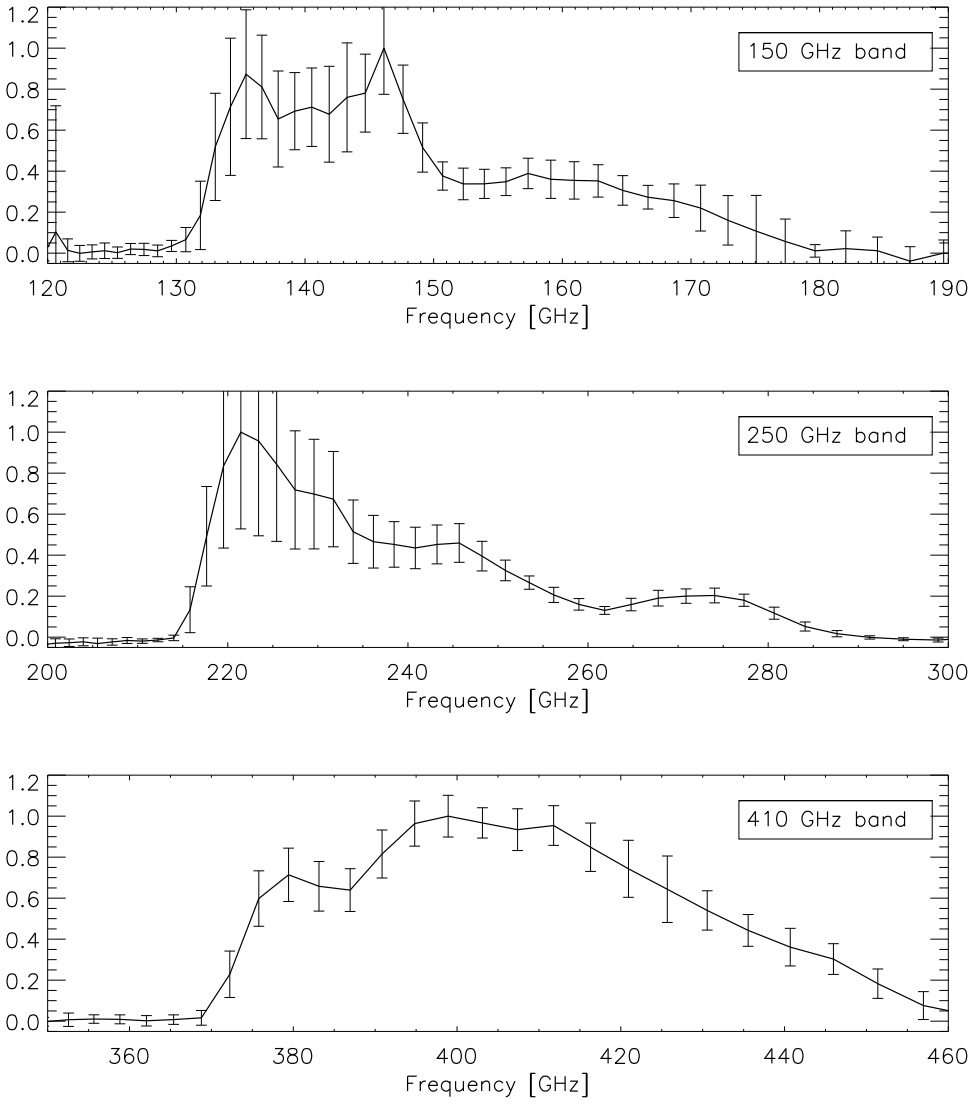

Figure A.1: Measured EBEX bands at 150 GHz, 250 GHz and 410 GHz in the 2012 Palestine ground calibration configuration. The measurements and data analysis to derive these bands are presented in K. Zilic's thesis [34].

Band (GHz)	ν_c (GHz)	$\Delta\nu$ (GHz)
150	148.2 ± 1.0	19.5 ± 1.1
250	235.5 ± 0.8	19.2 ± 0.8
410	388.3 ± 1.1	38.5 ± 1.6

Table A.1: Band parameters for measured EBEX bands in ground calibration configuration. The calculation of the top-hat equivalent band-centers, band-widths and their uncertainties is presented in K. Zilic's thesis [34].

EBEX ground bands	150 GHz	250 GHz	410 GHz
CMB Anisotropy	$60.01^\circ \pm 0.14^\circ$	$52.25^\circ \pm 0.02^\circ$	$59.01^\circ \pm 0.11^\circ$
Galactic Dust	$59.57^\circ \pm 0.18^\circ$	$52.22^\circ \pm 0.01^\circ$	$59.83^\circ \pm 0.14^\circ$
77K source	$59.83^\circ \pm 0.16^\circ$	$52.23^\circ \pm 0.01^\circ$	$59.67^\circ \pm 0.14^\circ$
300K source	$59.83^\circ \pm 0.17^\circ$	$52.24^\circ \pm 0.02^\circ$	$59.71^\circ \pm 0.12^\circ$
2000K source	$59.82^\circ \pm 0.16^\circ$	$52.23^\circ \pm 0.02^\circ$	$59.71^\circ \pm 0.13^\circ$
Flat spectrum	$60.14^\circ \pm 0.16^\circ$	$52.25^\circ \pm 0.02^\circ$	$59.43^\circ \pm 0.12^\circ$

Table A.2: The band averaged IVA phase offsets for different incoming signal spectra given the measured EBEX bands in ground calibration configuration. The uncertainties are calculated using Monte-Carlo simulation with the procedure listed in Sec. 4.2.4. The AHWP parameters used in the simulation here are listed in Table 4.4.

anisotropy, galactic dust, 77 K black body, 300 K black body and 2000 K black body in the list of incident spectra. We also list the results for a flat input spectrum as reference. The procedure to calculate the uncertainty of $\langle\phi\rangle$ using Monte-Carlo simulation is described in Sec. 4.2.4.